UNIVERSITÁ DEGLI STUDI
DI MODENA E REGGIO EMILIA

Dottorato di Ricerca in *Molecular and Regenerative Medicine*

Ciclo XXXVI

UNRAVELING THE ANGIOGENIC POTENTIAL OF INNOVATIVE 3D-PRINTED OSTEOGENIC BIOMATERIALS FOR BONE TISSUE ENGINEERING

Candidata:

Dott.ssa Virginia Stanzani

Relatore:

Prof. Carla Palumbo

Coordinatore del Corso di Dottorato:

Prof. Michele De Luca

INDEX

ABSTRACT

In the last decades, the progressive aging of the population and the increasing incidence of musculoskeletal diseases have enhanced the demand for innovative solutions in bone regeneration. Bone tissue engineering (BTE) fits into this context with the aim to support bone regeneration while providing three-dimensional (3D) porous structures combining cells, biomaterials and chemical factors together, to improve the repair of bone injuries. However, current solutions scarcely consider the role of the vascular component in reparative osteogenesis. In fact, bone is a highly vascularized tissue in which the formation of a functional vascular network is of primary importance during embryonic development as well as during fracture repair. Even if bone has a high regenerative capacity, in particular conditions such as critical-size fractures or degenerative diseases, that seriously compromise the blood supply, restoring the vascular network is preliminary to all osteogenic processes, and consequently to regeneration itself.

For this reason, the aim of this project was to evaluate the angiogenic potential of different osteogenic materials. In particular, three promising biomaterials were investigated: 1) bioplastics; 2) bone powder; 3) bioactive glasses.

Regarding bioplastics, currently there is a strong focus on biological and biodegradable materials for environmental reasons. Poly(3-hydroxybutyrate-co-3-hydroxyhexanoate) (PHBH) is a compostable bioplastic with great biocompatibility, high versatility and good mechanical properties. To reduce the cost of this polymer, part of the amount of PHBH was replaced with acetylated cellulose nanocrystals (CNCs). *In vitro* 3D cell cultures and the chorio-allantoic membrane (CAM) assay showed that the scaffolds obtained via fused filament fabrication (FFF) with the geometry of 350–400 μm pore size displayed the highest angiogenic potential. Among these, the most promising composition was PHBH 10 wt% CNCs. These results revealed that PHBH 10% CNCs with 350-400 μm microporosity possess favourable properties for EC growth, allowing scaffold colonization as well as the induction of *in ovo* angiogenic reaction, both essential features to promote vascularization *in vivo*.

Regarding the bone powder, Pal-OS® derives from scleral ossicles (SOs), naturally decellularized bone plates, localized at the scleral-corneal border of the eyeballs of lower vertebrates. Since the SOs are biocompatible, pro-osteogenic, and not immunogenic, the Pal-OS® powder was produced to better exploit these properties in BTE applications. Specifically, Pal-OS® was printed with a micro-extrusion technique together with different hydrogels; however, satisfactory results have not been obtained yet in terms of angiogenic response induced by the scaffolds *in ovo*.

Lastly, bioactive glasses (BGs) have been evaluated due to their ability to bond bone tissue. BGMS10 and Bio_MS are two novel compositions, created by adding strontium and magnesium ions to the original 45S5 Bioglass® to improve the crystallization temperature and the bioactivity of the gold standard. The three BGs were tested both in the form of granules and scaffolds to evaluate which 3D structure better displays the highest angiogenic potential. *In vitro* cell cultures and *in vivo* analyses showed that the granules have a significant higher angiogenic potential than scaffolds, and that BGMS10 and Bio_MS are significantly more angiogenic than 45S5. The histological evaluations confirmed the high biocompatibility of the granules, also evidencing a remarkable proliferation of the CAM tissues surrounding completely the two novel BGs. Molecular investigation of quantitative polymerase chain reaction (PCR) related to the gene expression of angiogenic markers, such as vascular endothelial growth factor (VEGF) and its receptor, allowed to quantify the angiogenic response of the granules in the CAM assay, further characterizing it over time and confirming the morphological data. In particular, the BG granules were able to upregulate the expression of these genes already after 48 hours.

In conclusion, these results demonstrate that, among the material tested, bioactive glasses may be the most promising materials for BTE applications, laying the foundations for bridging the gap between preclinical research and clinical practice.

0. PREFACE

0.1 *Angiogenesis*

0.1.1 Birth of blood vessels: vasculogenesis and angiogenesis

Blood vessels are the components of the circulatory system that connect each district of the human body through a hierarchically organized network of tubular structures. They have the crucial function of supplying tissues with oxygen and nutrients while removing waste products and carbon dioxide from the circulation. Vessels are composed of tunicae, whose inner lining of endothelial cells (ECs) forms a barrier between blood and the surrounding tissues to control the exchange of solutes and molecules. The vascular endothelium is an active and dynamic structure, which regulates itself by responding to different internal and external signals: in fact, ECs are polarized with their luminal membrane exposed to blood flow and their basolateral surface anchored to a basement membrane (Potente et al., 2011). Since the endothelium is exposed to different mechanical and hemodynamic forces, ECs can sense minimal changes through cell-to-cell junctions, primary cilia, caveolae and the glycocalyx, and respond by the release of vasoactive substances (Krüger-Genge et al., 2019). To stabilize the vascular endothelium and regulate perfusion, the so-called mural cells are recruited: they consist in pericytes that establish direct cell-to-cell contact with ECs, and smooth muscle cells (SMCs) that cover blood vessels externally. ECs and mural cells share a basement membrane which forms a sleeve around the endothelium and prevents resident ECs to leave their position; instead, SMCs are separated from ECs by an extracellular matrix (ECM) (Potente et al., 2011).

ECs derive from hemangioblasts, mesodermal stem cells that can differentiate into hematopoietic stem cells (HSCs) or endothelial precursors cells (EPCs), also known as angioblasts. During embryonic development, EPCs form aggregates called blood islands, the fusion of which leads to the formation of a honeycomb-shaped primary capillary plexus. Then, EPCs differentiate into ECs and the capillary plexus is remodelled into a primitive hierarchical vascular network. The dynamic

process that leads to the creation of vessels *de novo*, starting from a previous avascular tissue, is called vasculogenesis (Adams and Alitalo, 2007). Vasculogenesis can also occur in adults after extensive damage or in pathological conditions such as tumours. In these cases, hemangioblasts are mobilized into blood circulation, recalled into the tissue repair site and driven into endothelial differentiation to form a primitive vascular network (Rouwkema and Khademhosseini, 2016).

Angiogenesis, instead, is the biological process involved in vascular remodelling and in the formation of new blood vessels from a pre-existing network. It naturally takes place in adulthood, in the post-exercise regeneration process in athletes (recovery period), in wound healing and other physiological conditions such as the menstrual cycle in women (Adair and Montani, 2010).

0.1.2 Vascular remodelling: sprouting and intussusceptive angiogenesis

Vascular remodelling occurs according to two main processes: sprouting and intussusceptive angiogenesis. Sprouting angiogenesis is a well-characterized process which is meant to bridge vascular gaps in wound healing and invade tissues in hypoxic conditions or starvation (Adair and Montani, 2010). During this multi-step event, the fate of ECs is not permanently fixed, but is dynamically interchangeable between tip and stalk cells: the firsts start the migration from the vascular endothelium by taking the lead at the branching front, whereas the seconds follow, proliferating and elongating the new sprout in development. Guided by the angiogenic gradient of VEGF-A, tip cells secrete matrix metalloproteinases (MMPs) to make their way through the vessel ECM, moving by the contraction of actin filaments within the filopodia. The degradation of the basement membrane through proteolytic enzymes fortifies the angiogenic response by releasing other pro-angiogenic factors stored inside the ECM (Stegen et al., 2015). Sprouting angiogenesis continues until two or more vessels sprouts converge and fuse together creating a continuous lumen through which blood can flow. At the end of the process, the vessels of neo-formation require maturation and stabilization through the deposition of ECM and the recruitment of mural cells, to sustain shear stress

and other mechanical forces. Finally, when the tissue receives an adequate amount of oxygen, VEGF-A levels return to normal and the tissue reaches a new homeostasis (Potente et al., 2011).

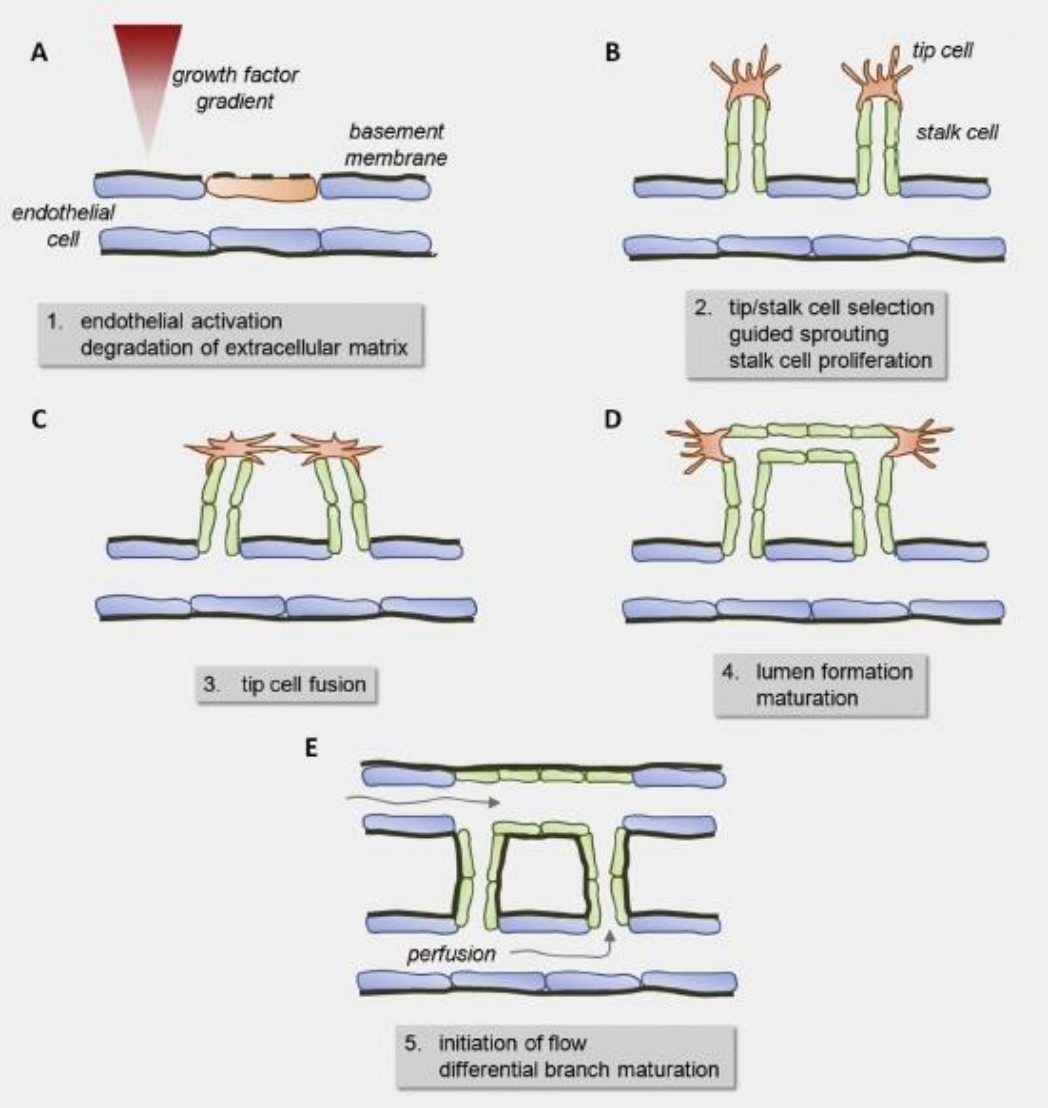

Figure 0.1. Sprouting angiogenesis phases (Stegen et al., 2015).

In contrast, intussusceptive angiogenesis represents an alternative expansion of the vascular network by branching, which has the main objective to increase the complexity of the vascular tree: it is the insertion of a new blood vessel, called transvascular tissue pillar, splitting an existing one into two. This process is faster and more efficient compared to sprouting angiogenesis, since it simply requires the reassembly of resident ECs and, only secondary, their proliferation and migration (Burri et al., 2004).

0.1.3 Structure and functions of the vascular endothelium

The hierarchical structure of the circulatory system starts from the heart, from which arteries branches in arterioles, capillaries, venules, veins, until the heart again. Arteries and veins represent the big diameter vessels and conduct the blood flow without great loss of fluid through the ECs layer, despite the differences in terms of blood pressure. On the contrary, capillaries are vessels with small diameter and huge permeability, meant for the exchange of fluids (Krüger-Genge et al., 2019). During the remodeling of the primary capillary plexus, arteries and veins are formed in a process called arteriovenous differentiation by the influence of hemodynamic forces on ECs that leads to different vessel structures. In fact, arteries are characterized of many concentric layers of SMCs, ECM and elastic fibers to support high pressures and elevated shear stress, whereas veins are surrounded by fewer cells and, consequently, formed by thinner layers since they have to face low-pressure gradients. In addition, veins present valves, low-pressure flap-like structures that have the function of preventing the backflow of blood by letting the flow to stream unidirectionally (Adams and Alitalo, 2007).

However, the mere structural organization is not sufficient to explain the characteristics of the vascular endothelium: vessels should selectively control the passage of molecules to the surrounding tissues by acting as a barrier and maintaining an adequate permeability (Jain et al., 2005). In fact, the vascular endothelium actively controls the degree of vessels constriction and relaxation to regulate the extravasation of solutes and molecules, such as hormones, as well as immune cells transmigration. The vascular tone is set up by ECs and controls the blood flow in each district of the body, keeping the balance between coagulation and fibrinolysis, regulating angiogenesis, the immune responses and consequently inflammation (Krüger-Genge et al., 2019). In addition, the spatial distribution is more important than the number of arteries, veins and capillaries, because to supply the tissues with adequate oxygen and nutrients, while guaranteeing the removal of waste products, cells need to be within a distance for a maximum of 200 µm from a vessel. This diffusion limit implies that the

vascular network must be organized as a tree, with larger vessels branching into smaller ones that can be distributed throughout the tissue thickness (Rouwkema and Khademhosseini, 2016).

In conclusion, structural and functional abnormalities of vessels contribute to the insurgence of different diseases: for example, inadequate vessel maintenance may cause ischemic disorders, whereas excessive vascular growth or abnormal remodeling could promote pathologies such as cancer or inflammatory diseases (Potente et al., 2011).

0.1.4 Molecular mechanisms behind angiogenesis and vascular processes

Angiogenesis is a complex phenomenon that requires the fine coordination of different cellular and molecular actors together. VEGF-A surely represents the main player in angiogenic processes, since it is involved in the majority of morphogenic events and is responsible of ECs proliferation, migration, differentiation and, in general, their survival. Most types of cells respond to a hypoxic environment and high levels of the hypoxia inducible factor 1α (HIF-1α) by secreting VEGF-A, which binds its receptor (VEGFR2) on ECs filopodia. Different gradients of VEGF-A determine the shape of vessels and the differentiation of ECs into tip or stalk cells: for example, high levels of VEGF-A determine a tip cell fate (Eelen et al., 2013). VEGF-A gradients also influence the Delta-Notch signalling pathway by inducing the production of Delta-like-4 (Dll4) ligand on tip cells, which leads to the activation of Notch receptors in stalk cells. The Notch receptor activation suppresses VEGFR2 production in ECs, stopping their migratory behaviour and inducing the differentiation into stalk cells (Potente et al., 2011). The Notch signalling pathway is also involved in the shape of vessels since it promotes arterial phenotype in ECs and in SMCs; on the other hand, its downregulation results in the expression of venous identity genes. Arteries are also marked by ephrin-B2, whereas the expression of the receptor EphB4 is mainly confined in the venous endothelium (Adams and Alitalo, 2007).

Vessel maturation is mainly controlled by the transforming growth factor β (TGF-β) signaling: in particular, it is responsible of mural cells induction and differentiation, and the production of ECM.

Mural cells, in turn, produce angiopoietin 1 (ANG1), which binds the endothelial receptor tyrosine kinase TIE2 to stabilize vessels and promote pericytes adhesion. Mural cells recruitment, instead, is activated by ECs with the induction of platelet-derived growth factor B (PDGFB): this signal stimulates PDGF receptor β (PDGFR-β) onto pericytes that are triggered to migrate and proliferate. Mural cells also require ephrin-B2 to stably associate with the vascular endothelium around ECs. Finally, the fibroblast growth factor (FGF) represents another important player in maintaining vascular integrity through cell-to-cell junctions: in fact, its inhibition leads to ECs dissociation and consequent vessel disintegration. In conclusion, a dysregulation among any of these molecular factors results in cardiovascular pathologies such as hypertension, diabetes mellitus and atherosclerosis (Potente et al., 2011).

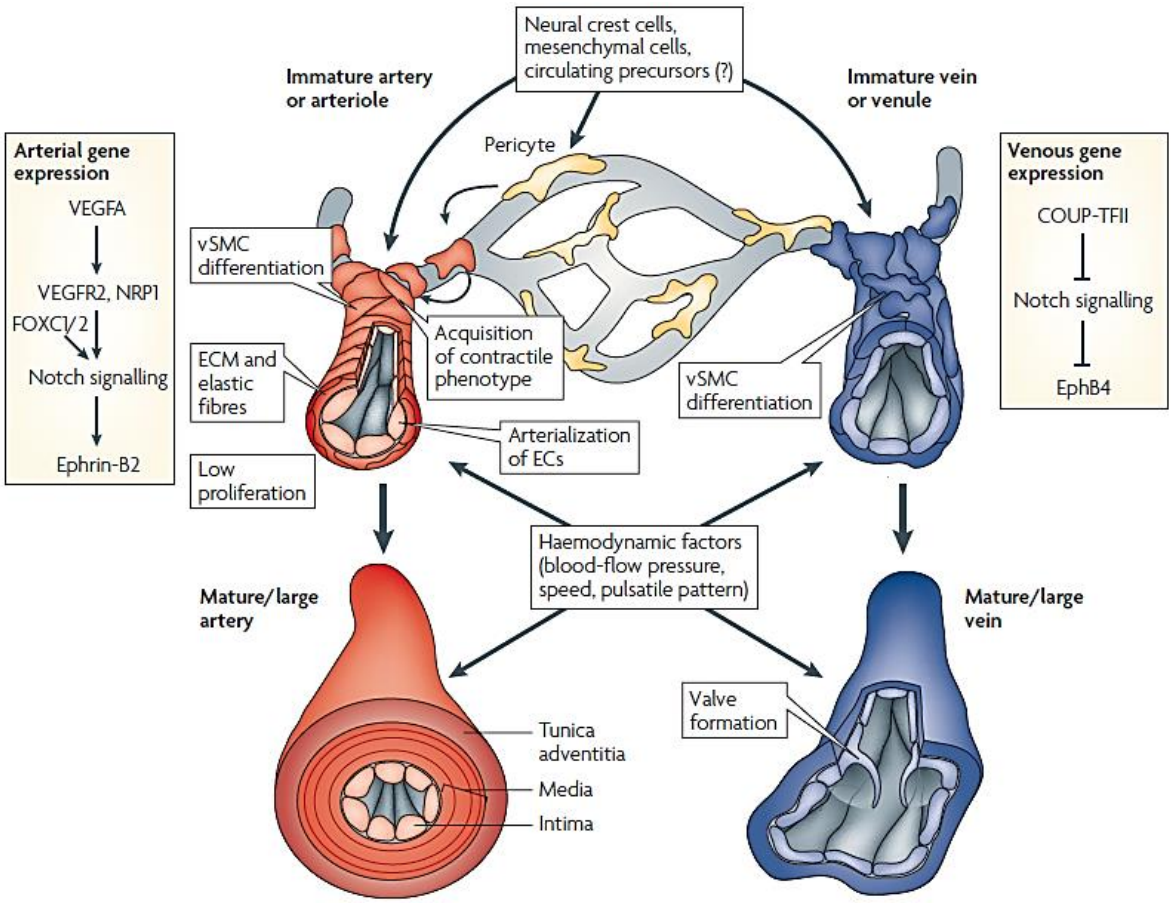

Figure 0.2. Arteriovenous differentiation and mural cell recruitment. (Adams and Alitalo, 2007)

0.1.5 The importance of hemodynamic forces for ECs functionality

The vascular endothelium can sense hemodynamic changes and signals from blood, and to respond by releasing vasoactive factors. ECs are responsible of the production of relaxing and contracting factors modulating blood flow and vascular tone, such as nitric oxide (NO). For example, NO release by the vascular endothelium enhances when shear stress increases. Among the mechanical and hemodynamic forces, shear stress is the friction of the flowing blood against the vessel wall, and it has the most important impact onto ECs since it determines their morphology. In fact, ECs in *in vitro* static cultures present a completely different morphology in comparison to cells subject to shear stress. It has been demonstrated that a mechano-sensory complex at cell-to-cell junctions, composed of platelet endothelial cell adhesion molecule 1 (PECAM1), vascular endothelial cadherin (VE-cadherin) and VEGFR2, is responsible to activate the signalling pathways related to shear stress. In particular, PECAM1, also known as CD31, is the primary mechano-transducer which activates in response to a shear stress signal; VE-cadherin or cadherin-5 (CDH5), instead, is supposed to work as adapter by bringing VEGFR2 and PECAM1 closer, thus facilitating VEGFR2 transactivation. In general, CDH5 is a key component of cell-to-cell junctions since it maintains ECs quiescence, when in complex with VEGFR2 (Krüger-Genge et al., 2019).

0.2 *Approaches to study angiogenesis*

0.2.1 From *in vitro* to *in vivo* models

Cell cultures still represent an irreplaceable model to obtain a first insight and an immediate response to different stimulations *in* vitro. In fact, their easy maintenance, inexpensiveness, versatility and rapidity of outcomes, have made them a good approximation of reality (Edmondson et al., 2014). In the angiogenic context, ECs are the main players. However, *in vitro* conditions do not consider cell-to-cell and cell-to-matrix interactions, typical of a 3D environment, and lack of exposure to shear stress and other hemodynamic forces of the blood. For these reasons, the use of ECs in cell cultures should be considered only a starting point for biological research and not a fully reliable method to assess angiogenesis (Adair and Montani, 2010).

The first approach used by scientists to increase the complexity of responses of *in vitro* assays was the development of *ex vivo* organ cultures: these models combine the *in vitro* environment with a multicellular *in vivo* system. However, even if *ex vivo* models can better recapitulate the *in vivo* environment in comparison to cell cultures, they lack of reproducibility and easy handling (Nicosia, 2009). Instead, 3D *in vitro* models were created to provide an easily accessible platform than *ex vivo* models, while incorporating a 3D environment to mimic native *in vivo* tissues. For example, vascularized micro-organ (VMO) platforms were developed to drive ECs to form a perfusable vascular network within a 3D hydrogel matrix by means of microfluidic technology. However, reproducing the interactions among multiple cell types and the ECM *in vitro* still represent a huge challenge in culture conditions (Nowak-Sliwinska et al., 2018).

To date, *in vivo* models are still widely employed even if they require a high level of surgical proficiency to perform the operations, an animal facility and consequently high costs. In addition, the long and cumbersome protocols to obtain the approval from the ethical committee for animal experimentation are no longer sustainable in terms of times and costs for the scientific research. Recently, the increasing attention to animal welfare worldwide has put an emphasis on the necessity

to develop alternatives to *in vivo* experimentation (Palumbo et al., 2023; Schneider-Stock and Ribatti, 2020). The Three Rs principle (Replacement, Reduction, Refinement), originally defined by Russell and Burch in 1959, encourages the use of alternatives to animal testing. The objectives are: 1) to "replace" the use of animals in research when unnecessary, 2) to "reduce" the number or to obtain more information from fewer animals; 3) to "refine" the methods by alleviating or minimizing pain, suffering or distress, while enhancing animal welfare (Russell and Burch, 1960). In fact, even if *in vivo* models offer the complexity of responses of a living organism, they also present some disadvantages, including the interspecies differences that often do not allow predictable outcomes on humans (Edmondson et al., 2014).

0.2.2 An alternative model to test angiogenesis

The chick chorio-allantoic membrane (CAM) is a non-innerved, highly vascularized, extra-embryonic membrane that has the role of exchanging respiratory gases and metabolites in the chick embryo. The CAM assay is not considered animal experimentation until the hatching, according to the actual Directive 2010/63/EU of the European Union (European parliament and Council, 2010). In fact, pain perception is not completely established in the embryo until the 15^{th} day of development, due to the still immature portion of central nervous system (CNS) involved in the nociception. Also, the immune system is not fully operating until the 18^{th} embryonic day (Janse and Jeurissen, 1991). Since its first description by Rous and Murphy in 1911 in a study of avian tumors (Rous and Murphy, 1912), the CAM model has been exploited in a wide range of applications: for example, to test pro- and anti-angiogenic molecules, to study tumor growth and progression, to sustain organotypic cultures as a "natural bioreactor", to evaluate the angiogenic potential of scaffolds for tissue engineering (Palumbo et al., 2023). In particular, in the study of materials biocompatibility for regenerative medicine purposes, the implantation in CAM has played a crucial role: from the first work of Spanel-Borowski described in 1989 (Spanel-Borowski, 1989), different natural and synthetic

materials have been examined (Ribatti et al., 2020; Stanzani et al., 2023). It has been demonstrated that the CAM is sensible to the chemical-physical properties of materials: for example, smooth surfaces and the positively charged ones, such as polyvinylchlorides or polyurethanes, are responsible of anti-angiogenic responses onto the membrane; on the contrary, rough materials, such as collagen or elastin membranes, can induce a pro-angiogenic reaction onto the CAM (Zwadlo-Klarwasser et al., 2001). Moreover, the structure and the geometry are able to influence the incorporation of materials into the CAM tissues. It has also been demonstrated that the CAM model produces similar inflammatory responses to those found in mammals: in fact, it has been exploited to analyse the effects on angiogenesis and on the formation of inflammatory tissue of different materials (Valdes et al., 2002).

Recently, the CAM model has also been exploited as a bioreactor for organotypic cultures: for example, Moreno-Jimenez reported that the CAM vessels were able to infiltrate human bone cylinders, sustaining human cell viability and bone regeneration *in ovo* (Moreno-Jiménez et al., 2016).

Among all the advantages, summarized in Table 0.1, the CAM assay offers a simple, rapid and economic platform to study angiogenesis since it provides a rapidly growing vascular bed and a constant blood vessel supply (Palumbo et al., 2023). In fact, when a biomaterial is implanted onto the membrane (8-10th embryonic day), the angiogenic response becomes visible through vessels of neo-formation that sprout radially from the implants, like spokes in a wheel. The readout is almost immediate (48-72 h), but commonly the CAM assay is extended up to 4 days to evidence macroscopically the angiogenic reaction at a morphological level (12-14th embryonic day). In fact, the vessels of neo-formation can be easily identified and quantified by an operator or through common software equipped with artificial intelligence, since they differ for morphology and dimensions to the ones of the CAM background (Schneider-Stock and Ribatti, 2020).

For all these reasons, the CAM assay surely represents an advantageous alternative solution for animal experimentation since it fully sustains the Three Rs principles: 1) it "replaces" the use of adult

animals, 2) it "reduces" the number experiments required by obtaining different information (morphological and molecular) from the same egg, 3) it "refines" the sacrificial method, given that the membrane is non-innervate and the embryo does not feel the pain.

Advantages	*Disadvantages*
Short experimental time, rapid screening platform	Limited availability of chick reagents, antibodies, etc.
Easy handling, easy accessibility	Sensitivity to environmental changes
High reproducibility and reliability	Low standardization of protocols in literature
Low costs	Non-specific inflammatory reactions
Well known biology and physiology	Different metabolism compared to humans
Fast vascular growth, natural bioreactor with blood vessels perfusion	Rapid changes of the CAM during embryogenesis (vessel density, morphology)
Natural immunodeficient model	
In vivo imaging, real-time monitoring	
No ethical committee approval, no animal experimentation procedures	
High experimental flexibility and versatility	
No pain perception before 15th embryonic day	
Model for the hallmarks of cancer (proliferation, angiogenesis, invasion, metastasis, drug response)	

Table 0.1. Advantages and disadvantages of the CAM model.

0.3 *Bone tissue engineering*

0.3.1 The importance of angiogenesis in bone

Bone is a highly vascularized tissue in which the formation of a functional vascular network is of primary importance during embryonic development as well as during fracture repair. Blood vessels are necessary not only to supply bone tissue with oxygen and nutrients, while removing waste products, as well as to provide the minerals for building the ECM, such as calcium, magnesium and phosphate; they are also very important to enable morphogenesis and bone design during skeletal organogenesis (Ferretti and Palumbo, 2021). In physiological conditions, the connection between angiogenesis and osteogenesis, *i.e.* the process of bone formation, is particularly evident in the bone marrow niche, where the blood vessels are responsible to maintain skeletal stem cells and HSCs. On the contrary, in pathological conditions such as critical-size fractures, surgical removal of tumours or degenerative diseases, where physiological regenerative processes cannot occur spontaneously, the restoring of the vascular network is preliminary to osteogenesis itself. In fact, it is estimated that about 10% of the fractures results in delayed union or non-unions for an inappropriate blood vessel supply (Stegen et al., 2015).

Bone healing is a complex and highly regulated process, composed of three phases: inflammation, repair and remodelling. After an injury, the damage to the blood vessels inside bone and in the surrounding tissues activate the inflammatory cascade: vasodilatation and exudation of plasma and leukocytes promote coagulation, until fibrinogen is converted into fibrin, leading to the formation of a hematoma. The hematoma is a temporary scaffold characterized by hypoxia and low pH: these signals trigger angiogenesis to form new vessels, attract inflammatory cells, such as macrophages, and deliver pro-angiogenic factors like VEGF-A. In addition, pre-existing periosteal vessels deliver ECs into the facture site to restore the vascular network, while osteoprogenitor cells and fibroblasts produce new bone ECM, gradually replacing the hematoma with a granulation tissue rich in collagen fibers and invading capillaries. Contrary to other soft tissues, bone has a high regenerative capacity,

and it can repair itself without the formation of fibrous scars through a process called endochondral ossification. During the repair phase, the granulation tissue is substituted by cartilage through endochondral ossification, bringing to callus formation. Here, osteoclasts resorb the callus to create new tunnels and porosities that enable the ingrowth of blood vessels. Osteoprogenitor cells, instead, are driven to differentiate into osteoblasts, to deposit new bone matrix and close the gap between bone fragments. Finally, during remodelling, the tissue becomes hyper-vascularized, enabling the final recruitment of cells and nutrients to conclude the bone healing process (Claes et al., 2012).

The coupling between angiogenesis and osteogenesis has also been demonstrated by the presence of a specific vessel subtype, characterized by an increased expression of PECAM1, also known as CD31, and endomucin (EMCN), which has the ability to promote new bone formation (Kusumbe et al., 2014). $CD31^{+}EMCN^{+}$ vessels can also be induced by pre-osteoclasts secreting PDGF (Xie et al., 2014). In addition, the ECs of vessels can directly act on osteogenesis by expressing factors such as VEGF-A, which has a stimulating effect on the differentiation of bone cells, and HIF-1α to promote new bone formation from osteoblasts (Liu et al., 2017).

0.3.2 Bone tissue engineering

In the last decades, the progressive aging of the population and the increasing incidence of musculoskeletal diseases have enhanced the demand for organ transplantation, revealing a severe shortage of donor availability. After blood, bone is the most transplanted tissue, but several side effects of the current gold standard approaches, *i.e.* autografts and allografts, have evidenced the urgent need of alternative solutions to reduce the failure rate in the clinical scenario. In fact, autografts have many drawbacks such as supply limitation from the iliac crest, increased surgery and recovery time, donor site morbidity, that all lead to high failure rate. On the other hand, the main problems associated with allografts either from human cadaver or living donor, or xenografts from animals, is the possibility of pathogen transmission and transplant rejection; moreover, bone matrix

demineralization and decellularization are long and difficult processes. Instead, metal prostheses in titanium or stainless steel can provide high mechanical and structural support, but they lack of degradability, integration in the host site and have a time-limited used (Fernandez de Grado et al., 2018).

Bone tissue engineering (BTE) fits into this context as potential innovative solution for bone regeneration with the aim to overcome the main drawbacks of the traditional techniques. Engineered structures combining cells, biomaterials and chemical factors together, called scaffold, may offer a valid solution to support bone growth while providing a 3D porous architecture. Scaffolds can be employed as acellular systems, to allow the colonization of the host cells once implanted, or combined with cells able to promote *in vivo* bone formation, with or without the release of inductive molecules. However, scaffolds for BTE should have precise characteristics to address that can be grouped into four categories, as reported in Figure 0.3: biological requirements, structural features, biomaterials composition and manufacturing processes. The ideal scaffold should be easy to handle, fast to prepare, sterilizable, reproducible, minimally invasive, and it should meet all the regulatory requirements (Roseti et al., 2017).

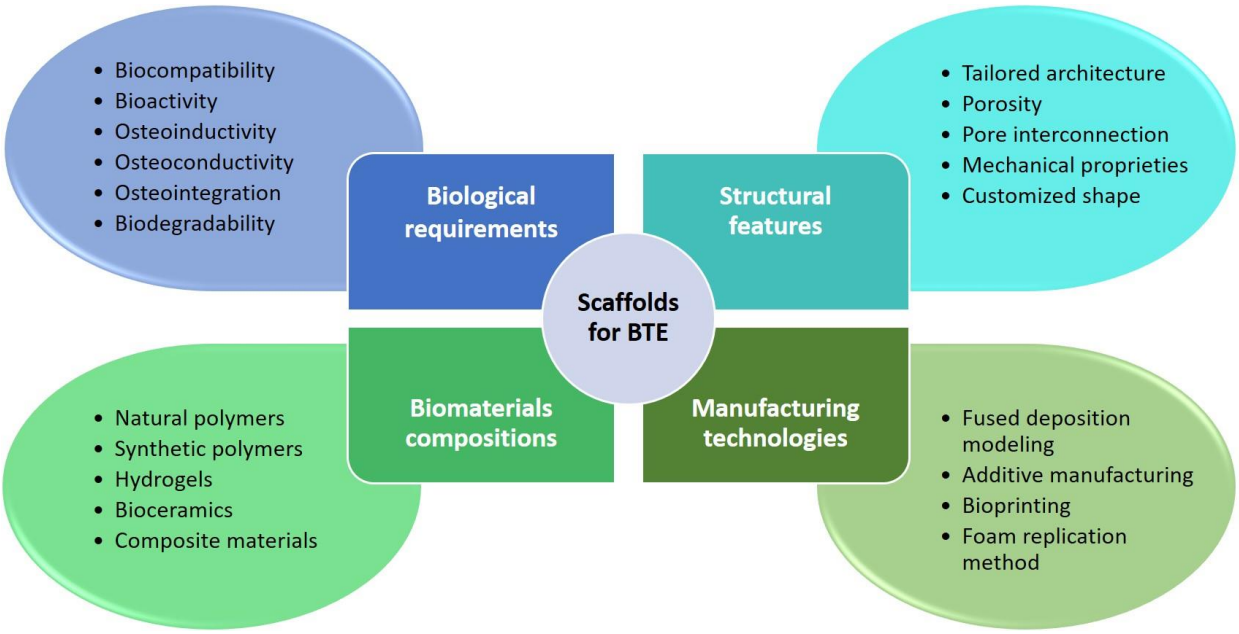

Figure 0.3. Scaffold characteristics for bone tissue engineering.

0.3.3 Biological requirements

Bone tissue is a natural nanocomposite characterized of proteins, mainly type I collagen, dispersed into an inorganic matter of calcium phosphate crystals. Specifically, bone ECM consists of crosslinked collagen fibrils, self-assembled into fibres and bundles, interspersed by carbonate hydroxyapatite. Bone ECM surrounds multiple cell types, such as osteoclasts and osteoblasts that deposit biologically active molecules and growth factors. Therefore, an ideal scaffold for BTE should mimic the natural composition of bone ECM, while supporting cellular attachment and functions (Koons et al., 2020). In general, the biological feature that is mandatory for any scaffold for tissue engineering applications is biocompatibility, which is the ability to be in contact with a living system without producing an adverse effect (Vert et al., 2012). Bioactivity represents the capability to provoke a response from a living matter: bioactive scaffolds promote cell proliferation and differentiation, minimizing the risk of adverse reactions such as scarring. In the bone context, bioactive scaffolds could improve the formation of bone through different mechanisms. Osteoinductivity represents the capacity to stimulate osteogenesis, in other words, to form ectopic bone and to differentiate osteoprogenitor cells into osteoblasts. Consequently, an osteoinductive scaffold should contain growth factors or ions that induce osteogenesis, such as calcium. Osteoconductivity, instead, is the ability to allow the deposition of mineralized ECM and to directly bond to bone; it depends on the composition and structure of the scaffold. Finally, osteointegration occurs as a consequence of the formation of a stable bond between the scaffold and the native bone: it is critical especially for scaffold mechanical stability (Koons et al., 2020).

Biodegradability and biocompatibility of the degradation products released by the scaffolds constitute also other desirable features. In fact, after having supported bone growth in the first place, the ideal scaffold should be gradually replaced by the regenerated tissue, which has the same proprieties of native bone. Commonly, in fact, scaffolds are designed to be mechanically weaker than native bone,

to provide a biological and mechanical sustain for the cells, while synchronizing mineralized tissue deposition and degradation rate (Roseti et al., 2017).

0.3.4 Structural features

The structural qualities of the scaffold influence *in vivo* cell behaviour, not only for bone cell proliferation and matrix deposition, but also for blood vessels growth. Macroscopically, bone is a hierarchical tissue arranged into two different architectures: cortical and cancellous bone. Cortical or compact bone displays high mechanical stiffness and low porosity, whereas cancellous or spongy bone exhibits 10% of the cortical bone stiffness and high porosity. Due to the low porosity of cortical bone, blood vessels and nerves are contained inside the so-called osteons, functional units that present the Haversian canals in the center. The cancellous compartment, although presenting osteons to a lesser extent, has particularly developed vascular surfaces and has an optimal supply of oxygen and nutrients (Simunovic and Finkenzeller, 2021).

Structural requirements must consider the complex 3D architecture of bone and its peculiar porous structure in terms of mechanical proprieties and tissue functionality. In fact, scaffolds should display a higher porosity than 100 µm to ensure both bone cell penetration and vascular ingrowth (Bonfield, 2006). However, conflicting data in literature between *in vitro* and *in vivo* conditions evidence that there is not a single vision about scaffold porosity. For example, Narayan et al. found that smaller pore sizes promote *in vitro* ECs growth on scaffolds (Narayan and Venkatraman, 2008). Instead, Karageorgiou and Kaplan demonstrated that larger pores improve *in vivo* bone growth and osteointegration. In the same work, the authors reported that probably *in vitro* lower porosity enhances osteogenesis due to cell aggregation, but it also suppresses osteoblast proliferation (Karageorgiou and Kaplan, 2005). Another work seems to confirm that larger pores favor both osteogenesis and angiogenesis, since they allow a higher oxygenation in *in vivo* experiments, while a lower porosity results in osteochondral ossification. Anyway, the porosity range depends mainly on

the technique used to fabricate the scaffolds and concerns also the maintenance of the mechanical stability of the 3D structure (Bonfield, 2006).

Since bone is one of the hardest tissues of the body, mechanical proprieties play a fundamental role in the design of the scaffolds for BTE. The objectives are, on the one hand, to minimize the risk of *in vivo* re-fracture with materials presenting low stiffness, on the other hand, to avoid the stress shielding, frequently observed in implants with higher elastic modulus than native bone. Preventing the collapse of the growing tissue at the first compressive load requires an equilibrium of mechanical forces inside and outside the scaffold that should be finely balanced.

Clearly, apart from mandatory characteristics such as biocompatibility, scaffold requirements should vary according to the specific applications and particular clinical needs. For instance, critical-size defects (CSD) demand hard materials with optimized mechanical proprieties due to the dimension of the lesions; instead, small and non-load-bearing lesions could exploit minimally invasive solutions such as hydrogels, that are mechanically weaker, but offer higher bioactivity and biodegradability (Koons et al., 2020).

0.3.5 Biomaterials composition

A biomaterial is a natural, synthetic or hybrid non-vital substance which is intended to interact with a biological system (Vert et al., 2012). Polymers and bioceramics represent the majority of scaffolds that are currently used in BTE. Polymers are organic materials composed of covalently bonded long chains of atoms that can be nature-derived or synthetic. Natural polymers, such as fibrin and chitosan, are typically hydrophilic and have several advantages such as good biocompatibility and bioactivity, low immunogenicity: however, they also present poor mechanical proprieties and high batch-to-batch variability. On the other hand, synthetic polymers show better mechanical proprieties, a good degradation rate and the possibility to fabricate complex structures. In general, they display high versatility since they offer different chemical and molecular modifications that facilitate the tailoring

process to the application requirements. Moreover, synthetic polymers, such as poly(ε-caprolactone) (PCL) and poly(L-lactic acid) (PLA), allow their production in large uniform quantities at low costs and present a long shelf life. However, the major drawback is the lack of bioactivity and the lower biocompatibility in comparison to natural polymers (Koons et al., 2020; Roseti et al., 2017).

Hydrogels are hydrophilic polymers that are currently widely used in tissue engineering, due to their high biocompatibility, versatility, availability, low costs, tuneable biochemical and mechanical proprieties. In particular, their porosity, which is similar to the natural ECM of tissues, has the ability to enhance cell adhesion, nutrients diffusion, cell-to-cell and cell-to-matrix interactions. Hydrogels can have natural, synthetic or hybrid composition. Natural hydrogels derive from plants or animals and are often ECM constituents: they support growth and cell viability because they mimic the physiological environment of cells, but they are affected by high batch-to-batch variability and the possibility of pathogen transmission. Instead, synthetic hydrogels offer a well-standardized production, but they often lack biocompatibility and biological functionality. Finally, hydrogels with hybrid composition are essentially natural polymers that are chemically modified with domains or functional groups to enhance cell adhesion and to increase mechanical proprieties. Due to their high versatility, currently the latter represent the most used solution in BTE applications (Pati et al., 2015).

Bioceramics are a class of inorganic materials categorized as crystalline ceramics, amorphous glasses or partly crystalline glass ceramics. Among them, bioactive glasses (BGs) are gaining more and more attention since they have demonstrated the ability to bind directly with bone tissue. Due to their chemical similarity to bone, these inorganic materials can stimulate osteoprogenitor cells at genetic level and induce bone regeneration. In fact, the regenerative potential of BGs is significantly related to their ionic release, which is critical for both osteogenesis and angiogenesis. In addition to their high biocompatibility and bioactivity, BGs possess antibacterial properties and outstanding mechanical properties such as high compressive strength, resistance, but also brittleness. However,

their main challenge is the tendency to crystallize at high temperatures, which can affect BGs bioactivity and stability, thus limiting their use in BTE (Koons et al., 2020).

0.3.6 Manufacturing technologies

The fabrication technique plays a crucial role in BTE since it influences the biomaterial properties, such as pore architecture, degradability and biocompatibility, and the mechanical characteristics. Conventional techniques, such as solvent casting and particulate leaching, gas foaming, freeze-drying and electrospinning, have important limitations in reproducibility and versatility and, even if they are widely used, they are outdated and disadvantageous for BTE applications (Koons et al., 2020). To date, additive manufacturing (AM) technologies have emerged as the most promising solution for BTE, due to their wide availability and low costs. In particular, these techniques give the opportunity to print three-dimensionally tissues and organs customized for the patient at industrial level, starting from computed tomography (CT) scans or magnetic resonance imaging (MRI); then, 3D scaffolds are fabricated following the computer-aided design (CAD) geometry derived from the CT scans. Computer-assisted 3D printers allows an accurate control over scaffold structure and composition, reaching the complexity of natural bone porosity, anatomically shaped for each patient (Yilmaz et al., 2019). At present, the leading 3D printing technique for polymers is extrusion, since it allows the reproduction of bone hierarchical structure, mimicking its architecture and porosity. All the extrusion techniques originated from fused deposition modelling (FDM), in which materials are melted and extruded as filaments from a small nozzle by mechanical or pneumatic pressure. Following the CAD geometry, those filaments are deposited layer-by-layer on a printing platform and soon after solidified to maintain the 3D structure. In general, the resolution of this technique is typically under 100 µm, but material viscosity and nozzle diameter can influence this parameter (Koons et al., 2020).

Conversely, soft or low-viscosity materials such as hydrogels cannot be melted at high temperatures and require different technologies. Biofabrication is an emerging research area that combines the use

of hydrogels and bioactive molecules to produce 3D scaffolds with high reproducibility and precision. The major advantage of biofabrication techniques, such as micro-extrusion bioprinting, is that living cells can be printed encapsulated into the hydrogels in a mixture called bioink, which mimics the natural characteristics of tissue ECM (Ozbolat, 2016).

Bioceramic scaffolds require still different techniques to be produced. For instance, the foam replication method allows the realization of highly porous scaffolds by coating a polyurethane sponge having a desired porosity with a ceramic slurry. Then, the sponge is thermally treated to slowly burn out the polyurethane, while sintering the inorganic phase (Vitale-Brovarone et al., 2009). Other techniques, such as the polymer burning out method, exploit different organic particles that burn out during sintering: these particles act as pore generating agents that create a good porosity inside the scaffolds (Bellucci et al., 2012).

0.3.7 Vascular tissue engineering in bone: current approaches and main issues

Tissue engineering is an interdisciplinary field that combines life science and engineering principles to restore, improve or establish the physiological function of damaged tissues (Langer and Vacanti, 1993). To date, successes in the field are restricted to avascular structures, such as cartilage, or thin tissues, such as skin, where angiogenesis triggered by the foreign body response is sufficient to maintain the viability of the implant (Jain et al., 2005). Since bone has a peculiar structure and dimensions that limit both the diffusion of nutrients and oxygen and the removal of waste products, a vascular perfusion is essential. In addition to this, based on the knowledge of bone histogenesis, a key aspect appears to be the preliminary establishment of a functional vascular network that supports the processes of osteogenesis. However, in BTE the proposed solutions scarcely consider the vascular component of bone. The majority relies on the combination of osteogenic biomaterials and/or angiogenic growth factors, or directly the use of ECs to engineer a new vascular network, but both the approaches have demonstrated to fail once *in vivo* (Stegen et al., 2015). In the first scenario, the

timing and dosing of the angiogenic molecules are difficult to regulate *in vivo* and they are often the cause of adverse effects. In the second approach, instead, the choice of the EC type is determinant: mature ECs are less available, have a low proliferation capacity and present a different phenotype depending on the tissue from where they are harvested; on the other hand, EPCs are too heterogeneous and limited in number. However, both ECs and EPCs require a perivascular component to improve vascular stability and maturation, such as pericytes and SMCs. Taken together, these pre-vascularization strategies may have a promising potential, but currently they still require experimental validation and the translation into clinic remains difficult (Stegen et al., 2015).

Even if it is possible to maintain an artificial perfusion in laboratory by the use of bioreactors, after *in vivo* implantation, the engineered tissues have very little time before cells start to starve and consequently die. As a foreign body response, the vascular network of the host has a natural tendency to invade the implant, but the process takes days or weeks (Rouwkema and Khademhosseini, 2016). To reduce the amount of time that is necessary to perfuse an engineered tissue, many approaches have been exploited. Among them, Levenberg *et al*. found a possible solution in vascularizing the engineered tissue before implantation. They demonstrated that the *in vivo* integration of pre-vascularized skeletal muscle constructs was improved in three different mice models (Levenberg et al., 2005). This study paved the way to many attempts that had exploited the spontaneous tendency of ECs to organize into vascular networks on scaffolds (Unger et al., 2007), in ECM analogues (Chen et al., 2012), or in cellular aggregates in combination with other cell types (Fuchs et al., 2007). However, the random organization of vessels often resulted in structures that could not fully supply the cells with sufficient nutrients and oxygen support after the implantation. To date, the functional status of the engineered vessels and, in particular, their permeability and longevity, still represent the main issue in tissue engineering (Jain et al., 2005).

Other studies tried to overcome the obstacle of uncontrolled angiogenesis by active patterning the ECs into a vascular network that resembled the physiological organization of the vascular tree. Two

approaches that have in common the use of 3D printing technologies have been exploited. The first method consists in printing channels that resemble the blood vessels and can be seeded with ECs, while the second allows the direct patterning of vascular cells with a controlled geometry in 3D printed vascular structures (Rouwkema and Khademhosseini, 2016). However, even controlling the initial spatial organization and diameter of the vascular tree, *in vivo* remodelling after implantation always changes the original patterning. In other words, the functionality of the printed vascular network cannot be guaranteed once the engineered tissue is implanted *in vivo*. Instead, the vasculature should easily connect to the network of the host, providing continuity and correct functionality once *in vivo* (Chaturvedi et al., 2015).

Guided morphogenesis is an alternative approach, which consists in including chemical signals, such as growth factors and chemokines, inside engineered tissues to control/drive vascular organization and angiogenesis. Even if the main players of angiogenesis are well known, reproducing the space-time coordination of the multiple factors involved is a complex matter and the prediction of the resulting vascular geometry is still challenging (Rouwkema and Khademhosseini, 2016). Moreover, the mechanical properties, such as the stiffness, and the density of the matrix in which the ECs reside, can alter the vascular organization and also the cellular response to growth factors like VEGF-A (Shamloo and Heilshorn, 2010).

AIM OF THE STUDY

In the last decades, the progressive aging of the population is intensifying the escalation of musculoskeletal diseases, demanding new solutions to address the problem of bone regeneration in the clinical scenario. BTE approaches are gaining more and more attention since the traditional solutions, such as autografts and allografts, are no longer exploitable for the high incidence of adverse reactions and the scarcity of donors. For this reason, 3D porous scaffolds of innovative biomaterials, in combination with bone cells and chemical factors, have been created to support bone regeneration. However, since bone is a highly vascularized tissue that requires a functional vascular network both in physiological and in pathological conditions to induce the regenerative processes, the current solutions in BTE must consider the angiogenic component preliminary over osteogenic features.

Recently, the close connection between angiogenesis and osteogenesis has led scientific research to investigate the angiogenic potential of biomaterials prior to the osteoinductive and osteoconductive proprieties (Liu et al., 2017).

The aim of this project was to investigate the angiogenic potential of different novel biomaterials with morphological and molecular approaches both *in vitro* and *in vivo*. This research focuses on the study of three promising biomaterials.

Firstly, the angiogenic potential of a peculiar biopolymer, PHBH, was investigated together with the combination of cellulose nanocrystals at different concentrations. The biocomposites were printed with an extrusion-based technique in 3D scaffolds with different microporosities.

Secondly, we evaluated the angiogenic potential of a peculiar bone powder, called Pal-OS®, obtained by processing peculiar small ossicles (*i.e.* scleral ossicles) from the eyeballs of poultry. 3D scaffolds with the Pal-OS® powder blended with different hydrogels were fabricated through a micro-extrusion bioprinting technique to find the suitable bioink for printing the Pal-OS® powder and maintaining its properties.

Thirdly, two novel bioactive glasses were analysed and compared to the gold standard in the field, called 45S5 Bioglass®. BGMS10 and Bio_MS were created to overcome the tendency of 45S5 to crystallize at high temperatures, which affects its bioactivity, by adding strontium and magnesium. Since they already demonstrated excellent biocompatibility, bioactivity and pro-osteogenic properties, the angiogenic potential of the bioactive glasses was tested both in the form of granules and scaffolds, with the aim to evaluate which 3D structure could better fit in the bone context. Firstly, to evaluate angiogenesis at morphological level *in vitro* 3D cell cultures and the CAM assay were exploited. Then, molecular investigations of the gene expression of markers related to angiogenic pathways were performed through quantitative real time PCR in the CAM assay samples.

Taken together, morphological and molecular analyses revealed that among the three biomaterials tested, the bioactive glasses displayed the highest angiogenic potential in the form of granules, showing interesting results that deserve further investigation.

Collectively, the results of this thesis have evidenced three valuable alternatives for BTE applications in the future. Each biomaterial has peculiar advantages and the ability to address specific patient needs in the clinical scenario. By exploiting different innovative approaches to test angiogenesis in biomaterials, such as the CAM assay applied to regenerative medicine, an artificial intelligence software to evaluate the angiogenic reaction *in ovo* and the quantitative PCR applied to CAM samples, this thesis project gathers original findings that add new insights to the existing body of knowledge in the context of angiogenesis in reparative osteogenesis.

1. CHAPTER I: BIOPLASTICS

1.1 *Introduction*

To date, ecological issues are moving all the industrial sectors, as well as the biomedical field, toward an eco-sustainable development to avoid the depletion of non-renewable resources and petroleum-based plastics. Synthetic polymers, initially selected for their mechanical properties and their resistance to microorganisms, arose many problems related to long-term biocompatibility in the human body. Instead, polymers of natural origin demonstrated the ability to enhance the biological properties of the implants and to reduce the material waste. In addition, resorbability represents another particularly desirable property for implantable scaffolds: specifically, they should be gradually replaced by new tissue while providing support for regenerative processes, without leaving toxic degradation products (Peng et al., 2020). Currently, new bio-based, biocompatible, and biodegradable materials are gaining more and more attention due to the impending environmental issues and the limits of the conventional thermoplastics, such as PLA and PCL. Specifically, PCL has limited mechanical performances (Malikmammadov et al., 2018), whereas PLA suffers from structure instability by chain hydrolysis and thermal degradation (Peng et al., 2020). On the contrary, PHBH is a copolymer of the polyhydroxyalkanoate (PHA) family, which has already been proven as a promising eco-friendly material for biomedical applications. PHBH is an aliphatic polyester mainly synthesized by Gram-negative bacteria under oxygen and nitrogen imbalance with an excess of carbon sources (Kumar et al., 2020). This bio-based, biodegradable and compostable bioplastic already displayed great biocompatibility with different cell types, high versatility and good mechanical properties (Ang et al., 2020; Puppi et al., 2019). However, its high cost is not comparable yet with the affordability of traditional plastic. To overcome this limitation, many studies have recently tried to replace part of the amount of PHBH with different fillers derived from biowaste of the wine or food chain (Giubilini et al., 2021; Nanni and Messori, 2021). In particular, cellulose

derivatives in the form of nanocrystals are displaying the major reinforcing effects (Giubilini et al., 2020a). To date, only a few studies reported the 3D printing of PHBH and cellulose nanofibrils (CNF) and, commonly, the presented biocomposites had a cellulose content below 3 wt% with a decrease in mechanical performances (Valentini et al., 2019). Instead, Giubilini *et al*. demonstrated that functionalized CNCs had an impressive mechanical reinforcement effect, at different concentrations of CNCs, namely, 5, 10, 15, and 20 wt% (Giubilini et al., 2020b).

To date, BTE approaches have mainly focused on enhancing the colonization of the scaffolds only considering the bone cells, such as osteoblasts and osteoclasts, and mesenchymal stem/stromal cells (MSCs) (Stegen et al., 2015). For example, bone marrow MSCs (BMSCs) were used to demonstrate the biocompatibility and the osteogenic ability of PHBH both on films (Yang et al., 2004) and on scaffolds with a 3 μm pore size diameter (Wang et al., 2004). Moreover, PHBH has already been tested for hemocompatibility and stent vessel applications, but any study has ever investigated the angiogenic potential of this material either alone or in combination with CNCs (Puppi et al., 2017; Zhang et al., 2007).

In addition, among AM technologies, fused filament fabrication has emerged for printing thermoplastic polymers for its high precision and since it does not employ any toxic solvents. This extrusion-based technique has the great advantage of maintaining the biocompatibility of materials and, consequently, it can be widely used in the biomedical field as well as in BTE applications (Stanzani et al., 2023).

In this study, for the first time, PHBH with different percentages of CNCs were printed through FFF technique according to different microporosities to evaluate which composition and 3D scaffold structure may have the highest angiogenic potential for BTE applications.

1.2 *Materials and methods*

1.2.1 Fabrication of biocomposites

PHBH containing 11 mol% of hydroxyhexanoate was supplied in pellet form (code B6H N15, MAIP SRL, Turin, Italy). Before any processing, PHBH pellets were oven-dried at 85°C overnight. CNCs (CelluForce, Quebec, Canada) show a ratio between the average length (120 nm) and the diameter (6.5 nm) of about 18. Acetic anhydride and sulfuric acid (95–97%) (Merck KGaA, Darmstadt, Germany) were used as received without further purification.

The affinity between the hydrophilic CNCs and the hydrophobic PHBH matrix was improved through an acetylation of the CNCs, as presented by Giubilini *et al*. (Giubilini et al., 2020b). Briefly, acetic anhydride (75 ml) was mixed with sulfuric acid (150 µl), used as a catalyst, and then CNCs (15 g) were added to this solution under mechanical stirring at 250 rpm for 8 h at 30°C. Acetylated CNCs were then washed four times by centrifugation and redispersion. The melted compounding between PHBH and acetylated CNCs was performed using a DSM Xplore 15 twin-screw micro-compounder (Engelmann & Buckham Ltd., Hampshire, USA) with a batch volume of 15 cm^3 and conical screws at a processing temperature of 130°C, a mixing speed of 100 rpm, and a mixing time of 120 s. Final biocomposites were obtained at 0, 5, 10, 15, and 20 wt% nanocrystal contents. Hereafter, the samples were named PHBH X% CNC, where X corresponds to the weight percentage of CNCs. Filaments were made by extrusion at 145°C through a die orifice with a diameter of 1.8 mm, using a piston extruder (Rosand RH7 Flowmaster, Netzsch GmbH, Germany) at an extrusion speed of 8.5 mm min^{-1}. Then, the filaments were stored in a desiccator to prevent moisture absorption, which would affect the 3D printing process. To assess the biocompatibility of the bio-based composites, hot-pressed films were obtained by pressing the material at 125°C with this pressure cycle: 5 kPa for 60 s, 10 kPa for 60 s, and then cooled to room temperature (RT) at 5 kPa for 60 s. The final thickness of the hot-pressed films was 130±10 µm.

1.2.2 Fused Filament Fabrication

The structure of the 3D-printed PHBH–CNC composite scaffolds was modelled using SolidWorks 2016 software (SolidWorks Corporation, USA). Specifically, a grid-filled geometry with fully interconnected structures was prepared with an alternation of 90° for each layer, a vertical height of 1.5 mm, and a square base of 15×15 mm^2. All scaffolds were printed using a commercial FFF-based 3D printer (TREAStilla 3D FFF, Stilla3D, Italy) with a nozzle temperature of 180°C, a platform temperature of 50°C, and a printing speed of 5 mm s^{-1}. The nozzle diameter and the layer height were 0.4 and 0.2 mm, respectively. A linear infill type was chosen for all samples, whereas the microporosity of the structure was tuned by varying the infill percentage among 60%, 50%, 45%, and 40%, respectively, named S1, S2, S3, and S4. The microporosity was assessed with the ESEM Quanta 200 Scanning Electron Microscope (SEM) (Fei Company, Hillsboro, OR, USA) performing ten different measurements of each micrograph for every sample type. For experimental needs, the 3D-printed scaffolds were hand cut with a scalpel, resulting in specimens less than 5 mm wide, suitable for all the analyses.

1.2.3 ^{13}C Cross-Polarization-Magic Angle Spinning Nuclear Magnetic Resonance Spectroscopy

Solid-state ^{13}C cross-polarization-magic angle spinning (CP-MAS) nuclear magnetic resonance (NMR) spectra of unmodified and acetylated CNCs were acquired at 27°C using an AVANCE IIIHD600 (Bruker, Billerica, Massachusetts, USA) spectrometer equipped with a 2.5mm H/X CP-MAS probe operating at 150.90 MHz. ^{13}C CP-MAS NMR spectra were obtained at 16 kHz MAS rate, using the standard Bruker CP sequence. The parameters used were: 125 kHz spectral width, 10 s relaxation delay, 2.4 μs 90° pulse, 4000 data points, and 32 or 64 scans. All chemical shifts were referenced by adjusting the spectrometer field to the value corresponding to 38.48 ppm chemical shift for the deshielded line of the adamantane ^{13}C NMR signal.

1.2.4 *In vitro* cell cultures

DsRed-modified mouse aortic endothelial cells (MAEC) were provided by the laboratory of Prof. Stefania Mitola (University of Brescia, Italy). MAEC DsRed were thawed and seeded at 6000 cells cm^{-2} in Dulbecco's Modified Eagle Medium (DMEM) (Corning, Somerville, Massachusetts, USA) added with 10% fetal bovine serum (FBS), 1% glutamine, and 1% penicillin/streptomycin (10^4 IU mL^{-1} and 10 mg mL^{-1}) (all from Euroclone, Milan, Italy). The maintenance medium was substituted approximately every 48 h of culture. When MAEC DsRed reached the 80–85% of confluence, they were detached using 0.05% trypsin/0.02% ethylenediaminetetraacetic acid (EDTA) and counted using 0.4% Trypan blue staining (both from Euroclone, Milan, Italy). Before all the biological evaluations, the materials used as scaffold were washed three times in 1× PBS and sterilized under ultraviolet (UV) light. MAEC DsRed were seeded over each material at 2×10^4 cells cm^{-2} in a 24-well plate and cultured for 10 days at 37°C and 5% CO_2. Specifically, the cells were cultured until 72 h onto the films, whereas for 10 days onto the 3D-printed scaffolds. To evaluate the growth rate of endothelial cells over PHBH–CNC films, cell nuclei stained with 4′,6-diamidino-2-phenylindole (DAPI) (Millipore, Merck KGaA, Darmstadt, Germany) were counted from ten different pictures acquired at the same magnification for each specimen; then, the number of cells counted was normalized over the area (cm^2). The analysis was conducted in triplicate with three independent experiments.

1.2.5 Morphological analysis

The films and the scaffolds were washed in 1× phosphate-buffered saline (PBS) and fixed with 4% paraformaldehyde/PBS (Sigma Aldrich, Darmstadt, Germany) at RT for 20 min. Then, after another wash in 1× PBS, cell nuclei were stained with DAPI (Millipore, Merck KGaA, Darmstadt, Germany) and observed under fluorescent light with a Nikon Eclipse Ni microscope (Nikon Instruments Europe BV, Amstelveen, The Netherlands).

After the immunofluorescence analysis, the same specimens were dehydrated through an ascending ethanol series (50%, 70%, 95%, and 100% ethanol, 30 min each), air-dried, transferred over stubs, and coated with gold by using Emitech K550 sputter coater (Quorum Technologies, South Stour Avenue, Kent, UK). MAEC DsRed morphology and scaffold colonization were observed in high vacuum conditions at the ESEM Quanta 200 SEM (Fei Company, Hillsboro, OR, USA).

1.2.6 CAM assay

Fertilized Isa Brown chicken eggs (Azienda Agricola Cellini Andrea, Forlì, Italy), staged according to Hamburger and Hamilton's classification (Hamburger and Hamilton, 1951), were placed into an incubator (FIEM Mercurius MG244, Como, Italy) at 37.8°C in constant humidity conditions. After 3 days of incubation, at stage 3 of embryo development (ED3), a square window was opened into the eggshell, after the removal of 2–3 mL of albumin, to detach the developing CAM from the shell. After verifying embryos viability, the window was sealed with 18×18 mm^2 coverslip, fixed to the shell with paraffin, and then the eggs were returned to the incubator. At stage ED8, the coverslips were removed, and the CAM assay was performed placing the materials over the CAM; then, the eggs were closed again, replacing the coverslips, and returned into the incubator. Six eggs were used for each condition and all experiments were carried out in independent triplicate. After 4 days of development (ED12), the eggs were opened, removing the coverslips, and the CAMs grafted with the materials were photographed *in ovo* using a Nikon SMZ745T stereomicroscope (Nikon Instruments Europe BV, Amstelveen, The Netherlands) equipped with a digital camera and Xentry software (both Alexasoft, Florence, Italy). Images were taken at ED12; the angiogenic response was evaluated by comparing the grafted CAMs with the controls at 1× magnification. In addition, the viability of embryos was considered as an index of the biocompatibility of the materials.

1.2.7 Statistical analysis

Experiments were all carried out in independent triplicate, which means that samples were treated, isolated, and analysed separately. All data are expressed as mean±standard deviation (SD). Differences between the experimental conditions were evaluated by one-way analysis of variance (ANOVA) with Bonferroni's correction for multiple comparisons. The type of analysis and significant p-values are shown in figure legends. Differences are classified as significant with a p-value (p) < 0.05. Statistical analysis and relative graphs were elaborated with GraphPad Prism 6 (version 6.01, San Diego, USA).

1.3 *Results*

1.3.1 350-400 µm pore size is the most colonized scaffold by endothelial cells *in vitro*

Neat PHBH was exploited to test the four scaffolds (S1, S2, S3, and S4) and to set the printing parameters for FFF technique. The differences among the four microporosities are showed in the pictures acquired by SEM, reported in Figure I.1; the same data are expressed quantitatively in Table I.1 through mean values and SD of measurements conducted on the images.

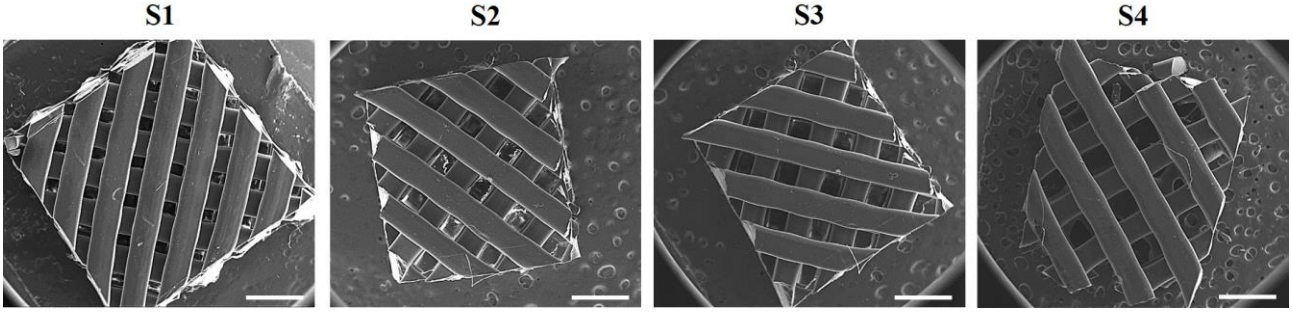

Figure I.1. SEM of PHBH 3D scaffolds with different microporosity as a function of varying infill percentage; magnification 50X, scale bar 1 mm.

CODE	INFILL PERCENTAGE [%]	PORE SIZE [µm]
S1	60	237±16
S2	50	313±18
S3	45	370±25
S4	40	467±19

Table I.1. Correlation between the infill percentage of the 3D printing process and the final pore size for the four scaffold geometries.

Then, MAEC DsRed were seeded and cultured for 10 days over the four different samples. The immunofluorescence analysis showed that all the scaffolds were colonized, but to different extents. As shown in Figure I.2a, MAEC DsRed were able to colonize the upper layers of the scaffolds and only a few sparsely scattered cells were found in the lower sheets. Among the four microporosities, only S3 scaffolds allowed MAEC DsRed to colonize homogeneously also the lower layers. Observing the same specimens at SEM, reported in Figure I.2b, it is possible to visualize how these cells are well connected to each other and display their peculiar dendritic morphology, especially in S2 and S3 scaffolds.

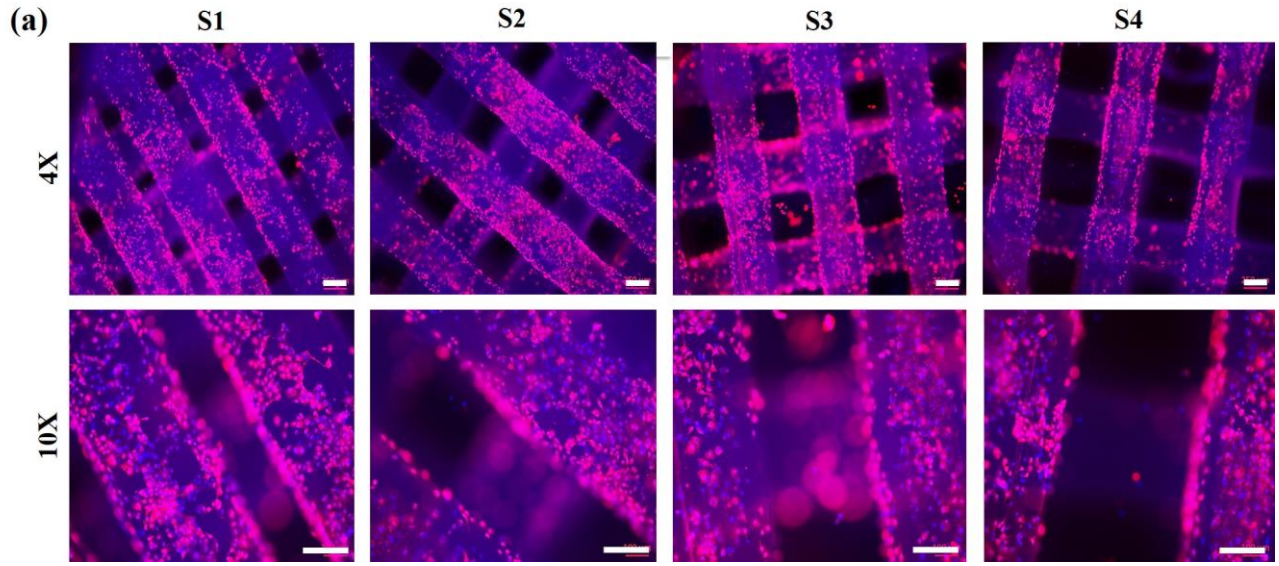

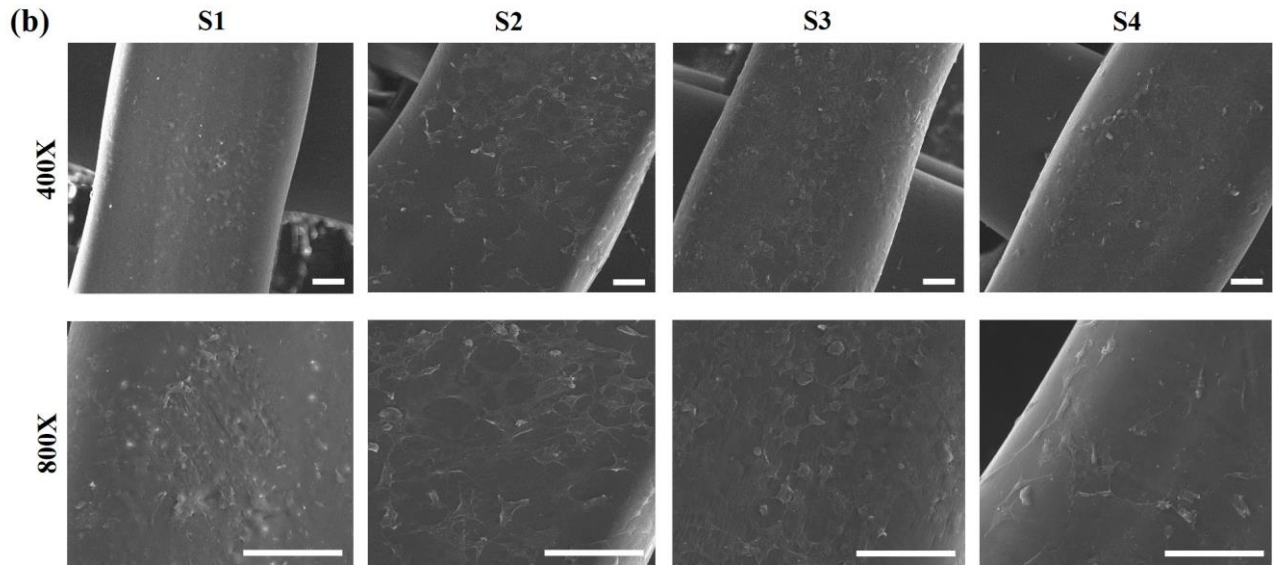

Figure I.2. Micrographs show MAEC DsRed colonizing PHBH scaffolds at varying internal microporosity. (a) Immunofluorescence evidenced in blue cell nuclei (DAPI) and in red cytoplasms (DsRed); magnifications 4 and 10X, scale bar 250 μm. b) Cell morphology of the same specimens was evaluated at SEM; magnifications 400 and 800X, scale bar 100 μm.

The four geometries of PHBH were also tested *in ovo* to observe any differences in the development of vessels onto the CAM. After four days of incubation, images of the scaffolds at ED12 were acquired and analysed. As shown in Figure I.3, all the geometries displayed an evident angiogenic response (visible through the peculiar reaction of the CAM vessels sprouting radially from the materials, such as spokes in a wheel), but comparable to each other. For this reason, the study proceeded by adding previously functionalized CNCs to PHBH at various concentrations (5, 10, 15, and 20 wt%) to enhance the angiogenic potential of this biopolymer.

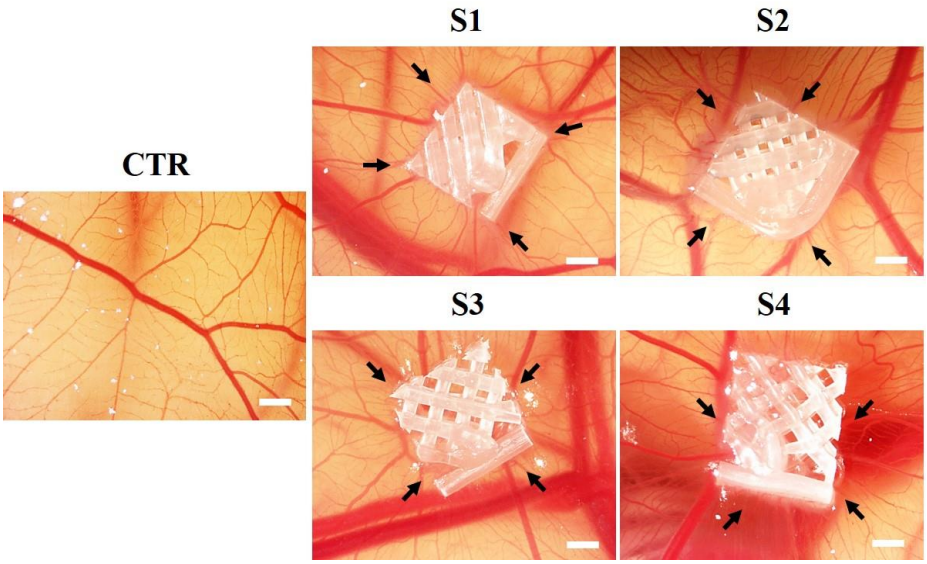

Figure I.3. CAM assay for the evaluation of the angiogenic potential of different PHBH scaffold at varying internal microporosity: images show the vascular reaction triggered by the scaffolds at ED12. The four geometries were compared to the control CAM (CTR); note the abundant vessels spreading out from the scaffolds (arrows); magnification 1X, scale bar 1 mm.

1.3.2 ^{13}C CP-MAS NMR spectroscopy showed acetylated CNCs

^{13}C CP-MAS NMR spectroscopy demonstrated that the process of acetylation occurred positively, as shown in Figure I.4. The former is the spectrum of untreated CNCs and displays typical signals from cellulose: C_1 (105 ppm), C_4 crystalline (89 ppm) and C_4 amorphous (84 ppm), $C_2/C_3/C_5$ (72 and 75 ppm), C_6 crystalline (65 ppm), and C_6 amorphous (63 ppm) (Tingaut et al., 2010). After 8 h of acetylation, the characteristic signals of the acetyl group emerged at 172 and 21 ppm, corresponding to the carbons of the carbonyl (C¼O) and methyl (CH_3) groups of the grafted moiety, respectively. Moreover, an additional decrease in the C_1 intensity at 105 ppm was observed together with the progressive appearance of a shoulder at 102 ppm, as shown in the second spectrum. In literature, it was reported that the acetylation of polysaccharides results in a downfield shift of the peak, corresponding to the O-acetylated carbon, and a concomitant upfield shift of the carbon,

corresponding to the adjacent carbon (Jebrane and Sèbe, 2007). Therefore, the shoulder at 102 ppm was associated with the upfield shift of the C_1 after acetylation of the OH at the C_2 position.

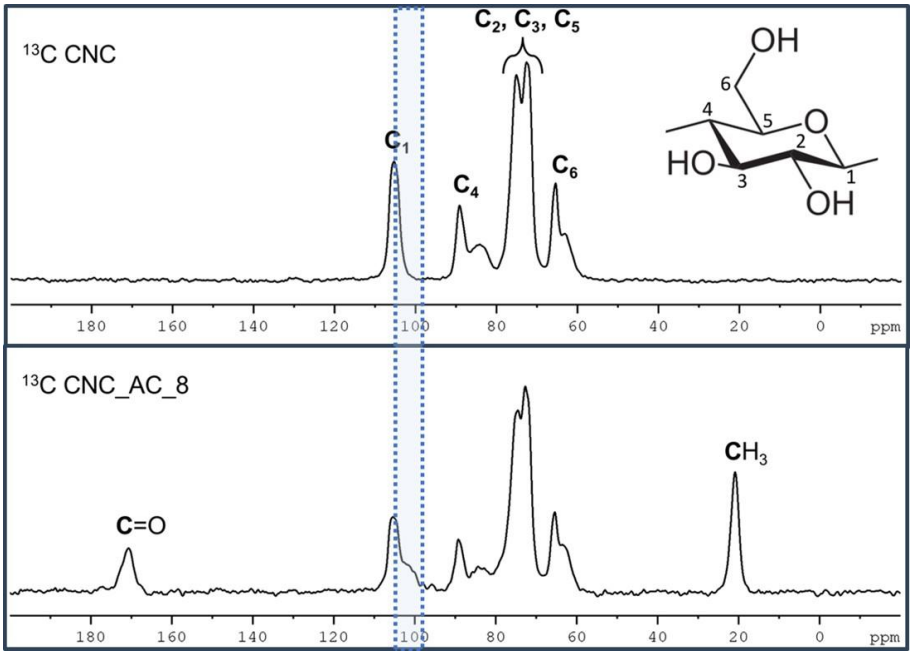

Figure I.4. ^{13}C CP-MAS NMR spectra of pristine CNC and after 8 h of acetylation (CNC_AC_8).

1.3.3 Films of PHBH 10% and 15% CNCs demonstrated the highest angiogenic potential *in vitro* and *in vivo*

First, four different composites of acetylated CNCs at different percentages 5, 10, 15, and 20 wt% suspended in PHBH were prepared and printed in the form of films. MAEC DsRed were seeded onto the films and monitored daily until 72 h of cell culture. After 48 h, immunofluorescence analyses were performed showing that all the PHBH-CNCs biocomposites allowed the growth of ECs, as reported in Figure I.5. After 72 h of culture, MAEC DsRed had colonized all the materials, visibly increasing their number in comparison to the 48 h. The SEM analysis showed the physiological morphology of ECs over all the biocomposites; in particular, Figure I.6 highlights many cell-to-cell contacts through cytoplasm extensions over the four different films.

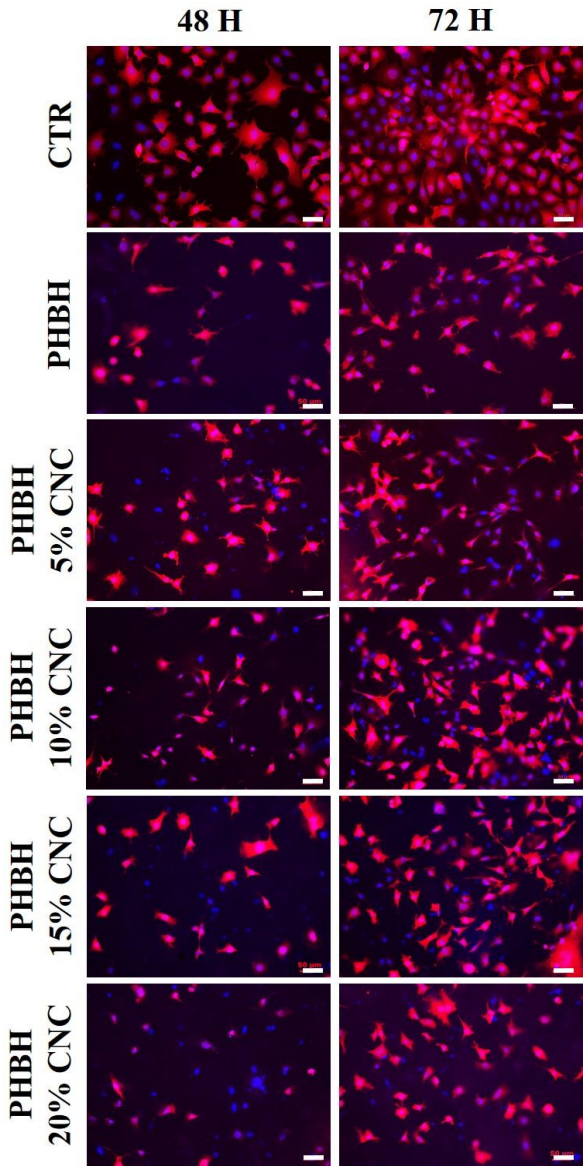

Figure I.5. *In vitro* biocompatibility of PHBH-CNC biocomposites. Different concentrations of PHBH-CNC were tested with MAEC DsRed and monitored with immunofluorescence analysis after 48 and 72 h of culture. Representative images of cells colonizing PHBH-CNC films are compared to PHBH alone; cell nuclei are stained in blue (DAPI), cytoplasms in red (DsRed); magnification 20X, scale bar 50 µm.

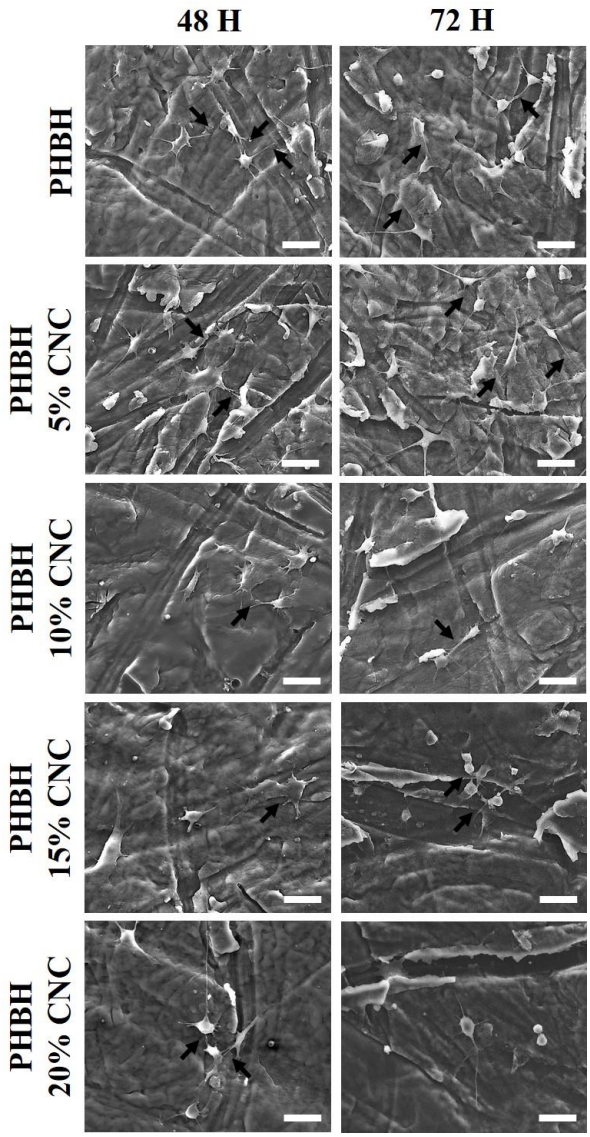

Figure I.6. SEM analysis of MAEC DsRed morphology over films of different PHBH-CNC biocomposites; note the cell connections (arrows); magnification 1200X, scale bar 100 µm.

Then, cell growth was quantified and the relative statistical analysis, as shown in Figure I.7, revealed that after 48 h of culture, samples with 5, 10, and 15 wt% of CNCs were significantly better colonized than the ones with neat PHBH or 20% of CNCs. After 72 h, instead, PHBH 10% CNC significantly peaked over the other formulations, followed by PHBH 15% CNC. These results suggest that overall the compounding with CNCs improved the biocompatibility of PHBH in comparison with the neat biopolymer.

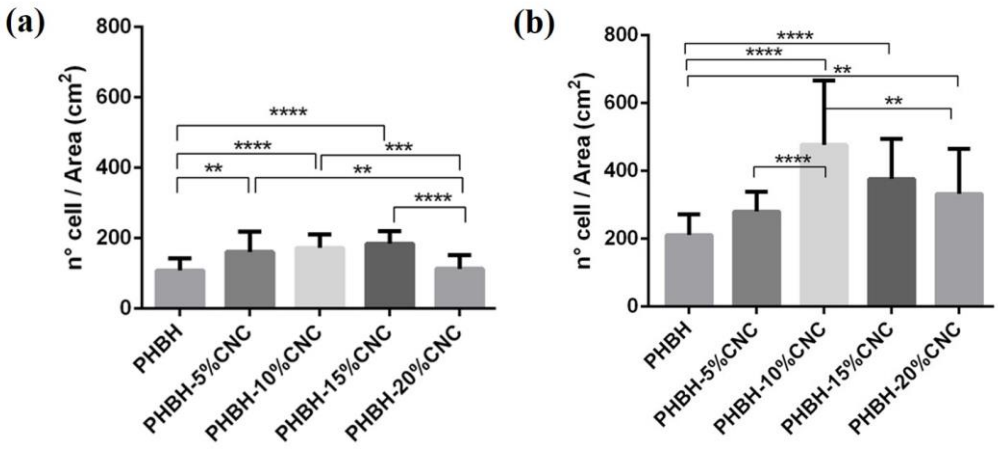

Figure I.7. Cell growth rate on different compositions of PHBH-CNC samples was tested with MAEC DsRed *in vitro* after (a) 48 and (b) 72 h of culture (**p ≤ 0.01; ***p ≤ 0.001; ****p ≤ 0.0001).

To deepen the *in vitro* results, the CAM assay was performed. After 4 days of *in ovo* incubation, the morphological analysis of the neo-formed vessels indicates that the formulation with the highest angiogenic response was PHBH 10% CNCs, as shown in Figure I.8a. In addition, this data was also confirmed by the number of viable embryos at ED12, reported in Figure I.8b. Even to a minor extent, positive results were also displayed by PHBH 5% and 15% CNCs: these two formulations showed a visible vascular reaction over the CAM and a high embryos viability at ED12.

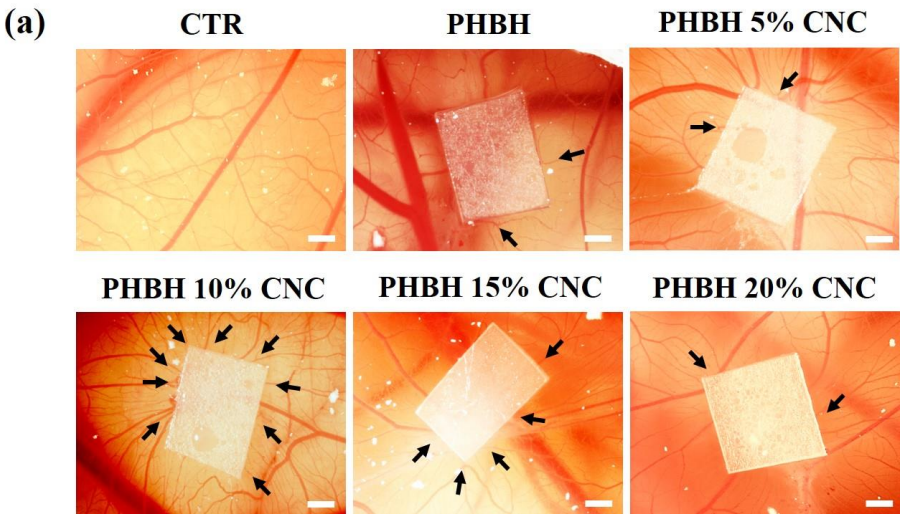

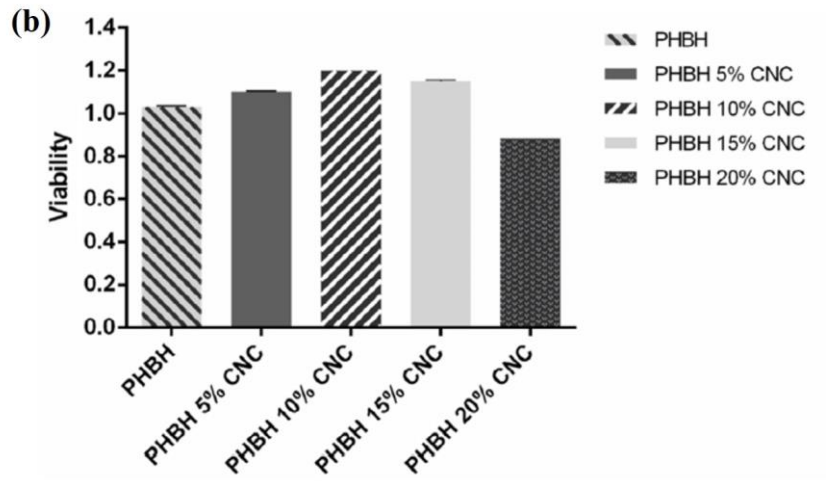

Figure I.8. *In ovo* biocompatibility of PHBH-CNC biocomposites. (a) CAM assay of films of different PHBH-CNC concentrations and their angiogenic reaction *in ovo* (arrows); magnification 1X, scale bar 1 mm. (b) Viability of the tested eggs: all data were normalized on the control.

1.3.4 PHBH 10% CNCs with 350-400 µm microporosity showed the significantly highest cell colonization compared to other scaffolds

According to the preliminary data obtained, the S3 geometry was chosen due to the most homogeneous colonization of ECs over the three dimensions *in vitro* and their typical dendritic morphology, as observed through the SEM analysis. On the other hand, the composition with 10% and 15% CNCs were selected since they showed the most interesting results both *in vitro* and *in ovo*. By means of FFF technique, 3D scaffolds of PHBH 10% and 15% CNCs were printed with S3 microporosity. The immunofluorescence analysis of MAEC DsRed seeded and cultured over the scaffolds shows the comparison between the two formulations and neat PHBH, as reported in Figure I.9a. After 10 days of culture, the images suggest that PHBH 10% CNCs scaffolds were better colonized in the three dimensions than PHBH with 15% CNCs ones, displaying more cells over the superficial layers. Neat PHBH showed a comparable colonization to PHBH with 10% CNCs. The

results, shown in Figure I.9b, demonstrated that PHBH 10% CNCs scaffolds were significantly better colonized than the other two formulations.

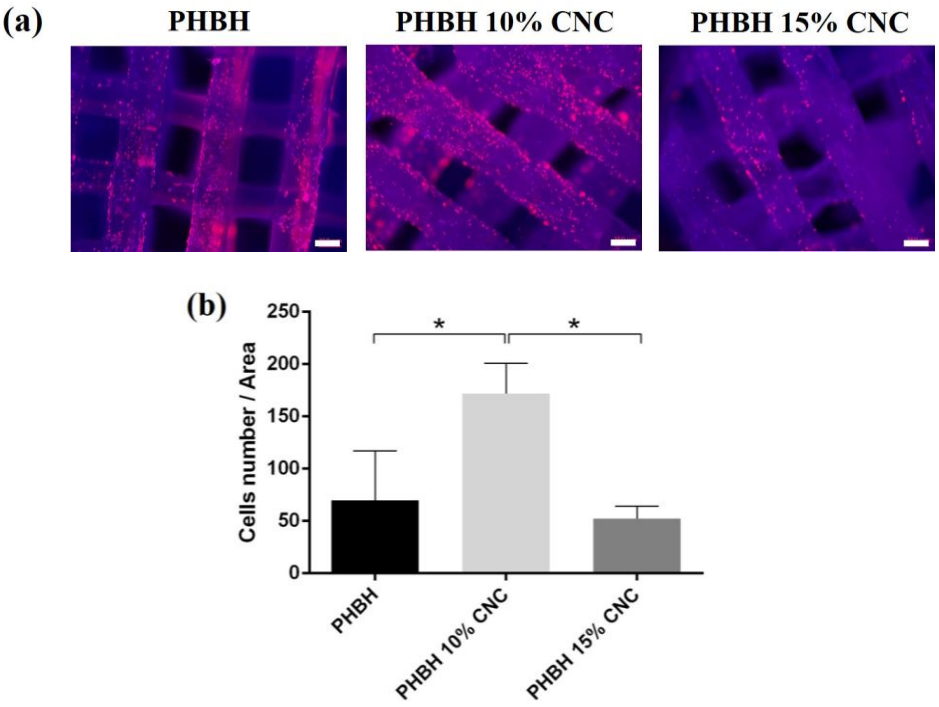

Figure I.9. Cell colonization after 10 days of culture of 3D-printed scaffolds by MAEC DsRed with two different PHBH-CNC compositions (10 and 15 wt%) and neat PHBH, used as control. (a) Immunofluorescence characterization: cell nuclei in blue (DAPI), cytoplasms in red (DsRed); magnification 4X, scale bar 250 µm. (b) Cell number per area, with statistically significant variances (*p ≤0.05).

Finally, the angiogenic potential of the S3 PHBH–CNCs scaffolds was tested *in ovo*. The CAM assay highlights that at ED12 all the angiogenic reactions were comparable, as shown in Figure I.10. The visible vascular reactions confirm, on the one hand, the biocompatibility already observed *in vitro*, on the other hand, the absence of noticeable differences in terms of angiogenic potential among the different formulations of PHBH-CNCs.

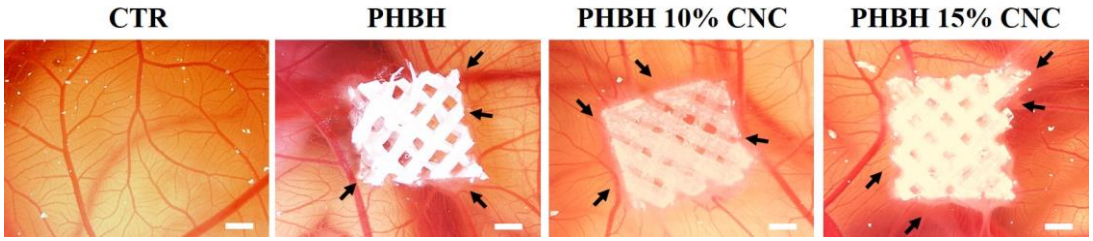

Figure I.10. CAM assay for the evaluation of the angiogenic potential of different PHBH-CNC 3D-printed scaffolds at varying compositions compared to the control (CTR); magnification 1X, scale bar 1 mm.

1.4 *Discussion*

Following the emerging debate about environmental issues in the biomedical field, this study focused on biobased, biodegradable and compostable polymers from the PHA family. Specifically, scaffolds of PHBH reinforced with CNCs at different concentrations (5, 10, 15 and 20 wt%) were printed realizing four microporosities through FFF. This high-precision extrusion-based technique, which does not make use of any toxic solvents, was exploited to mimic the peculiar architecture of bone and to preserve the biocompatibility of the materials. The four microporosities spaced from 200 to 500 μm, since in literature are reported conflicting results regarding scaffold pore size and cavity wideness in BTE. For example, Narayan *et al*. reported that pore sizes inferior to 100 μm enhanced the proliferation of human umbilical vein endothelial cells (HUVEC) *in vitro* over poly(L-lactic acid) (PLLA) and poly(lactic-coglycolic) acid (PLGA) scaffolds (Narayan and Venkatraman, 2008). However, many studies indicate that larger pores than 300 μm favour osteogenesis, allowing vascularization and high oxygenation, while a smaller porosity results in osteochondral ossification (Karageorgiou and Kaplan, 2005). Another study demonstrated that PLGA inverse opal scaffolds with higher pore size, between 250–300 μm, improved vascularization *in vivo* in athymic nude mice by favouring the formation of vascular networks with large blood vessels at low densities and greater penetration depth (Choi et al., 2013).

Since PHBH was already demonstrated to be an osteogenic material (Wang et al., 2004; Yang et al., 2004), this study focused on evaluating EC colonization of the scaffolds *in vitro* and the eventual angiogenic potential *in ovo*. To evaluate which pore size could trigger the highest angiogenic response, the four 3D-printed microporosities of neat PHBH (S1, S2, S3 and S4) were tested *in vitro.* The results suggest that all the scaffolds were colonized by MAEC DsRed in the superficial layers, but only the S3 geometry allowed EC growth also in the deeper sheets. This data confirms that higher pore sizes, specifically between 350 and 400 μm, allows ECs to grow in the three dimensions, as reported *in vivo* by Bonfield (Bonfield, 2006). In addition, SEM analysis showed that MAEC DsRed displayed their peculiar dendritic morphology only over S2 and S3 microporosities, with many cell-to-cell interactions and connections, a clear sign of cellular wealth. However, the results in the *in ovo* model evidenced a comparable angiogenic effect among the different microporosities, likely due to the scaffold 3D structure. Indeed, smooth and tall biomaterials cannot be easily investigated using this model since they do not promote CAM cell adhesion and tissue ingrowth, confirming what reported by Valdes *et al*. (Valdes et al., 2002). This data clearly indicates that the CAM model is more predictive about biomaterials designed with a rough surface and small thickness, like thin films.

After the identification of a suitable microporosity, the effect of biosourced and functionalized CNCs suspended in PHBH matrix was evaluated. CNCs were previously acetylated to achieve a higher polymer–filler interaction and to improve the chemical affinity between the hydrophobic biopolymer matrix and the hydrophilic cellulose. NMR spectra clearly indicates that the functionalization of CNCs surface positively occurred, since the modifications of the spectra are comparable to the data reported in literature (Jebrane and Sèbe, 2007; Tingaut et al., 2010). Therefore, the substitution of the hydroxyl groups with the acetyl groups in CNCs allowed carbonyl interactions with the PHBH ester chain.

To investigate the biocompatibility of PHBH–CNC biocomposites, films of neat PHBH and 5, 10, 15, and 20 wt% of CNCs compounded to the biopolymer matrix were printed and hot-pressed,

simulating bidimensional materials. Our results illustrate that after 48 h MAEC DsRed proliferated over all the biocomposites in a comparable manner, whereas after 72 h PHBH 10% CNCs obtained the highest results, followed by PHBH 15% CNCs. In addition, SEM analysis showed the dendritic morphology of MAEC DsRed and many cytoplasmic protrusions that connected cells to each other, especially in these two formulations. Taken together, all these data demonstrate the biocompatibility of the PHBH-CNC biocomposites, indicating that the compounding with CNCs has enhanced the cell growth rate over the films compared to neat PHBH.

The same films, without cells, were also grafted onto the CAM to evaluate their angiogenic potential. Interestingly, the CAM assay confirmed that PHBH 10% CNCs and, to a minor extent, PHBH 15% CNCs displayed visible vascular reactions, with vessels sprouting from radially from the films like spokes in a wheel. In addition, PHBH 10 and 15% CNCs also allowed the highest embryos viability at ED12. Taken together, these results clearly evidence that the biocomposite films with the *in vitro* and *in ovo* highest angiogenic potential are PHBH 10 and 15% CNCs.

Finally, from these preliminary results, S3 microporosity was selected to print PHBH scaffolds with 10% and 15% of CNCs. PHBH compounded with 10% of CNCs allowed a better colonization than neat PHBH or with 15% CNCs. The addition of CNCs to PHBH as mechanical reinforcement also improved the adhesion rate of ECs in the three dimensions, making the material more attractive for their growth. Once again, the CAM assay showed a visible but comparable vascular reaction among the three biocomposites, confirming our previous hypothesis: the different spatial configuration between the films and the scaffolds influenced the development of vessels onto the CAM. In fact, when comparing different structures of the same material, the angiogenic reaction of the films was higher compared to the one of the scaffolds. Overall, this data confirms that the CAM model demonstrated high sensitivity to assess minimal differences in CNCs concentration, while being less predictive in testing the angiogenic potential of thick scaffolds.

Taken together, the results lay the foundation for the *in vivo* testing of PHBH 10% CNCs scaffolds, to demonstrate that this formulation could trigger vascularization in bone lesions and is suitable for BTE applications in the future.

1.5 *Conclusion*

In this research work, 3D-printed biobased scaffolds were successfully fabricated through FFF technique with a suitable control over the filling geometries. First, the effect of scaffold microporosity on ECs *in vitro* and their angiogenic response *in ovo* were investigated. The results indicated that the geometry with 350–400 μm pore size displayed the suitable 3D colonization by ECs, while the CAM assay had confirmed the angiogenic potential of PHBH porous scaffolds, without noticeable differences. Secondly, PHBH matrix was successfully compounded with acetylated CNCs at four different concentrations varying from 0 to 20 wt%. *In vitro* and *in ovo* investigation on bidimensional films harmoniously indicated 10 and 15% CNCs as the most promising formulations. Instead, PHBH 20% of CNCs denoted a lower proliferation rate, but similar to neat PHBH. Finally, PHBH 10 and 15% CNCs 3D-printed scaffolds with 350–400 μm microporosity were investigated in terms of ECs adhesion, proliferation and angiogenic potential. The findings gave clear indication that 10 wt% of acetylated CNCs enhanced PHBH biocompatibility and proliferation rate *in vitro,* although the angiogenic potential of the different scaffolds was comparable *in ovo*.

In conclusion, the developed biocomposites possess favourable properties for EC growth, allowing scaffold colonization and cell-to-cell interactions that are essential to promote vascularization, preliminary to all bone regenerative processes. Moreover, PHBH–CNC films demonstrated a promising angiogenic potential *in ovo,* suggesting that, once implanted, these materials could trigger vascularization *in vivo* as well. Taken together the results suggest PHBH 10% CNCs with 350-400 μm microporosity as a promising 3D-printed scaffold for BTE applications.

2. CHAPTER II: BONE POWDER

2.1 *Introduction*

Scleral ossicles (SOs) are peculiar bone segments, localized at the scleral-corneal border of the eyeballs of lower vertebrates and arranged in a ring to protect the eye during activities with high pressure or compression, such as flying or swimming. Interestingly, SOs are naturally decellularized since bone cells undergo massive apoptosis at the end of the embryonic development (Franz-Odendaal and Hall, 2006; Palumbo et al., 2012). This characteristic is of huge importance because it avoids the time-consuming and expensive decellularization processes that are necessary to prevent the transplant rejection. Moreover, it prevents the pathogen transmission from human donors (allografts) or animals (xenografts) (Roseti et al., 2017). In addition, SOs have demonstrated to be biocompatible and able to sustain *in vitro* cell adhesion, proliferation and differentiation. Once implanted *in vivo*, they also displayed a non-immunogenic reaction and an evident angiogenic potential: for all these reasons, SOs appear promising biomaterials for BTE applications (Checchi et al., 2020, 2017).

However, the peculiar geometry of SOs makes difficult their translation into the clinical scenario: in fact, since they are small bone plates, they cannot be easily tailored according to the lesion dimensions. For this reason, we tried to create SO-derivatives to be integrated into support scaffolds; in particular, SOs were grinded into fine bone powder with the purpose of enhancing their usability in BTE applications while maintaining their useful properties. The powder is a very versatile formulation because it allows the printing of the particulate blended within soft biomaterials, like hydrogels, in customized 3D scaffolds. Thus, this part of the project aims at exploring the possibility of creating porous scaffolds through a micro-extrusion bioprinting technique. The major advantage of micro-extrusion bioprinting is the production of anatomically shaped scaffolds with great precision and structural integrity. In fact, the layer-by-layer deposition of continuous filaments extruded by the

printer micro-nozzle allows the creation of patient-specific 3D scaffolds that could be easily used in tissue engineering applications (Yilmaz et al., 2019). Hydrogels surely represent the most popular bioinks in tissue engineering applications due to their high availability, great biocompatibility, low costs and tailorable proprieties. The choice of the suitable bioink is a crucial step toward successful micro-extrusion bioprinting. Ideally, it should display some fundamental characteristics: firstly, high biocompatibility and a tissue-like composition to mimic cell natural environment; secondly, adequate viscosity to print 3D geometries with high precision; thirdly, mechanical consistency to retain the structure after printing; finally, tailorable features to easily modify the scaffolds onto patients' needs, while maintaining high reproducibility on the printing process (Gungor-Ozkerim et al., 2018). Clearly, the selection of the bioink depends on the application: as already described, bone cells require an ECM with peculiar porosity and mechanical stiffness. One of the most common natural hydrogels is collagen, which is the primary organic constituent of connective tissues like bone. Type I collagen, in particular, is highly used in tissue engineering because of its availability, biomimetic properties, biocompatibility and low antigenicity (Caliari and Burdick, 2016). Similarly, hyaluronic acid (HA) is a ubiquitous polysaccharide in the ECM, which has the ability to interact with the cells and growth factors involved in bone formation. In addition, its hydrophilic nature promotes the formation of hydrogels with high viscosity, biocompatibility and biodegradability (Hwang and Lee, 2023).

Currently, the most popular hydrogels have an hybrid composition: essentially, they are natural hydrogels chemically-modified with functional groups to enhance the adhesion between molecules and to increase mechanical proprieties (Ozbolat, 2016). Gelatin is a derivative of collagen, which has been modified through the physical blending with methacrylate. In gelatin methacryloyl (GelMA) the amine groups on the side chains of gelatin are replaced by methacryloyl groups, which enable photo-crosslinking with UV light exposure in presence of a photo-initiator. Photo-crosslinked GelMA still exhibits high biocompatibility and proper degradability, with the addition of improved mechanical strength and stability (Sun et al., 2018).

In the last years, graphene oxide (GO) has gained particular attention due to its ability to improve bone cell proliferation, growth and differentiation *in vitro* (Koons et al., 2020). GO is a thick carbon sheet obtained by the oxidative exfoliation of graphite that, due to its large surface area and abundant hydrophilic functional groups, such as hydroxyl, epoxide and carbonyl, it allows a wide range of chemical modifications (Zhang et al., 2021). For this reason, graphene-based hydrogels have been exploited to improve bone regeneration and the characteristics of other biomaterials for different applications in the biomedical field (Lu et al., 2017).

In this study, the SOs powder, from this moment on named Pal-OS® as subject of trademark filing, was blended with different hydrogels (type I collagen, GelMA, HA and GO) and printed into porous 3D scaffolds by means of a micro-extrusion bioprinting technique. The final aim was to find the suitable hydrogel formulation to print the Pal-OS® powder, to optimize the expression of the angiogenic potential of SOs also in the scaffold form for BTE applications.

2.2 *Materials and methods*

2.2.1 SOs extraction and Pal-OS® powder fabrication

The eyeballs of adult chickens, gently donated from a local butcher, were incised with a scalpel to remove the scleral rings. The SOs were disjoined one by one by removing the tissue membranes that cover the scleral ring; 13–14 SOs were extracted from each eyeball. Then, they were cleaned with 1× PBS, dried and finally sterilized under UV radiation. The Pal-OS® powder was obtained by grinding the SOs with a mortar and then sifting the particulate matter with a 200 µm strainer, to obtain a homogeneous size of the particles. To confirm the granulometry, the Pal-OS® powder was prepared for the SEM analysis, as already described (Chapter 1, Paragraph 1.5) and analysed with the ESEM Quanta 200 SEM (Fei Company, Hillsboro, OR, USA). The particulate matter was measured with the

ImageJ software (v1.8.0_101, National Institutes of Health, Bethesda, MD, USA) by analysing different micrographs. Finally, the powder spectrum was analysed via X-ray microprobe (X-ray energy dispersion spectroscopy, X-EDS) using the ESEM software INCA Suite (version 4.07, Oxford Instruments Analytical, Tubney Woods, Abingdon, Oxon, UK).

2.2.2 Micro-extrusion bioprinting and hydrogel preparation

All the printing processes were conducted using a micro-extrusion 3D printer (3D Bioplotter®, EnvisionTEC GmbH, Gladbeck, Germany) placed within a sterile flow hood cabinet and equipped with a low-temperature printing head (operating temperature range of 0-50°C). A customized CAD project was developed to fabricate parallelepiped-shaped structures, each measuring 5 mm on the base sides and approximately 1 mm in height. This architecture comprised four layers, each with a slicing height of 260 µm. The infill pattern was composed of a grid with lines spaced 1.25 mm apart. Collagen structures were realized by diluting highly concentrated (35 mg/ml) type I collagen Lifeink® 200 (Advanced BioMatrix, Carlsbad, CA, USA) in PBS at a volume ratio of 5:1.

GelMA-based bioinks (Sigma Aldrich, Darmstadt, Germany), with a gel strength of 300 g Bloom and degree of substitution 60%, were prepared by dissolving GelMA powder in 1× PBS, sterilizing through filtration, and subsequently adding pre-sterile components: photo-initiator lithium phenyl-2,4,6-trimethylbenzoylphosphinate (LAP) (Sigma Aldrich, Darmstadt, Germany), hyaluronic acid Sinovial HL 32 (IBSA, Lodi, Italy), graphene oxide (Graphenea, San Sebastián, Spain) and Pal-OS® powder. The solutions were mixed by mechanical stirring.

Following preparation, the bioinks were carefully loaded into a 30 ml syringe equipped with a needle and a piston (all Nordson, Westlake, Ohio, USA). The syringe was connected to the low-temperature printing head and maintained at the optimal temperature throughout the process. The printing process parameters are summarized in Table II.1.

After printing, the 3D structures underwent specific crosslinking processes. Collagen scaffolds underwent thermal crosslinking by maintaining them at 37°C for at least 30 minutes post printing. In contrast, GelMA structures were crosslinked through UV irradiation (170 mW/cm²) for 10 seconds on the entire scaffold, except for GO scaffolds, which were irradiated after the completion of each layer, due to the light-shielding effect of the dispersed black powder in the hydrogel. Following crosslinking, the 3D structures were stored at 4°C in 1× PBS.

Ink	Composition (% w/v)	Pressure (bar)	Printing speed (mm/s)	T Head (°C)	T Plate (°C)	Needle (Gauge)	Cross linking
Collagen	Type I collagen 2.9%	0.22-0.3	5	4°C	37°C	25	Thermal
GelMA	GelMA 6% + LAP 0.05%	0.6-0.7	4-5	24°C	6°C	22	UV
GelMA+ Pal-OS®	GelMA 6% + LAP 0.05% + Pal-OS® 50%	0.5-0.7	4-5	24°C	6°C	22	UV
	GelMA 6% + LAP 0.05% + Pal-OS® 70%	0.5-0.7	4-5	24°C	6°C	22	UV
GelMA+HA	GelMA 6% + LAP 0.05% + HA 10%	0.6-0.7	4.5-4.8	24°C	6°C	22	UV
GelMA+HA+ Pal-OS®	GelMA 6% + LAP 0.05% + HA 10% + Pal-OS® 50%	0.7	4.5	24°C	6°C	22	UV
	GelMA 6% + LAP 0.05% + HA 10% + Pal-OS® 70%	0.5-0.7	4.5	24°C	6°C	22	UV
GelMA+GO	GelMA 6% + LAP 0.05% + GO 2.5%	0.5-0.6	4.5	24°C	6°C	22	UV
	GelMA 6% + LAP 0.05% + GO 5%	0.45-0.6	4.5	24°C	6°C	22	UV

Table II.1. Bioinks compositions, printing parameters and crosslinking techniques.

2.2.3 CAM assay

Fertilized Isa Brown chicken eggs (Azienda Agricola Cellini Andrea, Forlì, Italy) were placed into the Mercurius MG244 incubator (FIEM, Como, Italy) at 37.8°C in constant humidity conditions. The CAM assay was performed as previously described (Chapter I, Paragraph 1.2.6) by grafting the 3D-printed scaffolds onto the CAM at ED8. Six eggs were used for each condition and all experiments were carried out in independent triplicate. A sterile, inert, haemostatic, absorbable, porcine gelatin

sponge (Spongostan™, Ferrosan Medical Devices, Søborg, Denmark) was used for the positive and negative controls. In particular, the sponge was soaked in 1× PBS for the negative controls, whereas was saturated with VEGF-A 100 ng/ml for the positive controls, according to Oranger's protocol (Oranger et al., 2017). The images were acquired on ED12 by using SMZ745T stereomicroscope (Nikon Instruments Europe BV, Amstelveen, The Netherlands) equipped with a digital camera and Xentry software (both Alexasoft, Florence, Italy) at 1× magnification.

2.2.4 Angiogenic response evaluation

The vessel count was performed starting from the images of the ED12 CAMs at 1× magnification; for each sample, the same round area surrounding the grafted materials was chosen. To evaluate the angiogenic response, WimCAM, a WIMASIS Image Software for CAM assays, was exploited (https://www.wimasis.com/en/WimCAM). This tool analyses the neo-formed vessels sprouting radially from the grafted materials, by examining mainly three parameters: the vessel density is the percentage of covered area by tubular structures in the whole area of the image, calculated by dividing the total number of pixels of the image by the pixels that belong to the tubular structure; the total vessel network length measures the complete length of the tubular structure in pixels: in WimCAM, a tube is the part of the tubular structure between two branching points or a branching point and a loose end; the total branching point is the count of branching points in the image, i.e. parts of the tubular structure where three or more tubes converge.

2.2.5 Histology

Samples from the CAMs grafted with the scaffolds were washed in 1× PBS and then fixed with 4% paraformaldehyde/PBS (Sigma Aldrich, Darmstadt, Germany) overnight (O/N) at 4°C. The scaffolds containing the Pal-OS® powder were also decalcified in ethylenediaminetetraacetic acid (EDTA) 10% for four days. Then, all the samples were dehydrated through the ascendant alcoholic scale (70,

80, 90 and 100% ethanol, an hour each) until xylene, and subsequently embedded in paraffin (all Histo-Line Laboratories, Milan, Italy). Sections of 4 μm of thickness were obtained through LEICA RM2255 microtome (Leica Biosystems, Wetzlar, Germany); once the sections were placed over glasses, they were placed in xylene for an hour, and then hydrated through the descendant alcoholic scale (100, 90, 80 and 70% ethanol, 30 min each). Sections were stained using Carazzi's hematoxylin and eosin/phloxine B solution (both Histo-Line Laboratories, Milan, Italy) according to the manufacturer's procedure. Sections were subsequently dehydrated through ascendant alcoholic scale (from 80 to 100% ethanol), cleared in xylene and cover-slipped with DPX mountant (Sigma-Aldrich, Milan, Italy) for imaging. Images were acquired at 20X and 40X magnification under Eclipse Ni-E light microscope (Nikon Instruments Europe BV, Amstelveen, Netherlands).

2.2.6 Statistical analysis

At least three different experiments were performed for each analysis. All data are expressed as mean±SD. Differences between the experimental conditions were evaluated by one-way ANOVA with Bonferroni's correction for multiple comparisons. The type of analysis and significant p-values are shown in figure legends. Differences are classified as significant with $p < 0.05$. Statistical analysis and relative graphs were elaborated with GraphPad Prism 6 (version 6.01, San Diego, USA).

2.3 *Results*

2.3.1 The Pal-OS® powder maintained the biological properties of SOs

First, the Pal-OS® powder was characterized and tested for biocompatibility. The microanalysis, reported in Figure II.1, showed that the most common elements of the Pal-OS® powder are oxygen (53.52%), carbon (33.57%) and calcium (8.51%), followed by magnesium (2.04%), phosphorus (1.53), sodium (0.48%) and chlorine (0.35%).

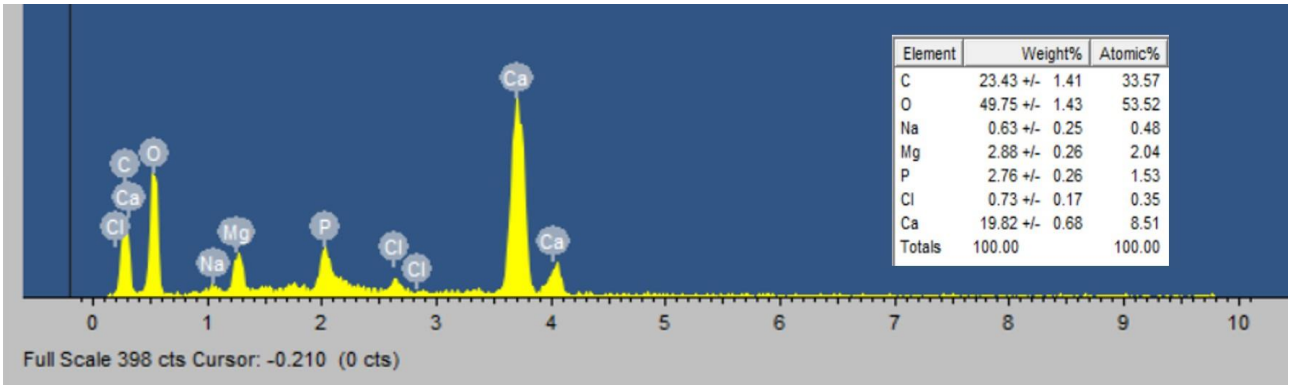

Figure II.1. Microanalysis of the Pal-OS® powder. The elements are reported in the table with their weight and atomic percentages.

Then, the Pal-OS® powder was sieved to obtain a homogeneous particulate matter. Since the needle internal diameter is 22 Gauge (G), which corresponds to approximately 400 µm, the powder particles dimensions should be inferior not to obstruct the nozzle during the printing procedure. The SEM analysis revealed that the sieved powder had dimensions inferior to 200 µm: in particular, the analysis with the ImageJ software showed that the mean of the particles is 178 $\pm$ 68 µm, as reported in Figure II.2.

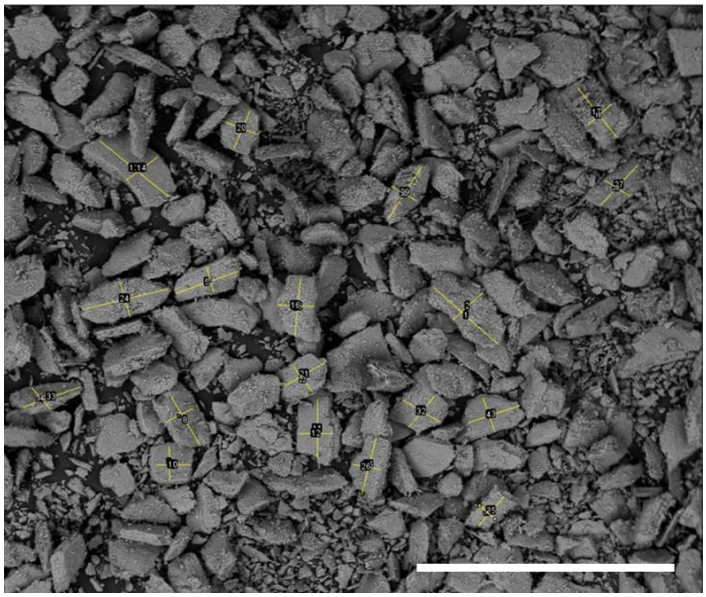

Figure II.2. SEM micrograph showing Pal-OS® powder granulometry. The mean ± SD of the Pal-OS® particulate calculated by the ImageJ software is 178 ± 68; scale bar 1 mm.

In addition, in test the Pal-OS® powder biocompatibility, the CAM assay was exploited. The SOs and the Pal-OS® powder were compared to standard negative and positive controls, *i.e.* an inert sponge soaked with 1× PBS or VEGF-A, respectively. As shown in Figure II.3, both SOs and the Pal-OS® powder displayed a visible angiogenic reaction, similar to the positive control and higher than the negative control.

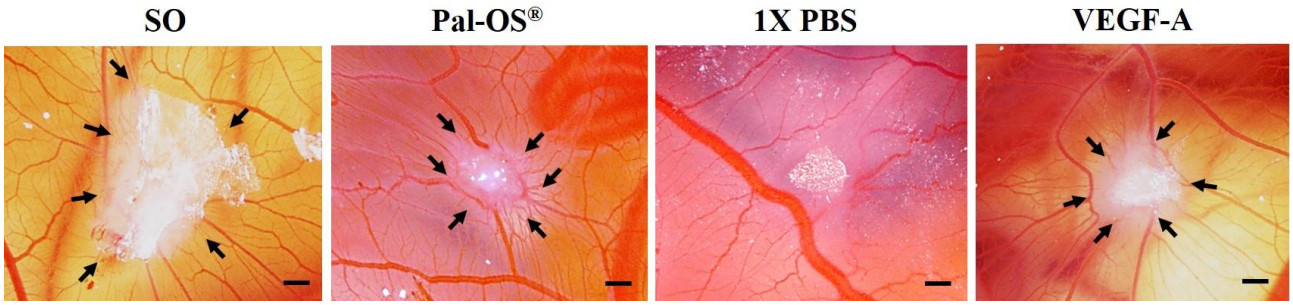

Figure II.3. CAM assay of SO, Pal-OS® powder and the negative (1× PBS) and positive (VEGF-A) controls; the angiogenic reaction is evidenced with arrows; magnification 1X, scale bar 250 µm.

2.3.2 GelMA scaffolds displayed higher structural integrity than type I collagen

To print the Pal-OS® powder with a micro-extrusion technique, the particulate matter should be blended within a viscous material, like a hydrogel: for this purpose, GelMA and type I collagen were chosen. The two hydrogels without the Pal-OS® powder were printed in a grid-like porous structure, as described. As reported in Figure II.4, after 4 days of incubation onto the CAM at physiological temperature and constant humidity, the collagen scaffolds completely lost their structural integrity, whereas GelMA hydrogels maintained their 3D conformation. For this reason, GelMA hydrogels were chosen as base bioink to print the Pal-OS® powder.

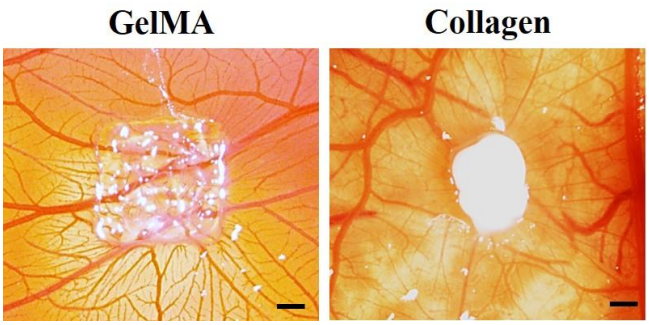

Figure II.4. CAM assay. GelMA and type I collagen at ED12; magnification 1X, scale bar 250 µm.

2.3.3 GelMA did not display the angiogenic potential of the Pal-OS® powder

The Pal-OS® powder was printed within GelMA at different concentrations to evaluate which percentage of bone powder may trigger the highest *in vivo* angiogenic potential. Preliminary results suggested that percentages inferior to 50% of Pal-OS® powder in GelMA were not able to express a higher angiogenic reaction to the control CAMs; instead, for percentages superior to 70% the 3D-printed structure could not maintain its integrity. For this reason, we focused on printing scaffolds with 50 and 70% of Pal-OS® powder within GelMA. The angiogenic reaction of the scaffolds, reported in Figure II.5a, was quantified through the WimCAM software and in Figure II.5b are reported the results for the three parameters analysed. In particular, for the vessel density GelMA scaffolds were significantly more pro-angiogenic than the controls (CTR). Moreover, for the total

vessel network length the scaffolds with GelMA displayed an angiogenic reaction significantly higher than the ones with 50% of Pal-OS®.

The histological analysis indicated that all the scaffolds were positively included by the CAM tissues: in fact, Figure II.5c shows how the cells surrounded each hydrogel arranging in organized multilayered structures. On the other hand, the CAM cells also highly proliferated surrounding the Pal-OS® powder particles. The H&E staining revealed that the cells near the hydrogels produced a different tissue formation compared to the ones surrounding the Pal-OS® powder: in fact, in the first case, they produced a multilayered structure (black head-arrows), whereas in the second case the cells were surrounded by a matrix (white head-arrows). However, no vessels were observed near the hydrogels or the Pal-OS® particles.

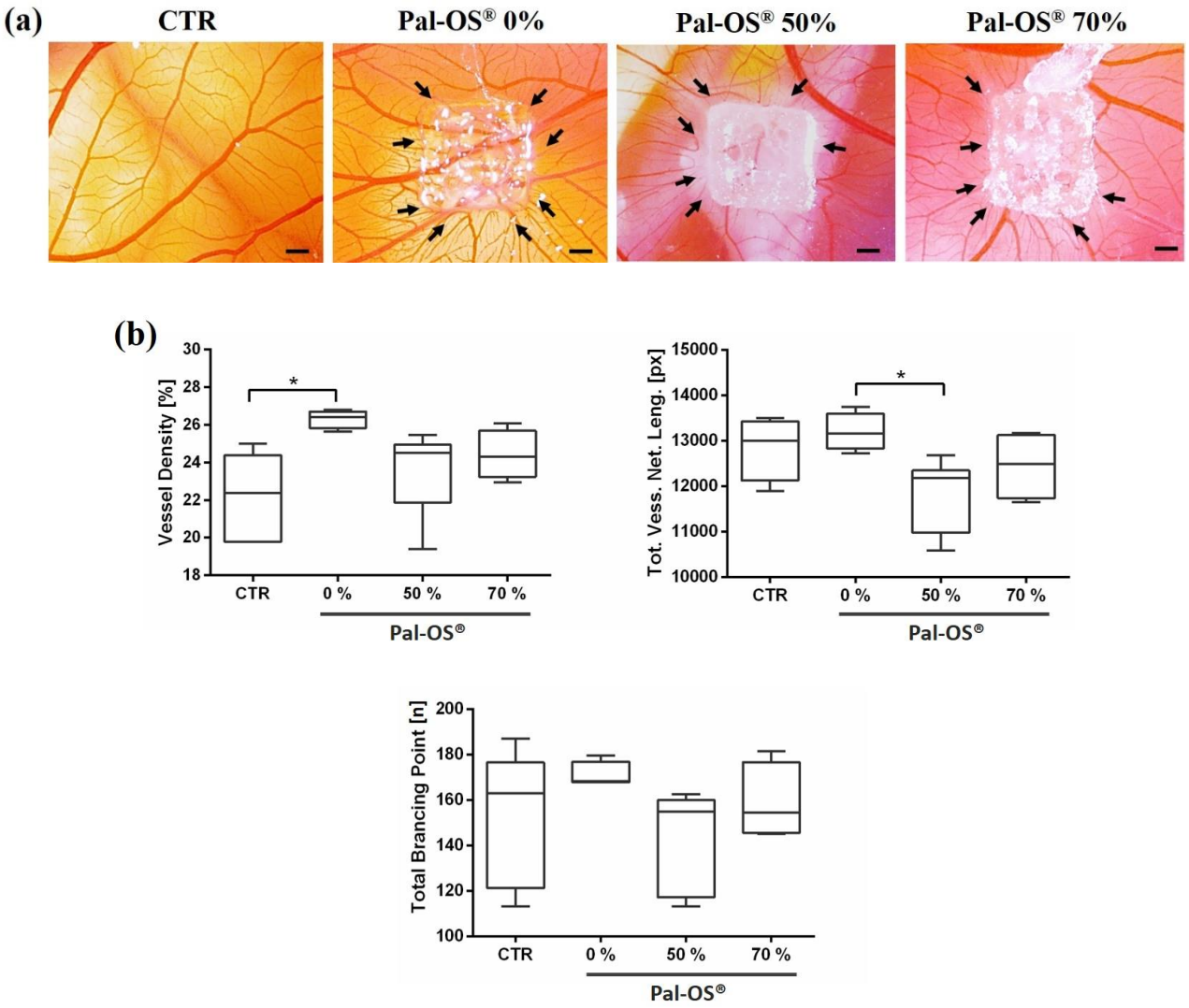

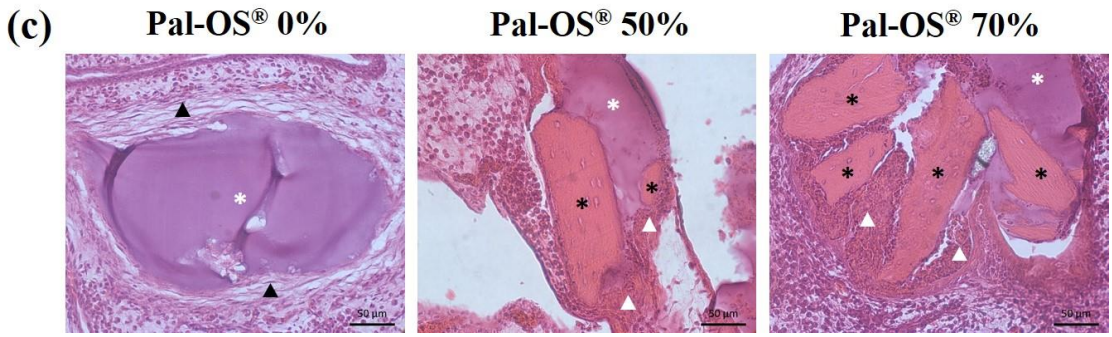

Figure II.5. Angiogenic evaluations of GelMA, GelMA-Pal-OS® 50% and 70% scaffolds. a) CAM assay: the black arrows indicate the angiogenic reaction; magnification 1X, scale bar 250 µm. b) Quantification of the angiogenic reaction of the scaffolds with WimCAM software: analysis of three parameters (vessel density, total vessel network length, total branching point) and statistical analysis (*$p \leq 0.05$). c) Histology of the CAM tissues and the scaffolds: cell nuclei in purple (hematoxylin), cytoplasms in pink (eosin); white asterisks indicate the hydrogel, black asterisks the powder particles and the head-arrows the CAM tissue (in white the connective-like tissue, in black the multilayered structure); magnification 40X, scale bar 50 µm.

2.3.4 The addition of HA to GelMA did not improve the scaffolds' performance

To enhance the scaffold performance, 10% of HA was added to the bioinks with GelMA and the Pal-OS® powder at 50% and 70%. The CAM assay in Figure II.6a showed that all the scaffolds with HA did not display a visible angiogenic reaction. This data was confirmed by statistical analysis that reported no significant differences among the scaffolds compared to the controls, as shown in Figure II.6b.

The histological analysis revealed that the CAM cells highly proliferated around the hydrogels and the powder, positively including the scaffolds. The sections reported in Figure II.6c show the presence of different tissue formations, often accompanied by an amorphous matrix around the hydrogels. However, this data should be further characterized.

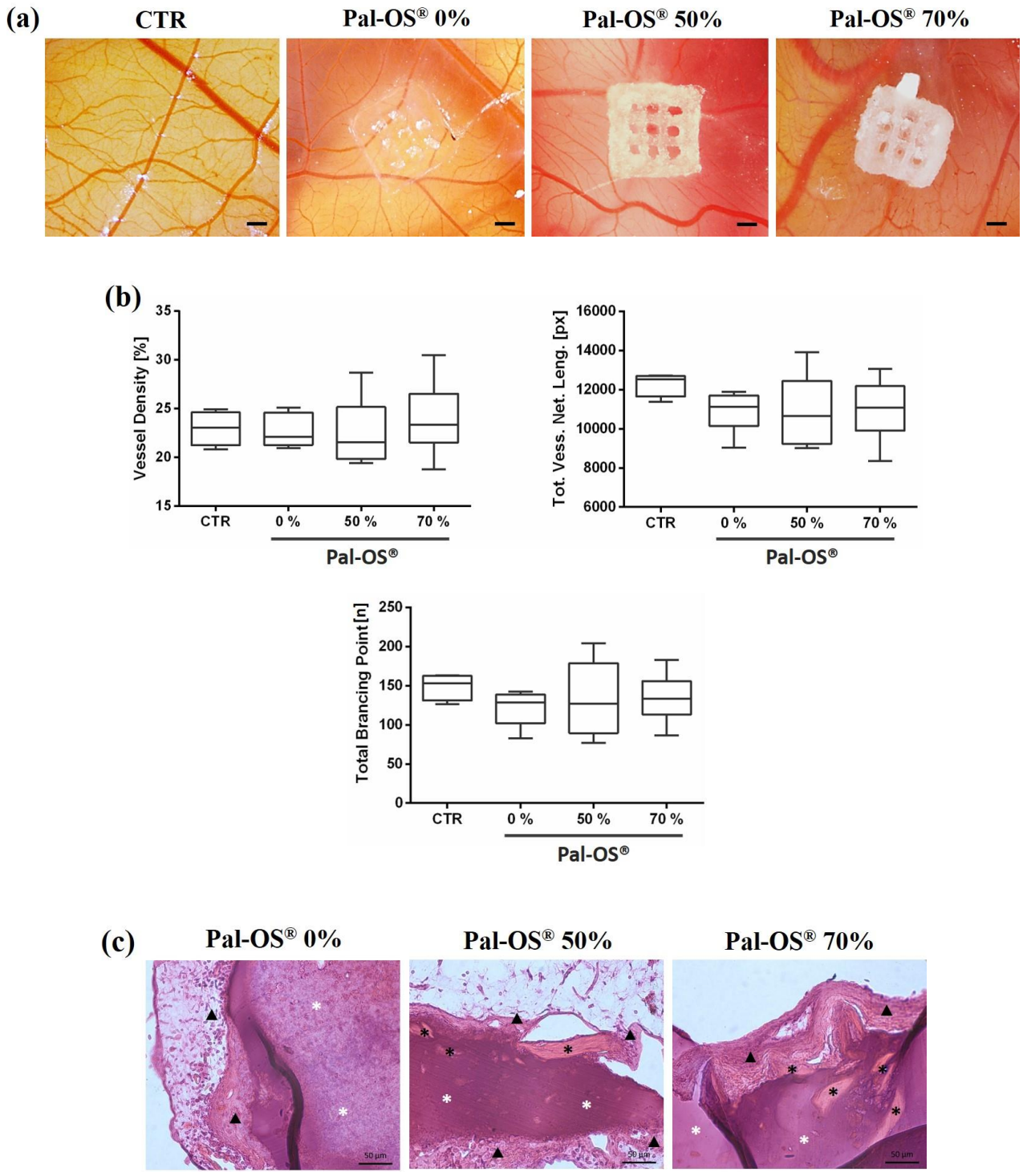

Figure II.6. Angiogenic evaluations of HA-GelMA, HA-GelMA-Pal-OS® 50 and 70% scaffolds. a) CAM assay: magnification 1X, scale bar 250 µm. b) Quantification of the angiogenic reaction of the scaffolds with WimCAM software: no statistical differences were observed. c) Histology: cell nuclei in purple (hematoxylin), cytoplasms in pink (eosin); white asterisks indicate the hydrogel, black asterisks the powder particles and the black head-arrows the CAM tissue of neo-formation; magnification 40X, scale bar 50 µm.

When the data of HA scaffolds are compared to the ones with GelMA, the first material always show a lower angiogenic potential than the latter. In Figure II.7 this data is evident for the scaffolds presenting only the hydrogels without the Pal-OS® powder: GelMA is always statistically more pro-angiogenic than HA for the three parameters analysed. Only for the vessel density, GelMA is also more pro-angiogenic than the controls. Moreover, GelMA always shows a significantly higher angiogenic response in comparison to HA with 50% of Pal-OS® powder.

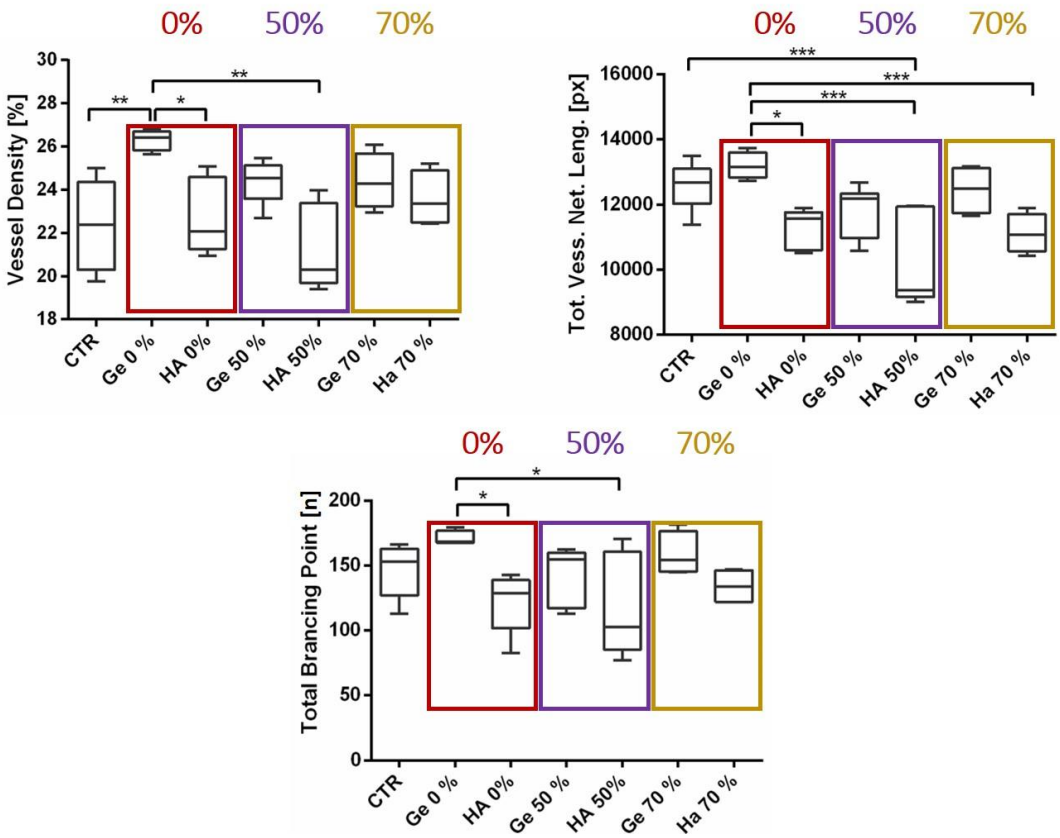

Figure II.7. Comparison between HA and GelMA scaffolds. In red the hydrogels with 0% Pal-OS®, in purple scaffolds with 50% Pal-OS®, and in yellow the ones with 70% Pal-OS®. Quantification of the angiogenic reaction of the scaffolds with WimCAM software: analysis of three parameters and statistical analysis (*$p \leq 0.05$, **$p \leq 0.01$, ***$p \leq 0.001$).

2.3.5 Lower concentrations of GO resulted in higher angiogenic reactions

Similarly, GO was added to GelMA at different concentrations, from 2.5 to 10%, and the relative scaffolds were printed. However, the scaffolds with concentrations of GO superior to 5% could not retain their 3D structure, dissolving onto the CAM. Instead, as shown in Figure II.8a, the scaffolds with 5% or inferior concentrations of GO maintained their structural integrity: for this reason, we focused on 2.5 and 5% of GO. The CAM assay showed that both concentrations gave positive results in terms of angiogenic response, however, as reported in Figure II.8b, the WimCAM analysis indicated that GelMA alone had a significant higher angiogenic potential in comparison to 5% GO for the total vessel network length and the total branching points. In addition, only for the total branching points, the controls and 2.5% GO displayed a significantly higher angiogenic potential in comparison to 5% GO.

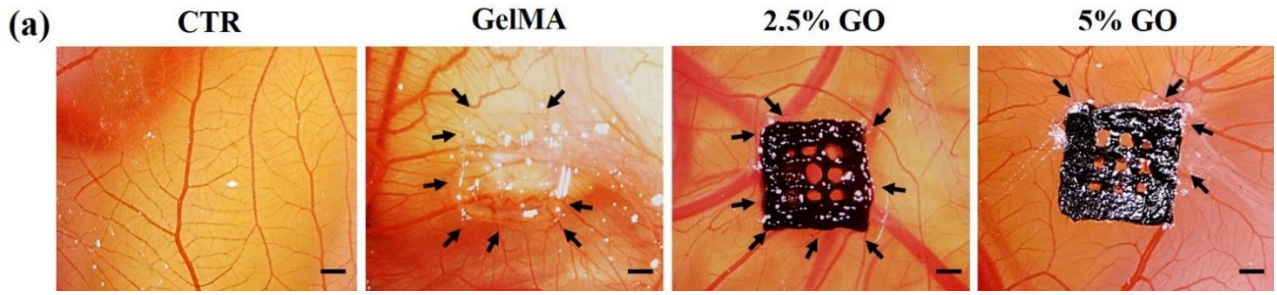

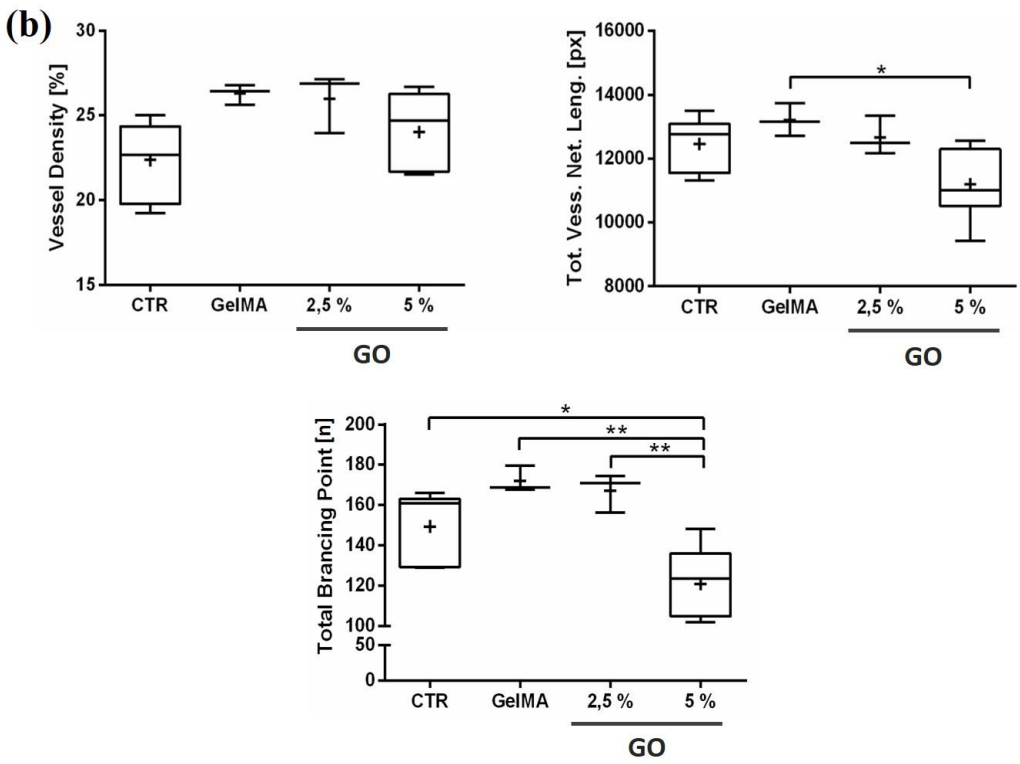

Figure II.8. Angiogenic evaluations of GelMA-GO scaffolds. a) CAM assay of GO scaffolds at different concentrations, from 2.5% to 5% in GelMA; the black arrows indicate the angiogenic reaction; magnification 1X, scale bar 250 µm. b) Quantification of the angiogenic reaction of the scaffolds with WimCAM software: analysis of three parameters and statistical analysis (*$p \leq 0.05$, **$p \leq 0.01$).

2.4 *Discussion*

In this study, SOs were mechanically fragmented into fine powder, called Pal-OS®, blended with different hydrogels and printed with a micro-extrusion bioprinting technique in 3D porous scaffolds. Then, they were directly tested *in vivo* by means of the CAM assay to evaluate the vascular response for future applications in BTE.

First, the Pal-OS® powder was characterized through the microanalysis. Checchi *et al*. already investigated the structure and the properties of SOs (Checchi et al., 2020, 2017), but this analysis wanted to further investigate their atomic composition and the preservation of SOs biological

properties. The microanalysis confirmed that the ions found are those typical of bone tissue: in fact, there are anionic species such as HPO_4^{2-}, CO_3^{2-} and Cl^-, and cationic like Ca^{2+}, Na^+ and Mg^{2+} (Von Euw et al., 2019). This result suggests that the Pal-OS® powder has maintained the properties of SOs at biological level without alterations. To investigate further this hypothesis, the powder was tested *in ovo* and compared to SOs: the visible angiogenic reaction confirmed the biocompatibility and the angiogenic potential of Pal-OS®.

In order to print the Pal-OS® powder in 3D scaffolds through a micro-extrusion technique, the choice of the bioink was between GelMA and type I collagen, that surely represent the most exploited hydrogels in BTE for their versatility and good biological properties (Gungor-Ozkerim et al., 2018). The chosen geometry was a grid-like porous structure: in fact, the porosity of the scaffold is of huge importance in bone, since it favours the exchange of molecules and the cell-to-matrix interactions (Bonfield, 2006). Interestingly, type I collagen constructs could not retain their geometry *in ovo*, whereas GelMA hydrogels showed high structural integrity. This result suggests that the thermal crosslinking of collagen scaffolds was not sufficiently effective to stabilize the structure after the printing process, whereas the photo-crosslinking in GelMA hydrogels was able to maintain their integrity. The maintenance of 3D structure after printing represents a challenging parameter: in fact, the culture conditions tend to degrade most hydrogels. For this reason, the fabricated scaffolds are usually stabilized by crosslinking techniques soon after the printing process. In this context, photo-polymerization under UV light is a type of chemical crosslinking that provides an increased stability and excellent mechanical properties in the printed scaffolds due to the strong and permanent covalent bonds created (Ozbolat, 2016). Consequently, GelMA was identified as the most suitable bioink to print the Pal-OS® powder.

Then, two different preliminary tests were conducted to assess: 1) if the Pal-OS® particulate would have obstructed the nozzle during the extrusion process, and 2) which concentration of powder inside GelMA was the most suitable. The printing tests confirmed that the sieving procedure had produced

a homogeneous particulate with dimensions lower than 200 µm: as expected, Pal-OS® did not obstruct the 22 G needle during the extrusion. This is also a proof that the Pal-OS® powder was homogeneously dispersed inside the bioink, which also enabled the production of highly precise and reproducible geometries. Subsequently, tests conducted to define the appropriate concentration of Pal-OS® in GelMA indicated that adequate percentages to show valuable angiogenic reactions and to maintain the structural integrity of the scaffolds are those between 50% and 70%. A possible explanation is that when the ratio GelMA-Pal-OS® is in favour of the hydrogel, it could somehow "hide" the angiogenic potential of the powder. Instead, when the ratio GelMA-Pal-OS® is in favour of the powder, the residual quantities of hydrogel could not retain the printed structure through the crosslinked bonds.

Once defined that the range to print the Pal-OS® powder was between 50 and 70% in GelMA, the scaffolds were produced and tested *in ovo*. Even if they displayed a visible angiogenic reaction, the ones with Pal-OS® showed no significant differences in response compared to GelMA. This data was also confirmed by the WimCAM software, especially for the total vessel network length in which the scaffolds with GelMA alone displayed an angiogenic reaction significantly higher than the ones with 50% of Pal-OS® for the total vessel network length and the controls for the vessel density. Overall, it seems that GelMA itself has an angiogenic potential that could have partially hided Pal-OS® properties, but this hypothesis requires further investigations.

At histological level, the hydrogels were positively included by the CAM tissue and the cells highly proliferated around the scaffolds, confirming their biocompatibility. In particular, the cells near the hydrogels organized in multilayer arrangements, typical of an epithelial tissue, whereas next to the powder the cells deposited a matrix forming a simil-connective tissue. Interestingly, this data suggests that the Pal-OS® particles may have induced the cells to produce an osteogenic matrix. Moreover, any vascular formation was spotted near the scaffolds, confirming that they did not trigger high angiogenic responses.

To diminish the quantity of GelMA and consequently to allow Pal-OS® to display its peculiar properties, 10% HA was added to the bioinks. HA is also reported to interact with bone cells and growth factors involved in bone formation (Hwang and Lee, 2023). However, the results unambiguously indicated that all the HA scaffolds, with or without the Pal-OS®, did not display a significant angiogenic reaction. These results suggest that the addition of HA had an overall negative effect onto the angiogenic potential of all the scaffolds, also indicating that the reduction of the percentage of GelMA did not improve Pal-OS® angiogenic properties. Moreover, the histological analysis of HA scaffolds reported a high proliferation of the CAM cells, but without organization around the hydrogels and, as expected, no vascular formations, confirming the negative effect of HA. To better understand the differences between the two bioinks, GelMA and HA-GelMA scaffolds were compared. GelMA showed significant more pro-angiogenic effects compared to GelMA-HA scaffolds. This finding confirms that the adding of HA negatively affected the angiogenic potential of GelMA-Pal-OS® scaffolds. Many studies reported that depending on its molecular weight, HA could display opposing actions, *viz.* promoting or inhibiting angiogenesis (Marinho et al., 2021). For example, Cyphert *et al*. reported that high molecular weight HA has an anti-inflammatory and anti-angiogenic effect in different models (Cyphert et al., 2015). A possible explanation could be that the HA bioink used, with a hybrid composition between high and low molecular weight molecules, exploited an anti-angiogenic effect in the CAM context. However, further investigations are required to confirm this hypothesis.

Then, GO was added to GelMA bioinks in order to study this innovative and promising material and its eventual angiogenic potential, which was not still characterized in literature. We chose GO because it has shown to improve the mechanical properties of the scaffolds, as well as the osteoinductivity, when in combination with other hydrogels (Lu et al., 2017). Preliminary test *in ovo* indicated that scaffolds with concentrations of GO superior to 5% were not able to maintain their printed geometry. For this reason, we focused on 2.5-5% of GO within GelMA. In particular, 2.5% GO displayed a

significantly higher angiogenic potential in comparison to 5% GO for the total branching point parameter, suggesting that lower concentration of GO may trigger higher vascular reactions. However, 2.5% GO scaffolds showed a similar and comparable vascular response to GelMA alone, indicating that the addition of lower concentration of GO makes no positive differences in terms of angiogenic potential.

These preliminary results suggest that GelMA has an angiogenic potential that could be exploited for BTE applications in the future. However, for the purposes of this study, GelMA does not represent the most suitable hydrogel for printing Pal-OS®, since it does not allow the powder to display its properties. Overall, all the bioinks tested were not able to reproduce the Pal-OS® powder angiogenic potential in the scaffold form. Taken together these results suggest that further research is required to find other bioinks to print the Pal-OS® powder for most effective BTE applications.

2.5 *Conclusion*

In this study, the Pal-OS® powder was characterized and successfully printed through a micro-extrusion bioprinting technique by blending different hydrogels together. Once defined that the powder particulate had compatible dimensions with the nozzle diameter and that the Pal-OS® maintained the SOs properties *in vivo,* a grid-like porous geometry was chosen to print the scaffolds with high precision and resolution. The CAM assay was the common thread that provided an advantageous *in ovo* platform to test the angiogenic potential of all the scaffolds.

First, Pal-OS® was printed at different concentrations blended within GelMA: 50 and 70% of powder resulted to be the most promising bioinks for technical and biological reasons. However, since GelMA displayed a higher angiogenic potential than the scaffolds with Pal-OS®, HA and GO were added to the bioinks to improve their angiogenic performance. The addition of HA undoubtedly

decreased the performance of all the scaffolds, whereas the presence of 2.5% GO displayed a similar angiogenic reaction to GelMA alone.

In conclusion, even if GelMA displayed a significant angiogenic potential *in ovo*, all the tested hydrogels did not improve the Pal-OS® powder properties. For BTE purposes, angiogenesis is preliminary to all bone regenerative processes, so it is necessary to study further solutions to support the powder pro-angiogenic potential. In the future, we will focus on the search of other bioinks to print the Pal-OS® powder with a porous 3D geometry to allow the optimal expression of its peculiar features.

3. CHAPTER III: BIOACTIVE GLASSES

3.1 *Introduction*

Among synthetic materials, bioactive glasses (BGs) have emerged as a promising class for bone tissue regeneration. The primary advantage of BGs is their ability to bond with bone, promoting growth and regeneration. In particular, since its discovery in the 1960s, the 45S5 Bioglass® had stood for its osteoinductivity and osteoconductivity properties, and the ability of stimulating osteoprogenitor cells to proliferate and differentiate at genetic level (Jones, 2013). However, the main challenge of BGs is their tendency to crystallize at high temperatures, which affects their bioactivity, limiting their use in BTE applications (Lefebvre et al., 2007). In fact, crystallization can be hazardous because biological tissues tend to degrade the residual glassy phase of the resulting sintered BGs, causing instability in the implant. Additionally, partially crystallized samples slow the ionic release of BGs, that significantly affects their regenerative potential, which is fundamental for osteogenesis and angiogenesis in bone (Galusková et al., 2021). To overcome this limitation, researchers have focused on modifying the ion composition of BGs with the so-called "therapeutic ions" to improve also their biological response (Zhu et al., 2021). For instance, silicon is known for inducing EC migration, differentiation and neo-blood vessels sprouting, whereas phosphorus has demonstrated to induce VEGF-A, HUVEC migration and tube formation. Calcium and magnesium, instead, can stimulate EC proliferation and migration: the first increasing different growth factors such as VEGF-A and PDGF, the second enhancing the mitogenic response to angiogenic factors (Kargozar et al., 2018). One of the promising alternatives to the original 45S5 composition is the recently developed bioactive glass BGMS10, which presents the addition of strontium and magnesium ions (Bellucci and Cannillo, 2018). This BG has an extraordinarily high crystallization temperature of 932°C, excellent biocompatibility and bioactivity, demonstrated through 3D *in vitro* testing with human MSCs (Bellucci et al., 2019b).

Bio_MS is another innovative composition containing strontium and magnesium, which has also displayed very promising features. This BG exhibited better biological performance than 45S5, with a very high crystallization temperature and a large processing window that allowed the production of completely amorphous products, despite the thermal treatment. The biological responsiveness of Bio_MS was assessed using simulated body fluid (SBF) and BM-MSCs, that successfully colonized the material and differentiated into bone lineage cells, demonstrating the excellent regenerative potential of this novel BG (Bellucci et al., 2020).

In this study, for the first time, BGMS10 and Bio_MS were tested along with the gold standard 45S5 to evaluate and compare their angiogenic potential both *in vitro* and *in ovo*. In order to investigate which 3D structure could better trigger and support angiogenesis for BTE applications, the three BGs were compared in the form of granules and scaffolds.

3.2 *Materials and methods*

3.2.1 Preparation of BG granules

The composition of the bioactive glasses studied are provided in Table III.1. These BG granules were manufactured using a traditional melting technique, reported by Bellucci *et al* (Bellucci et al., 2019a). Briefly, the powdered reagents (all Carlo Erba Reagenti, Rodano-Milano, Italy) were meticulously mixed for 6 h and then placed in a platinum crucible. The temperature was gradually increased by 10°C per minute until it reached 1450°C. Additionally, an isothermal step at 1100°C was performed for one hour to facilitate the decarbonation of the reagents. Following this, the molten glass was poured into RT water, resulting in a frit, which was subsequently dried for 24 h at 110°C. The frits were further processed by grinding and sieving, producing granules (particle size ranging from 250

to 500 μm) for subsequent biological testing, as well as finer powders (grain size < 63 μm) for scaffold preparation.

Oxides Composition [mol%]			
	45S5	**BGMS10**	**Bio_MS**
SiO_2	46.1	47.2	46.1
P_2O_5	2.6	2.6	2.6
Na_2O	24.4	2.3	5
CaO	26.9	25.6	31.3
K_2O	0	2.3	0
MgO	0	10	5
SrO	0	10	10

Table III.1. Composition in oxides mol% of the produced glasses.

3.2.2 Preparation and characterization of BG scaffolds

The scaffolds were produced using the traditional replica technique, which involves impregnating a polymer sponge with a glass slurry and subjecting the entire structure to heat treatment to evaporate the polymer phase and sinter the glass phase. The slurry was prepared by dispersing glass powders in distilled water, with the prior dissolution of polyvinyl alcohol (PVA). PVA serves a dual purpose: optimizing the slurry's viscosity and, acting as a binder, facilitating the adhesion of glass particles to the sponge. The weight ratio of the slurry components was as follows: 64% water, 6% PVA, and 30% glass, according to the protocol proposed by Chiara Vitale-Brovarone *et al*. (Vitale-Brovarone et al., 2009). The sponge, shaped in a cubic form, was immersed in the slurry for 10 seconds, then extracted and compressed to remove excess slurry, before being immersed again. This procedure was repeated to ensure a sufficient level of impregnation for each sponge. Subsequently, the glass-impregnated sponges were left to dry for 24 h at RT. Finally, they underwent heat treatment by gradually raising the temperature to the sintering temperature for each type of glass: 1050°C for 45S5, 730°C for Bio_MS, and 740°C for BGMS10. The temperature increase followed a gradient of 3°C per minute

until reaching 500°C, and then increased by 5°C per minute until reaching the sintering temperature, where the samples were treated for 3 h. At the end of the heat treatment, the samples were removed from the furnace and allowed to cool to RT.

To examine the potential crystallization of the glasses during the thermal treatment, the scaffolds were ground into powders. The obtained powders were then analysed using X-ray diffraction (XRD) to evaluate whether their amorphous nature had been preserved or not. The samples were examined using a PANalytical X'pert PRO diffractometer utilizing Cu Kα radiation. The glass powders were scanned between 2θ=10° and 2θ=70° with a step size of 2θ=0.02°.

The microstructure of the scaffolds was examined by SEM at 20 kV, employing the ESEM Quanta 2000 model (FEI Co., Eindhoven, Netherlands). To enhance conductivity, samples were sputter-coated with gold before observation and the analysis was conducted under high-vacuum conditions.

3.2.3 3D cell cultures

MAEC were cultured under standard conditions in DMEM (Gibco, Thermo Fisher Scientific, Waltham, MA, USA) added with 10% FBS, 2 mM L-glutamine, and 100 $U \cdot mL^{-1}$ penicillin, and 100 $U \cdot mL^{-1}$ streptomycin (all Sigma Aldrich, Darmstadt, Germany) in a humidified incubator set at 37°C with 5% CO_2. Before the seeding, the BGs granules and scaffolds were sterilized under UV light O/N. Then, MAEC were seeded onto the BGs at 2×10^4 cells cm^{-2} in a 24-well plate and cultured until 72 h. At different time points (24, 48 and 72 h), cell viability was determined by the resazurin reduction assay as follows: the resazurin reagent was added directly to the culture medium with 10 vol % medium contained in each sample and incubated for 4 h at 37 °C with 5% CO_2. Subsequently, aliquots from each sample were transferred to a 96-multiwell plate for fluorescence measurements at λ_{exc} 560 nm and λ_{em} 590 nm at Thermo Scientific Varioskan Flash Multimode Reader (Thermo Fisher Scientific, Waltham, MA, USA). A negative control of only medium without cells was included to

determine the background signal along with a positive control of 100% reduced resazurin reagent without cells. The analysis was conducted in triplicate with three independent experiments.

3.2.4 Morphological analyses

After the 3D cell culture, the specimens were fixed with 4% paraformaldehyde/PBS (Sigma Aldrich, Darmstadt, Germany) and washed in 1× PBS. Then they were permeabilized with 0.001 wt % Triton-X 100. The cells were labelled with tetramethylrhodamine (TRITC)-conjugated phalloidin (FAK100, Merck Millipore, Darmstadt, Germany) for 1 h, followed by rinsing with 1×PBS. Actin staining was critical to map the local orientation of actin filaments within cells. Nuclear counterstaining was performed by incubation with DAPI (FAK100, Merck Millipore, Darmstadt, Germany) for 3 min, followed by rinsing with 1×PBS. Samples were examined using a Nikon Eclipse 80i microscope equipped for fluorescence analysis (Nikon Instruments Europe BV, Amstelveen, The Netherlands). For the SEM analysis, the specimens were treated as follows: 2.5% glutaraldehyde/PBS was added at 4°C for 1 h; then, each sample was rinsed three times in 1×PBS for 5 min before being incubated for 1 h with 1% osmium tetra-oxide (OsO_4). The BGs were rinsed 3 times with distilled water 10 min each time. A sequential dehydration in 50%, 75%, 95% and 99% ethanol was performed, then, the specimens were air-dried, transferred over stubs and coated with a 10 nm thick gold layer by means of the Emitech K550 sputter coater (Quorum Technologies, South Stour Avenue, Kent, UK). BGs colonization was observed in high vacuum conditions at the ESEM Quanta 200 SEM (Fei Company, Hillsboro, OR, USA).

3.2.5 CAM assay and angiogenic response evaluation

Fertilized Isa Brown chicken eggs (Azienda Agricola Cellini Andrea, Forlì, Italy) were placed into the Mercurius MG244 incubator (FIEM, Como, Italy) at 37.8°C in constant humidity conditions. The

CAM assay was performed as previously described (Chapter I, Paragraph 1.2.6). The angiogenic response was performed as reported in Chapter II, Paragraph 2.2.4.

3.2.6 Histological analysis

Both control CAMs and the ones that received the BGs were fixed in 4% paraformaldehyde/PBS (Sigma Aldrich, Darmstadt, Germany), dehydrated in graded ethanol, and embedded in methyl methacrylate (MMA) resin (Sigma Aldrich, Milan, Italy). The specimens were cut in serial sections of 200 µm in thickness with a Leica SP1600 diamond saw microtome cutting system (Leica SpA, Milan, Italy) under water irrigation. The sections were thinned with fine grain emery papers and polished with alumina. Then, samples were stained with a toluidine blue alcoholic solution for 2 min at 60°C and rinsed with tap water. Images were acquired at 20× and 40× magnification under a light microscope (Eclipse Ni-E, Nikon Instruments Europe BV, Amstelveen, Netherlands).

3.2.7 Quantitative Real Time-Polymerase Chain Reaction (qRT-PCR)

For molecular analysis, treated and control CAM samples were harvested at different time points (8 and 48 h) to investigate the angiogenic reaction triggered by the BGs. To reduce the high variability intrinsic to this biological complex system, three CAM tissue samples were pooled together for each experimental point and three independent experiments were carried out. The RNA extraction was performed using TRIzol™ Reagent (Invitrogen, Thermo Fisher Scientific, Waltham, MA, USA), following the manufacturer's instructions. High-Capacity cDNA Reverse Transcription Kit (Thermo Fisher Scientific, Waltham, MA, USA) was employed to obtain the complementary DNA (cDNA). Quantitative gene expression was assessed employing the TaqMan® Gene Expression Master Mix, using the QuantStudio1 Real-Time PCR (Thermo Fisher Scientific, Waltham, MA, USA). The following chicken TaqMan probes were employed (all from Thermo Fisher Scientific, Waltham, MA, USA): VEGF-A (#Gg03362204_m1), VEGFR2 (#Gg03346172_m1), CDH5 (#Gg03364043_m1),

PECAM1 (#Gg03331692_m1), CD34 (#Gg07164057_g1). Glyceraldehyde 3-phosphate dehydrogenase (GAPDH) (#Gg03346982_m1) was used as internal control. Relative quantification was performed using the ΔΔCt method, and results were plotted as $2^{-\Delta\Delta Ct}$.

3.2.8 Statistical analysis

Data from the angiogenic response evaluation and molecular analysis are expressed as mean ± SD. At least three different experiments were performed for each analysis. Differences between the experimental conditions were evaluated by one-way ANOVA with Bonferroni's correction for multiple comparisons. The type of analysis and significant p-values are indicated in figure legends. Statistical analysis and relative graphs were elaborated with GraphPad Prism 6 Software (version 6.01, San Diego, USA).

3.3 *Results*

3.3.1 BGMS10 and Bio_MS scaffolds displayed a structural improvement compared to 45S5

The XRD spectra obtained from the powdered-reduced scaffolds are depicted in Figure III.1. The 45S5 scaffold is extensively crystallized, in contrast to BGMS10 and Bio_MS. In the case of 45S5, the peaks observed in the spectrum correspond to the combeite-type phase $Na_2CaSi_2O_6$. Instead, both the spectra of BGMS10 and Bio_MS showed that the two glasses can be consolidated at lower temperatures compared to 45S5.

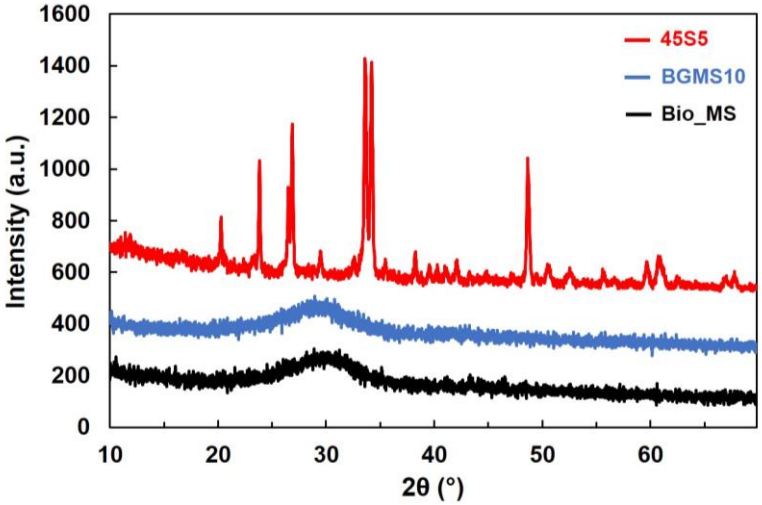

Figure III.1. XRD spectra analyses of the 45S5, BGMS10 and Bio_MS ground scaffolds.

Then, the microstructure of the scaffolds was examined using SEM. In the low-magnification panel (a-c) in Figure III.2, it is evident that all samples exhibited large pores that can enable cell infiltration. Upon closer inspection at higher magnification (d-f), both BGMS10 and Bio_MS have achieved a higher degree of powder densification, with BGMS10 showing particularly notable improvement. Conversely, in the case of 45S5, where the sintering process is impeded by concurrent glass crystallization, a pervasive presence of residual microporosity can be observed with identifiable remnants of the original glass particles; in addition, the surface appearance is considerably less smooth compared to BGMS10.

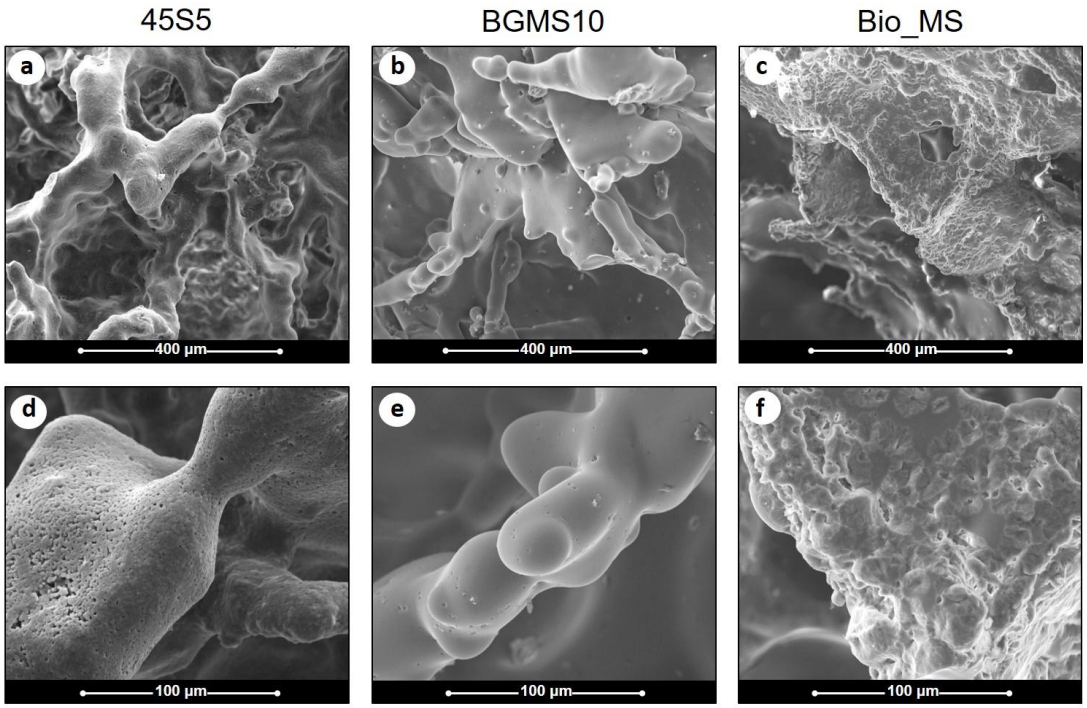

Figure III.2. SEM analysis of the BG scaffolds (45S5, BGMS10, Bio_MS). Images in panel a-b-c were acquired at 400X magnification (scale bar 400 µm), in d-e-f at 1600X magnification (scale bar 100 µm).

3.3.2 The BG granules allowed a higher cell viability compared to the scaffolds

MAEC were seeded over both granules and scaffolds, and left to grow over the BGs for 24, 48 and 72 h. The fluorescence data, reported in Figure III.3, showed that the BG granules allowed a higher cell viability compared to the scaffolds for the three time points analysed. In particular, at 72 h of culture, all the BG granules displayed significant higher cell viability compared to 45S5 scaffolds ($p \leq 0.05$). If the three BG granules showed a comparable trend, with a slightly growth over time, the two novel BG scaffolds seemed to surpass the gold standard viability after 48 and 72 h of culture. In addition, after 72 h, BGMS10 scaffolds displayed the highest cell viability.

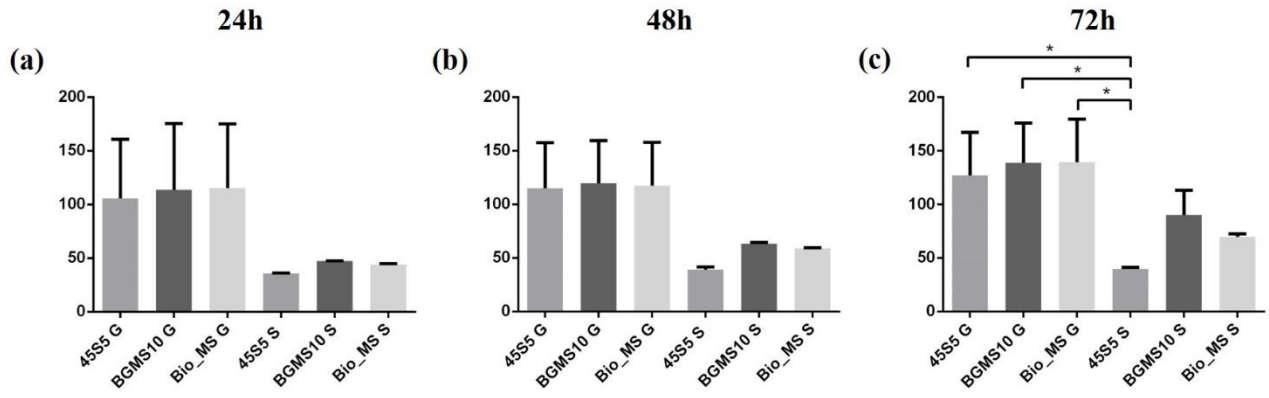

Figure III.3. Cell viability of the three BGs granules (G) and scaffolds (S) after 24, 48 and 72 h. a) Comparison between the granules and the scaffolds of MAEC viability, expressed as fluorescence (Y axis), after 24 h (a), 48 h (b) and 72 h (c) and relative statistical analysis (*$p \leq 0.05$).

3.3.3 The two novel BGs allowed a better colonization and cell morphology than the gold standard

The morphological analyses were conducted on the same specimens exploited to assess cell viability. Immunofluorescence analysis showed that cells were able to colonize all the BG granules, but to different extents. In particular, as shown in the images at lower magnification, reported in Figure III.4a, MAEC homogeneously colonized BGMS10 and Bio_MS in all their three-dimensionality, whereas in 45S5 granules only a few sparsely scattered cells were found. Moreover, the images at higher magnification indicated that MAEC were able to attach to the two novel granules, showing their peculiar dendritic morphology, whereas they displayed a round morphology over the gold standard. This data was confirmed also by SEM analysis. From the images reported in Figure III.4b, it is possible to visualize MAEC also forming different cell-to-cell interactions in BGMS10 and Bio_MS granules. Instead, in 45S5 granules a round morphology with fewer cell interactions was observed. In addition, only for the gold standard, many debris were spotted over the granules and near the cells.

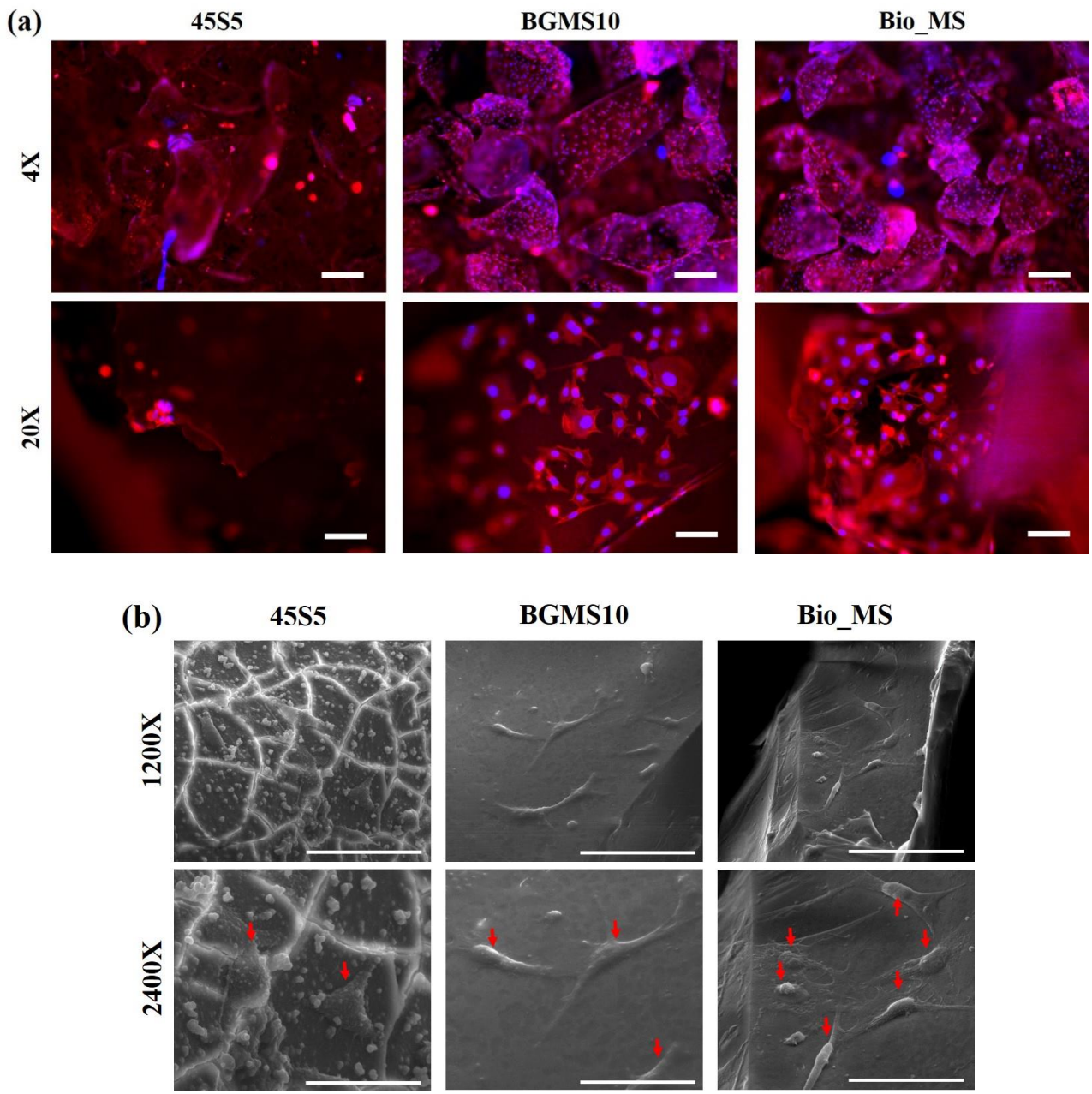

Figure III.4. Micrographs show MAEC colonizing the three BG granules. a) Immunofluorescence analysis: cell nuclei in blue (DAPI), cytoplasms in red (actin); images acquired at 4X (scale bar 250 µm) and 20X magnification (scale bar 50 µm). b) Cell morphology of the same specimens evaluated at SEM: the red arrows indicate the cells; magnification 1200X (scale bar 100 µm) and 2400X (scale bar 50 µm).

Similarly, immunofluorescence analysis of the BG scaffolds showed that MAEC homogeneously colonized BGMS10 and Bio_MS in all their three-dimensionality, while they did not display the same

behaviour over 45S5 scaffold. The images reported in Figure III.5a clearly demonstrated that only a few sparsely scattered cells were found over 45S5 scaffold. Despite the difficulty of colonizing high and jagged 3D structures, MAEC displayed their dendritic morphology, visibly attached to both BGMS10 and Bio_MS scaffolds; instead, they seemed to have a round morphology over the gold standard. SEM analysis confirmed that the cells became attached to the two novel BG scaffolds with spread cytoplasms and some cell-to-cell interactions, as it could be seen from the images reported in Figure III.5b. Moreover, it is possible to visualize MAEC displaying a round morphology without any cell-to-cell connection over 45S5 scaffolds. In addition, the gold standard scaffolds showed a peculiar jagged shape, which is completely different from the other two BGs.

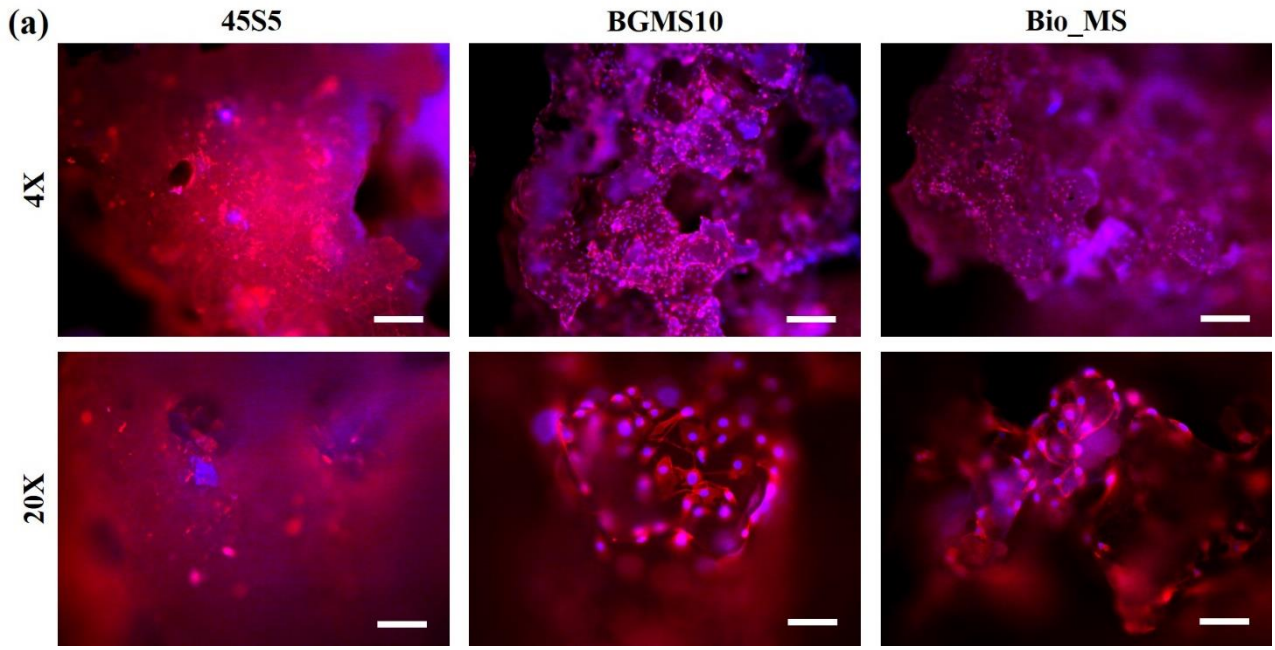

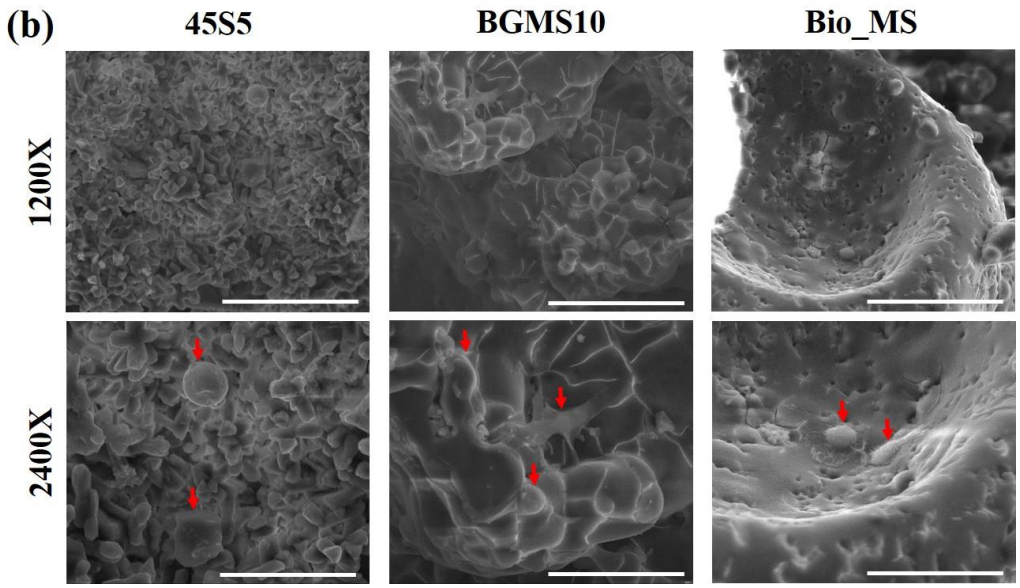

Figure III.5. Micrographs show MAEC colonizing the three BG scaffolds. a) Immunofluorescence analysis: cell nuclei in blue (DAPI), cytoplasms in red (actin); images acquired at 4X (scale bar 250 µm) and 20X magnification (scale bar 50 µm). b) Cell morphology of the same specimens evaluated at SEM: the red arrows indicate the cells; magnification 1200X (scale bar 100 µm) and 2400X (scale bar 50 µm).

3.3.4 The BG granules triggered a significant higher vascular reaction *in ovo* compared to the scaffolds

The vascular reaction triggered by all the bioactive glasses (45S5, BGMS10, Bio_MS), both in granules and in scaffold form, displayed irregular capillaries of neo-formation sprouting radially from their core, like spokes in a wheel. As reported in Figure III.6a, many of these vessels branched dichotomously, a typical index of a strong angiogenic response. Moreover, we observed an evident angiogenic potential of the BGs compared to the control CAMs, characterized by linear and regular vessels forming the natural background of the membrane.

The angiogenic potential data revealed that, for the three parameters analysed (vessel density, total vessel network length, total branching point), all the BGs, both in granular and in scaffold form, were significantly more pro-angiogenic than the control CAMs (Figure III.6b). In addition, all the granules also displayed significantly higher angiogenic responses compared to their relative counterparts in

scaffold form, although for BGMS10 the differences were not statistically significant. Among the granules, none showed any significant difference compared to the others in terms of angiogenic potential. Even among the scaffolds, for the total vessel network length and the total branching points the angiogenic potential did not show any significant difference among the three groups; however, only for the vessel density BGMS10 resulted to be significantly more pro-angiogenic than the gold standard 45S5.

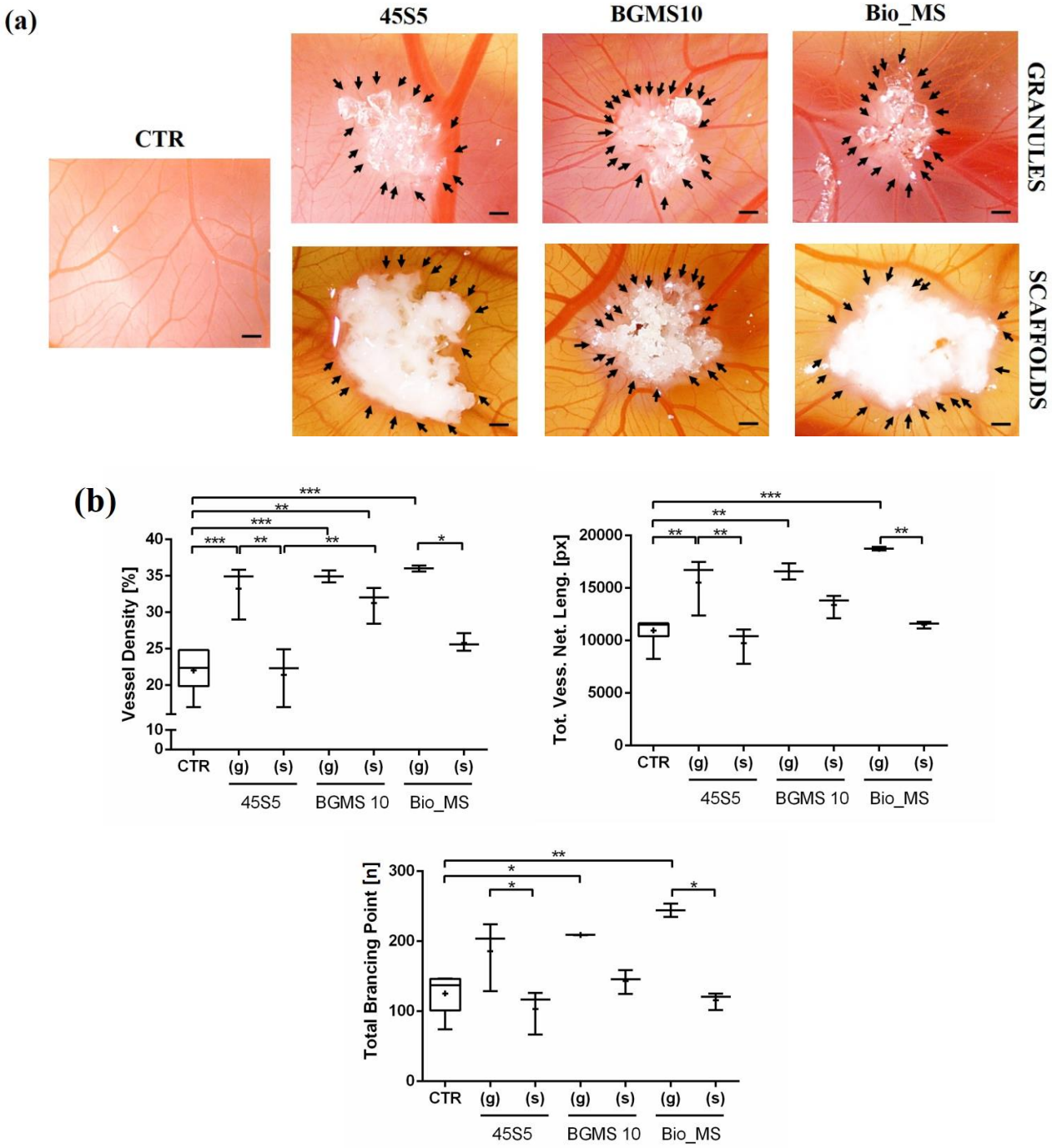

Figure III.6. Angiogenic evaluation of the three BGs (45S5, BGMS10, Bio_MS) arranged as granules and scaffolds. a) CAM assay of the three BGs compared to the control (CTR, untreated CAM): the black arrows indicate the vessels of neo-formation sprouting radially from the bioactive glasses; magnification 1X, scale bar 250 μm. b) Angiogenic reaction analysis and relative statistical analysis. The parameters analysed were the vessel density, the total vessel network length, the total branching point; the BG granules (g) were compared to their relative scaffolds (s) and the control CAMs (CTR) (*$p \leq 0.05$; **$p \leq 0.01$; ***$p \leq 0.001$).

3.3.5 The histological analysis confirmed the high biocompatibility of the BG granules

The histological analysis of the control CAMs showed the typical structure with two superficial monolayered epithelia (the upper called chorionic, the lower allantois) comprising an intermediate mesenchyme with wide blood vessels (CTR in Figures III.7 and III.8). The CAMs grafted with the granules displayed a remarkable proliferation of CAM tissues around the BGs compared to the controls, without visible inflammatory reactions (Figure III.7). In particular, the toluidine blue staining revealed the presence of abundant connective tissue, rich in proteoglycans (as the metachromasia suggests) and vessels, mostly of small sizes, near the BGs. In addition, a neo-formed multi-layered epithelium that encompasses the granules was also observed in the surrounding areas. Also, the histological evaluation did not highlight any difference among the three BGs, confirming the results obtained with our previous analyses.

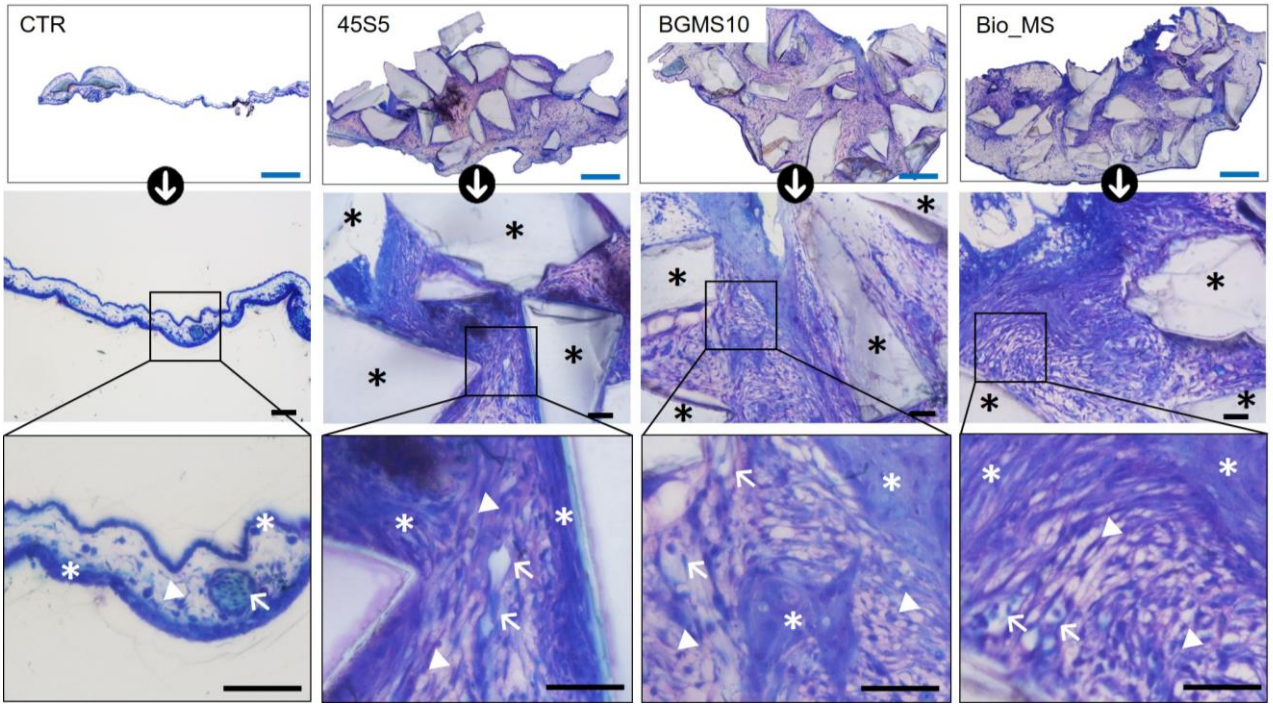

Figure III.7. Histological sections stained with toluidine blue of the control CAMs (CTR) and the BG granules (black asterisks) grafted onto the CAMs: epithelial tissue in blue (white asterisks), connective tissue (arrow heads) with proteoglycans in purple, vessels (arrows); blue scale bar 500 µm, black scale bar 50 µm.

The CAMs grafted with the scaffolds showed a considerable proliferation compared to the controls, without any observable difference among the three BGs, evidencing a proteoglycan-rich connective tissue with vessels, mostly of large dimensions, and a multi-layered epithelium of neo-formation; no visible inflammatory reactions were detectable (Figure III.8). In comparison to the granules, the scaffolds were not surrounded completely by the CAM tissues, which were unable to penetrate all the internal porosities of the BGs (red asterisks in Figure III.8).

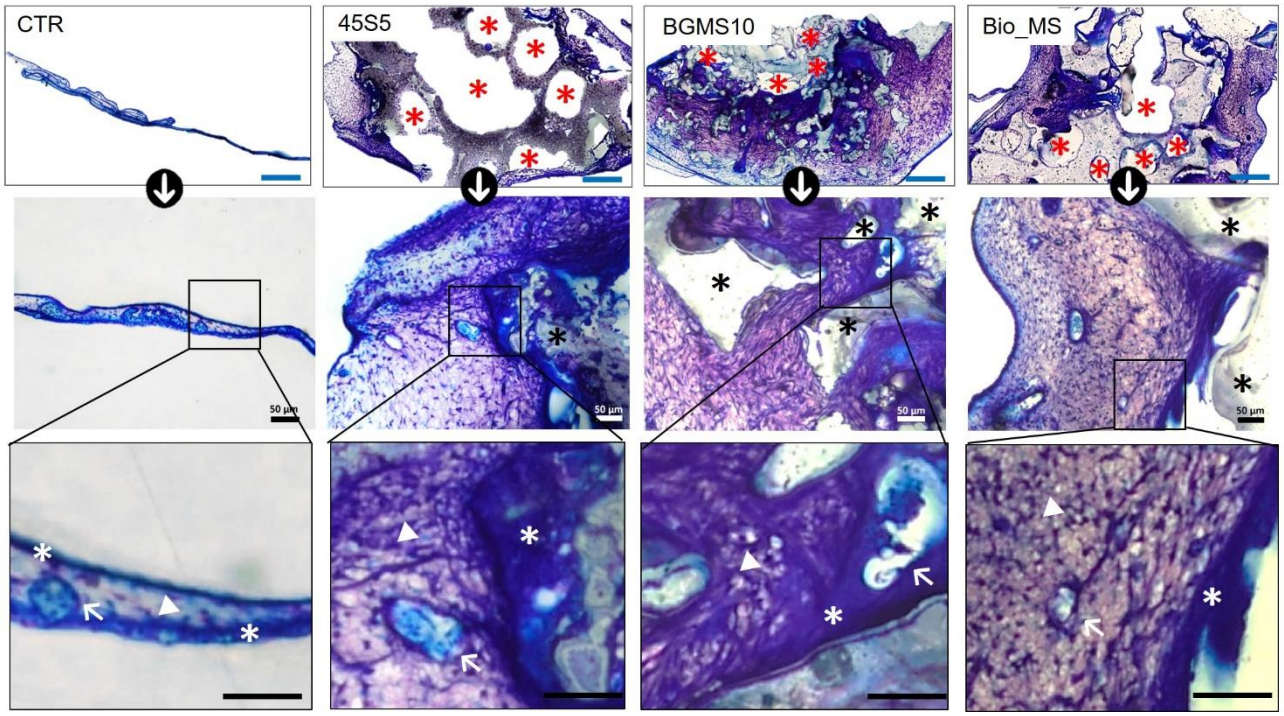

Figure III.8. Histological sections stained with toluidine blue of the control CAMs (CTR) and the BG scaffolds (black asterisks) grafted onto the CAMs: epithelial tissue in blue (white asterisks), connective tissue (arrow heads) with proteoglycans in purple, vessels (arrows); blue scale bar 500 µm, black scale bar 50 µm. In the first row the red asterisks indicate the areas where the CAM tissues were unable to penetrate the internal porosities of the scaffolds.

3.3.6 The BG granules induced a significant upregulation of the expression of different genes related to angiogenesis

Since the BG granules had exhibited a better angiogenic response compared to their scaffold counterparts, gene expression analyses were conducted on the former to deepen their biological activity at molecular level. To this aim, a possible modulatory effect was evaluated by analysing the expression of genes correlated to angiogenesis (VEGF-A, VEGFR2, CDH5, PECAM1 and CD34). We found no significant modulation after 8 h from the grafting, compared to control samples, which underwent the same treatment of other CAMs without receiving the BG granules. Interestingly, an increase in gene expression of these pro-angiogenic markers was observed after 48 h from the grafting

with BG granules. As reported in Figure III.9, CDH5 expression was significantly upregulated by all the BGs compared to the 8 h. Moreover, the results showed that the expression of CDH5 was significantly higher in Bio_MS in comparison to the gold standard 45S5 ($p \leq 0,05$) and to BGMS10 ($p \leq 0,01$).

Furthermore, Bio_MS granules caused a greater increase in gene expression levels of VEGF-A and its receptor VEGFR2. BGMS10 granules, instead, showed a significant increase in gene expression only for VEGF-A. However, the upregulation was significant only for the two novel BGs after 48 h compared to the 8 h.

PECAM1 gene expression was also evaluated due to its importance for endothelial cells. The results showed no significant differences between the three BG granules analysed. Finally, similar to VEGF-A and VEGFR2, CD34 gene expression was increased by 45S5 and Bio_MS after 48 h compared to the 8 h from the grafting (Figure III.9).

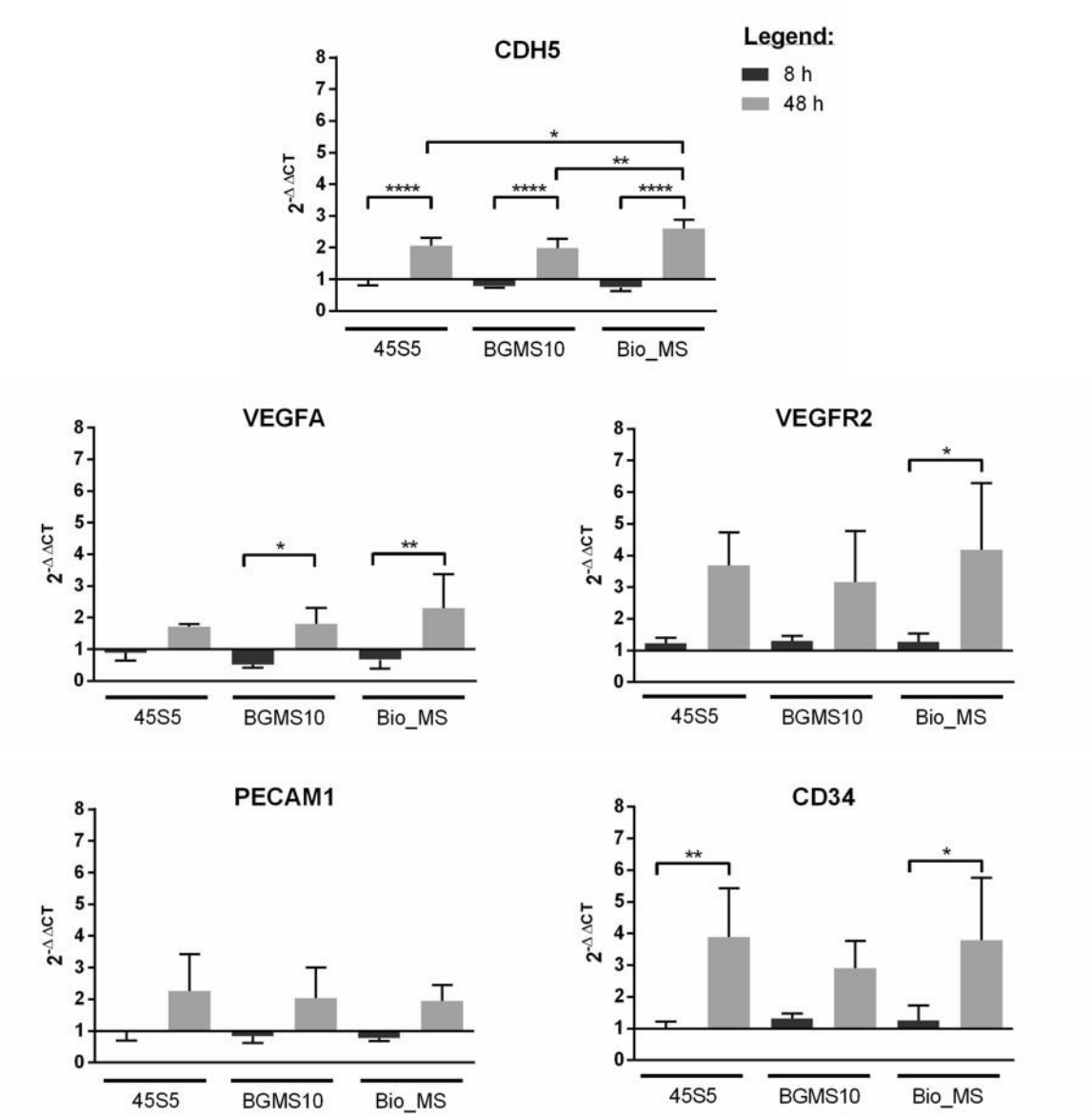

Figure III.9. Gene expression profile of VEGF-A, VEGFR2, CDH5, PECAM1 and CD34 in BG granules grafted onto the CAM after 8 and 48 h. The plot shows the $2^{-\Delta\Delta Ct}$ values (Y axis) and SD. The data were normalized on the control CAMs (black line y=1) and the endogenous gene GAPDH (*$p \leq 0.05$, **$p \leq 0.01$, ****$p \leq 0.0001$).

3.4 *Discussion*

This study explored the angiogenic potential of two novel bioactive glasses, BGMS10 and Bio_MS through morphological and molecular analyses. The two BGs were tested both in the form of granules and scaffolds, and compared to the gold standard 45S5.

Preliminary to biological analysis, the objective of XRD analysis was to identify potential crystallization of the BGs, resulting from the necessary thermal treatment for sintering the scaffolds. Even if the crystallization of BGs does not compromise their reactivity in a physiological environment, it has been reported that it does significantly slow down the process, as well as the release of ions from the glass surface (Mecca et al., 2023). In fact, the biological effects of BGs, such their regenerative potential in bone injuries, are attributed to the release of ions (Hoppe et al., 2011). Moreover, partially crystallized samples are more prone to fractures or instability upon *in vivo* implantation, as the residual amorphous phase tends to dissolve more rapidly in a physiological environment (Galusková et al., 2021). BGMS10 and Bio_MS were specifically designed to have a high crystallization temperature, allowing them to be sintered while retaining their amorphous nature and biological potential. In fact, XRD analysis demonstrated that the two novel BG scaffolds can be consolidated at lower temperatures compared to 45S5. Conversely, in the case of 45S5, an alternative combeite phase $Na_2Ca_2Si_3O_9$ has also been reported (Clupper and Hench, 2003), but the ambiguity in interpreting the spectrum arises from the structural similarity between these two crystalline phases. Other authors have also addressed the formation of a complex solid solution involving the two mentioned crystalline phases (Fujikura et al., 2012). SEM analysis also confirmed the presence of residual microporosity in the 45S5 scaffolds with identifiable remnants of the original glass particles. The two novel BGs, instead, showed a higher degree of powder densification: BGMS10, in particular, reached a visible superficial smoothness, which is a desirable feature for biological purposes.

To assess the biocompatibility of the scaffolds and compare their performance to the granules, the viability of endothelial cells seeded over the BGs was evaluated. The results clearly indicated that the

granules allowed a higher cell viability compared to the scaffolds, which was significant for all the BGs in comparison to the gold standard scaffold after 72 h from cell seeding, but evident already after 24 h. Taken together, these data suggest that the cells seeded onto the scaffolds may require more time to establish cell-to-cell interactions and colonize their 3D structure. The results also highlighted that, among the BG scaffolds, BGMS10 displayed the highest cell viability after 48 and 72 h of culture, suggesting that this novel composition may have improved the gold standard biological properties.

Morphological analyses, in particular the immunofluorescence, confirmed that both the granules and the scaffolds allowed the colonization by endothelial cells. However, for both granules and scaffolds, BGMS10 and Bio_MS displayed a homogeneously colonization in all their three-dimensionality, while 45S5 showed only a few sparsely scattered cells with a round morphology. This data suggests that the two novel formulations allowed a better cell adhesion to the BGs. Accordingly, SEM images clearly indicated a difference among the novel BGs and the gold standard in terms of cell morphology: in fact, MAEC displayed their peculiar dendritic morphology, with spread cytoplasm and different cell-to-cell interactions, only over BGMS10 and Bio_MS. A possible explanation is that, due to the ionic release, the surface of 45S5 has converted into hydrated silica, which peels off. The calcium phosphate precipitates on the hydrated silica gel and the cells made more effort to attach than on a more regular surface like the other BGs.

The gold standard scaffold, instead, displayed a jagged shape, which presumably did not promote cell adhesion. In fact, BGMS10 and Bio_MS scaffold surfaces appeared smoother than 45S5, as previously described. This data is also supported by SEM images that highlight MAEC with a round morphology without any cell-to-cell connection over 45S5 scaffolds, suggesting that the sintering process of the scaffold may have altered the biological properties of the gold standard.

The CAM assay was performed to assess the angiogenic potential of the BG granules and scaffolds, showing a significant higher vascular reaction compared to the control CAMs. Interestingly, 45S5

and Bio_MS granules were significantly more angiogenic than their relative scaffolds, while BGMS10 granules showed a higher angiogenic potential compared to the relative scaffolds, without reaching significance. These data suggest that, given the same material, BG granules display a better angiogenic potential. The influence of the geometry onto CAM has already been demonstrated in other studies: in fact, surface smoothness and high thickness are not positive features for *in ovo* validations. In fact, the CAM tissue cannot easily incorporate scaffolds mainly developed in height (Valdes et al., 2002). In this context, the BG granules significantly displayed a higher angiogenic response compared to their counterparts in scaffold arrangement, eventually due to their 3D conformation. In addition, the CAM assay pointed out that there were no significant differences among the three BG scaffolds in terms of angiogenic potential, except for BGMS10 that displayed a significantly higher vessel density in comparison to 45S5. This may be ascribed to the fully amorphous nature of BGMS10, which could favour the release of the "therapeutic" ions contained in its composition (Kargozar et al., 2018).

The histological analysis showed an abundant connective tissue rich in proteoglycans and a multi-layered epithelium surrounding the BGs compared to control CAMs. This data suggests that all the granules had the ability to trigger a remarkable cell proliferation of the CAM tissues, highlighting the high biocompatibility of the BGs within biological systems. Moreover, these analyses showed a possible osteoinductive conditioning by means of osteochondral differentiation, corroborating what was already seen in literature for the gold standard 45S5 (Hench, 2006), and what it was already demonstrated about BGMS10 and Bio_MS with previous *in vitro* studies (Bellucci et al., 2020, 2019b). From our previous studies, the osteoinductive potential of BG granules was already demonstrated by implanting the three formulations in rabbit femurs. Interestingly, *in vivo* the two novel BG granules granted the formation of a uniform net of bone trabeculae, compared to the less regularly distributed trabeculae separated by large amounts of soft tissue in 45S5 granules (Anesi et al., 2023).

The histological analysis also pointed out the presence of vessels of neo-formation in the proximity and among the BG granules, different from the ones of the CAM background, whose greater dimensions are visible in the control CAMs and in the scaffold samples. In addition, in the BG scaffolds the internal porosities were only partially surrounded by the CAM tissues. Taken together, these results suggest that the geometry of the scaffolds did not allow the colonization of the internal porosities, whereas the smaller dimensions of the granules allowed their incorporation into the CAM tissue and the infiltration of neo-formed vessels (Valdes et al., 2002).

Lastly, to better deepen the results obtained at morphological level, the BG granules were also evaluated through molecular analysis. We decided to focus on the BG granules since they had exhibited better angiogenic potential onto the CAM, compared to their scaffold counterparts. Specifically, VEGF-A and its receptor VEGFR2, which are the most known markers of angiogenesis, playing a key role in vascularization, were evaluated (Gheorghescu and Thompson, 2016). In the CAM context, VEGF-A and VEGFR2 are both expected to be modulated when a pro-angiogenic biomaterial is implanted, since the membrane reacts by forming new blood vessels around the graft (Demcisakova et al., 2022). CDH5, also known as VE-cadherin, is a transmembrane protein associated with adherent junctions and a fundamental molecule for the establishment of functional cell-to-cell connections in endothelial cells forming the vessels (Gheorghescu and Thompson, 2016). On the other hand, PECAM1, *i.e.* CD31, is a membrane glycoprotein, normally found on endothelial cells, which enables the formation of new blood vessels through cell-to-cell adhesions (DeLisser et al., 1997). In our work, CDH5 and PECAM1 were evaluated to analyse the cell-to-cell connections that are fundamental for ECs to assemble into new vessels. Finally, CD34 gene expression was investigated, due to its role as stemness marker in hematopoietic stem and progenitor cells; in the context of vascularization, it is a surface glycoprotein expressed by quiescent endothelial cells at sites of active angiogenesis on the lumen of blood vessels (Siemerink et al., 2012).

The results showed that all genes evaluated (VEGF-A, VEGFR2, CDH5, PECAM1 and CD34) were upregulated, although data did not always reach statistical significance, eventually due to the high experimental settings variability. In fact, even if the CAM model is not considered animal experimentation, its complexity could provide variable outputs (Palumbo et al., 2023).

The results indicate that Bio_MS and BGMS10 granules were able to significantly upregulate both VEGF-A and its receptor VEGFR2, confirming that the two novel BGs triggered a higher angiogenic response than the gold standard after 48 h. This data suggests that the novel BGs may have effectively ameliorated the 45S5 composition in terms of angiogenic potential.

Moreover, Bio_MS significantly triggered CHD5 expression compared to 45S5 and BGMS10, while PECAM1 expression was upregulated after 48 h in all BG granules analysed, but without reaching significance. The data suggest that all the BG granules may enhance cell-to-cell connections in CAM endothelial cells, and that Bio_MS, in particular, could significantly increase CHD5 expression and the establishment of adherent junctions compared to the other BG granules.

Finally, the granules were able to significantly increase the expression of CD34, especially 45S5 and Bio_MS, suggesting that they could maintain the stemness of EPCs, while simultaneously inducing their massive proliferation, as reported by histological analyses.

All in all, these results may suggest that the BG granules were able to induce angiogenic processes through the upregulation of VEGF-A and its receptor VEGFR2, to enhance cell-to-cell connections in endothelial cells likely by means of CDH5, and to maintain the CD34 stemness marker of EPCs.

3.5 *Conclusion*

In the present work, the angiogenic potential of two novel bioactive glasses, BGMS10 and Bio_MS, was tested with different morphological and molecular techniques and compared to the gold standard 45S5. Taken together, the results clearly indicated that the granules displayed better biological

properties compared to their scaffolds counterparts. The two novel formulations, in particular, showed the most promising characteristics, such as a smoother surface, that allowed a better *in vitro* cell colonization, and a higher *in ovo* vascular reaction, that also triggered the expression of genes related to angiogenesis at molecular level.

In conclusion, present and previous results clearly indicate that the novel BG granules, BGMS10 and Bio_MS, could be successfully used in the future for BTE applications. In a clinical perspective, the choice of BG granules will be crucial for repairing a damaged bone, since they were able to induce the highest angiogenic responses *in vitro* and *in ovo*. However, further investigations are required to deepen these findings. For instance, the characterization of the BG ionic release, which is of primary importance in the context of tissue regeneration, could point out additional aspects related to the biological properties of the granules and the molecular mechanisms behind their angiogenic potential.

REFERENCES

- Adair, T.H., Montani, J.-P., 2010. Angiogenesis, Integrated Systems Physiology: from Molecule to Function to Disease. Morgan & Claypool Life Sciences, San Rafael (CA).

- Adams, R.H., Alitalo, K., 2007. Molecular regulation of angiogenesis and lymphangiogenesis. Nat. Rev. Mol. Cell Biol. 8, 464–478. https://doi.org/10.1038/nrm2183

- Anesi, A., Ferretti, M., Salvatori, R., Bellucci, D., Cavani, F., Di Bartolomeo, M., Palumbo, C., Cannillo, V., 2023. In-vivo evaluations of bone regenerative potential of two novel bioactive glasses. J. Biomed. Mater. Res. A 111, 1264–1278. https://doi.org/10.1002/jbm.a.37526

- Ang, S.L., Shaharuddin, B., Chuah, J.-A., Sudesh, K., 2020. Electrospun poly(3-hydroxybutyrate-co-3-hydroxyhexanoate)/silk fibroin film is a promising scaffold for bone tissue engineering. Int. J. Biol. Macromol. 145, 173–188. https://doi.org/10.1016/j.ijbiomac.2019.12.149

- Bellucci, D., Cannillo, V., 2018. A novel bioactive glass containing strontium and magnesium with ultra-high crystallization temperature. Mater. Lett. 213, 67–70. https://doi.org/10.1016/j.matlet.2017.11.020

- Bellucci, D., Chiellini, F., Ciardelli, G., Gazzarri, M., Gentile, P., Sola, A., Cannillo, V., 2012. Processing and characterization of innovative scaffolds for bone tissue engineering. J. Mater. Sci. Mater. Med. 23, 1397–1409. https://doi.org/10.1007/s10856-012-4622-6

- Bellucci, D., Salvatori, R., Anesi, A., Chiarini, L., Cannillo, V., 2019a. SBF assays, direct and indirect cell culture tests to evaluate the biological performance of bioglasses and bioglass-based composites: Three paradigmatic cases. Mater. Sci. Eng. C 96, 757–764. https://doi.org/10.1016/j.msec.2018.12.006

- Bellucci, D., Veronesi, E., Dominici, M., Cannillo, V., 2020. A new bioactive glass with extremely high crystallization temperature and outstanding biological performance. Mater. Sci. Eng. C 110, 110699. https://doi.org/10.1016/j.msec.2020.110699

- Bellucci, D., Veronesi, E., Strusi, V., Petrachi, T., Murgia, A., Mastrolia, I., Dominici, M., Cannillo, V., 2019b. Human Mesenchymal Stem Cell Combined with a New Strontium-Enriched Bioactive Glass: An ex-vivo Model for Bone Regeneration. Materials 12, 3633. https://doi.org/10.3390/ma12213633

- Bonfield, W., 2006. Designing porous scaffolds for tissue engineering. Philos. Trans. R. Soc. Math. Phys. Eng. Sci. 364, 227–232. https://doi.org/10.1098/rsta.2005.1692

- Burri, P.H., Hlushchuk, R., Djonov, V., 2004. Intussusceptive angiogenesis: Its emergence, its characteristics, and its significance. Dev. Dyn. 231, 474–488. https://doi.org/10.1002/dvdy.20184

- Caliari, S.R., Burdick, J.A., 2016. A practical guide to hydrogels for cell culture. Nat. Methods 13, 405–414. https://doi.org/10.1038/nmeth.3839

- Chaturvedi, R.R., Stevens, K.R., Solorzano, R.D., Schwartz, R.E., Eyckmans, J., Baranski, J.D., Stapleton, S.C., Bhatia, S.N., Chen, C.S., 2015. Patterning Vascular Networks *In Vivo* for Tissue Engineering Applications. Tissue Eng. Part C Methods 21, 509–517. https://doi.org/10.1089/ten.tec.2014.0258

- Checchi, M., Bertacchini, J., Cavani, F., Magarò, M.S., Reggiani Bonetti, L., Pugliese, G.R., Tamma, R., Ribatti, D., Maurel, D.B., Palumbo, C., 2020. Scleral ossicles: angiogenic scaffolds, a novel biomaterial for regenerative medicine applications. Biomater. Sci. 8, 413–425. https://doi.org/10.1039/C9BM01234F

- Checchi, M., Bertacchini, J., Grisendi, G., Smargiassi, A., Sola, A., Messori, M., Palumbo, C., 2017. Proposal of a Novel Natural Biomaterial, the Scleral Ossicle, for the Development of Vascularized Bone Tissue In Vitro. Biomedicines 6, 3. https://doi.org/10.3390/biomedicines6010003

- Chen, Y.-C., Lin, R.-Z., Qi, H., Yang, Y., Bae, H., Melero-Martin, J.M., Khademhosseini, A., 2012. Functional Human Vascular Network Generated in Photocrosslinkable Gelatin Methacrylate Hydrogels. Adv. Funct. Mater. 22, 2027–2039. https://doi.org/10.1002/adfm.201101662

- Choi, S., Zhang, Y., MacEwan, M.R., Xia, Y., 2013. Neovascularization in Biodegradable Inverse Opal Scaffolds with Uniform and Precisely Controlled Pore Sizes. Adv. Healthc. Mater. 2, 145–154. https://doi.org/10.1002/adhm.201200106

- Claes, L., Recknagel, S., Ignatius, A., 2012. Fracture healing under healthy and inflammatory conditions. Nat. Rev. Rheumatol. 8, 133–143. https://doi.org/10.1038/nrrheum.2012.1

- Clupper, D.C., Hench, L.L., 2003. Crystallization kinetics of tape cast bioactive glass 45S5. J. Non-Cryst. Solids 318, 43–48. https://doi.org/10.1016/S0022-3093(02)01857-4

- Cyphert, J.M., Trempus, C.S., Garantziotis, S., 2015. Size Matters: Molecular Weight Specificity of Hyaluronan Effects in Cell Biology. Int. J. Cell Biol. 2015, 563818. https://doi.org/10.1155/2015/563818

- DeLisser, H.M., Christofidou-Solomidou, M., Strieter, R.M., Burdick, M.D., Robinson, C.S., Wexler, R.S., Kerr, J.S., Garlanda, C., Merwin, J.R., Madri, J.A., Albelda, S.M., 1997. Involvement of endothelial PECAM-1/CD31 in angiogenesis. Am. J. Pathol.

- Demcisakova, Z., Luptakova, L., Tirpakova, Z., Kvasilova, A., Medvecky, L., De Spiegelaere, W., Petrovova, E., 2022. Evaluation of Angiogenesis in an Acellular Porous Biomaterial Based on Polyhydroxybutyrate and Chitosan Using the Chicken Ex Ovo Chorioallantoic Membrane Model. Cancers 14, 4194. https://doi.org/10.3390/cancers14174194

- Edmondson, R., Broglie, J.J., Adcock, A.F., Yang, L., 2014. Three-Dimensional Cell Culture Systems and Their Applications in Drug Discovery and Cell-Based Biosensors. ASSAY Drug Dev. Technol. 12, 207–218. https://doi.org/10.1089/adt.2014.573

- Eelen, G., Cruys, B., Welti, J., De Bock, K., Carmeliet, P., 2013. Control of vessel sprouting by genetic and metabolic determinants. Trends Endocrinol. Metab. 24, 589–596. https://doi.org/10.1016/j.tem.2013.08.006

- European parliament and Council, 2010. http://data.europa.eu/eli/dir/2010/63/oj.

- Fernandez de Grado, G., Keller, L., Idoux-Gillet, Y., Wagner, Q., Musset, A.-M., Benkirane-Jessel, N., Bornert, F., Offner, D., 2018. Bone substitutes: a review of their characteristics, clinical use, and perspectives for large bone defects management. J. Tissue Eng. 9. https://doi.org/10.1177/2041731418776819

- Ferretti, M., Palumbo, C., 2021. Static Osteogenesis versus Dynamic Osteogenesis: A Comparison between Two Different Types of Bone Formation. Appl. Sci. 11, 2025. https://doi.org/10.3390/app11052025

- Franz-Odendaal, T.A., Hall, B.K., 2006. Skeletal elements within teleost eyes and a discussion of their homology. J. Morphol. 267, 1326–1337. https://doi.org/10.1002/jmor.10479

- Fuchs, S., Hofmann, A., Kirkpatrick, C.J., 2007. Microvessel-Like Structures from Outgrowth Endothelial Cells from Human Peripheral Blood in 2-Dimensional and 3-Dimensional Co-Cultures with Osteoblastic Lineage Cells. Tissue Eng. 13, 2577–2588. https://doi.org/10.1089/ten.2007.0022

- Fujikura, K., Karpukhina, N., Kasuga, T., Brauer, D.S., Hill, R.G., Law, R.V., 2012. Influence of strontium substitution on structure and crystallisation of Bioglass® 45S5. J. Mater. Chem. 22, 7395. https://doi.org/10.1039/c2jm14674f

- Galusková, D., Kaňková, H., Švančárková, A., Galusek, D., 2021. Early-Stage Dissolution Kinetics of Silicate-Based Bioactive Glass under Dynamic Conditions: Critical Evaluation. Materials 14, 3384. https://doi.org/10.3390/ma14123384

- Gheorghescu, A., Thompson, J., 2016. Delayed vasculogenesis and impaired angiogenesis due to altered Ang-2 and VE-cadherin levels in the chick embryo model following exposure to cadmium. Pediatr. Surg. Int. 32, 175–186. https://doi.org/10.1007/s00383-015-3830-9

- Giubilini, A., Bondioli, F., Messori, M., Nyström, G., Siqueira, G., 2021. Advantages of Additive Manufacturing for Biomedical Applications of Polyhydroxyalkanoates. Bioengineering 8, 29. https://doi.org/10.3390/bioengineering8020029

- Giubilini, A., Sciancalepore, C., Messori, M., Bondioli, F., 2020a. New biocomposite obtained using poly(3-hydroxybutyrate-co-3-hydroxyhexanoate) (PHBH) and microfibrillated cellulose. J. Appl. Polym. Sci. 137, 48953. https://doi.org/10.1002/app.48953

- Giubilini, A., Siqueira, G., Clemens, F.J., Sciancalepore, C., Messori, M., Nyström, G., Bondioli, F., 2020b. 3D-Printing Nanocellulose-Poly (3-hydroxybutyrate-co-3-hydroxyhexanoate) Biodegradable Composites by Fused Deposition Modeling. ACS Sustain. Chem. Eng. 8, 10292–10302. https://doi.org/10.1021/acssuschemeng.0c03385

- Gungor-Ozkerim, P.S., Inci, I., Zhang, Y.S., Khademhosseini, A., Dokmeci, M.R., 2018. Bioinks for 3D bioprinting: an overview. Biomater. Sci. 6, 915–946. https://doi.org/10.1039/C7BM00765E

- Hench, L.L., 2006. The story of Bioglass®. J. Mater. Sci. Mater. Med. 17, 967–978. https://doi.org/10.1007/s10856-006-0432-z

- Hoppe, A., Güldal, N.S., Boccaccini, A.R., 2011. A review of the biological response to ionic dissolution products from bioactive glasses and glass-ceramics. Biomaterials 32, 2757–2774. https://doi.org/10.1016/j.biomaterials.2011.01.004

- Hwang, H.S., Lee, C.-S., 2023. Recent Progress in Hyaluronic-Acid-Based Hydrogels for Bone Tissue Engineering. Gels 9, 588. https://doi.org/10.3390/gels9070588

- Jain, R.K., Au, P., Tam, J., Duda, D.G., Fukumura, D., 2005. Engineering vascularized tissue. Nat. Biotechnol. 23, 821–823. https://doi.org/https://doi.org/10.1038/nbt0705-821

- Janse, E.M., Jeurissen, S.H., 1991. Ontogeny and function of two non-lymphoid cell populations in the chicken embryo. Immunobiology 182, 472–481. https://doi.org/https://doi.org/10.1016/S0171-2985(11)80211-1

- Jebrane, M., Sèbe, G., 2007. A novel simple route to wood acetylation by transesterification with vinyl acetate. Holzforschung 61, 143–147. https://doi.org/10.1515/HF.2007.026

- Jones, J.R., 2013. Review of bioactive glass: From Hench to hybrids. Acta Biomater. 9, 4457–4486. https://doi.org/10.1016/j.actbio.2012.08.023

- Karageorgiou, V., Kaplan, D., 2005. Porosity of 3D biomaterial scaffolds and osteogenesis. Biomaterials 26, 5474–5491. https://doi.org/10.1016/j.biomaterials.2005.02.002

- Kargozar, S., Baino, F., Hamzehlou, S., Hill, R.G., Mozafari, M., 2018. Bioactive Glasses: Sprouting Angiogenesis in Tissue Engineering. Trends Biotechnol. 36, 430–444. https://doi.org/10.1016/j.tibtech.2017.12.003

- Koons, G.L., Diba, M., Mikos, A.G., 2020. Materials design for bone-tissue engineering. Nat. Rev. Mater. 5, 584–603.

- Krüger-Genge, Blocki, Franke, Jung, 2019. Vascular Endothelial Cell Biology: An Update. Int. J. Mol. Sci. 20, 4411. https://doi.org/10.3390/ijms20184411

- Kumar, M., Rathour, R., Singh, R., Sun, Y., Pandey, A., Gnansounou, E., Andrew Lin, K.-Y., Tsang, D.C.W., Thakur, I.S., 2020. Bacterial polyhydroxyalkanoates: Opportunities, challenges, and prospects. J. Clean. Prod. 263, 121500. https://doi.org/10.1016/j.jclepro.2020.121500

- Kusumbe, A.P., Ramasamy, S.K., Adams, R.H., 2014. Coupling of angiogenesis and osteogenesis by a specific vessel subtype in bone. Nature 507, 323–328. https://doi.org/10.1038/nature13145

- Langer, R., Vacanti, J.P., 1993. Tissue Engineering. Science 260, 5110. https://doi.org/10.1126/science.8493529

- Lefebvre, L., Chevalier, J., Gremillard, L., Zenati, R., Thollet, G., Bernache-Assolant, D., Govin, A., 2007. Structural transformations of bioactive glass 45S5 with thermal treatments. Acta Mater. 55, 3305–3313. https://doi.org/10.1016/j.actamat.2007.01.029

- Levenberg, S., Rouwkema, J., Macdonald, M., Garfein, E.S., Kohane, D.S., Darland, D.C., Marini, R., van Blitterswijk, C.A., Mulligan, R.C., D'Amore, P.A., Langer, R., 2005. Engineering vascularized skeletal muscle tissue. Nat. Biotechnol. 23, 879–884. https://doi.org/10.1038/nbt1109

- Liu, W.C., Chen, S., Zheng, L., Qin, L., 2017. Angiogenesis Assays for the Evaluation of Angiogenic Properties of Orthopaedic Biomaterials - A General Review. Adv. Healthc. Mater. 6, 1600434. https://doi.org/10.1002/adhm.201600434

- Lu, H., Zhang, S., Guo, L., Li, W., 2017. Applications of graphene-based composite hydrogels: a review. RSC Adv. 7, 51008–51020. https://doi.org/10.1039/C7RA09634H

- Malikmammadov, E., Tanir, T.E., Kiziltay, A., Hasirci, V., Hasirci, N., 2018. PCL and PCL-based materials in biomedical applications. J. Biomater. Sci. Polym. Ed. 29, 863–893. https://doi.org/10.1080/09205063.2017.1394711

- Marinho, A., Nunes, C., Reis, S., 2021. Hyaluronic Acid: A Key Ingredient in the Therapy of Inflammation. Biomolecules 11, 1518. https://doi.org/10.3390/biom11101518

- Mecca, F.G., Bellucci, D., Cannillo, V., 2023. Effect of Thermal Treatments and Ion Substitution on Sintering and Crystallization of Bioactive Glasses: A Review. Materials 16, 4651. https://doi.org/10.3390/ma16134651

- Moreno-Jiménez, I., Hulsart-Billstrom, G., Lanham, S.A., Janeczek, A.A., Kontouli, N., Kanczler, J.M., Evans, N.D., Oreffo, R.O., 2016. The chorioallantoic membrane (CAM) assay for the study of human bone regeneration: a refinement animal model for tissue engineering. Sci. Rep. 6. https://doi.org/10.1038/srep32168

- Nanni, A., Messori, M., 2021. Effect of the wine wastes on the thermal stability, mechanical properties, and biodegradation's rate of poly(3-hydroxybutyrate). J. Appl. Polym. Sci. 138. https://doi.org/10.1002/app.49713

- Narayan, D., Venkatraman, S.S., 2008. Effect of pore size and interpore distance on endothelial cell growth on polymers. J. Biomed. Mater. Res. A 87A, 710–718. https://doi.org/10.1002/jbm.a.31749

- Nicosia, R.F., 2009. The aortic ring model of angiogenesis: a quarter century of search and discovery. J. Cell. Mol. Med. 13, 4113–4136. https://doi.org/10.1111/j.1582-4934.2009.00891.x

- Nowak-Sliwinska, P., Alitalo, K., Allen, E., Anisimov, A., Aplin, A.C., Auerbach, R., Augustin, H.G., Bates, D.O., van Beijnum, J.R., Bender, R.H.F., Bergers, G., Bikfalvi, A., Bischoff, J., Böck, B.C., Brooks, P.C., Bussolino, F., Cakir, B., Carmeliet, P., Castranova, D., Cimpean, A.M., Cleaver, O., Coukos, G., Davis, G.E., De Palma, M., Dimberg, A., Dings, R.P.M., Djonov, V., Dudley, A.C., Dufton, N.P., Fendt, S.-M., Ferrara, N., Fruttiger, M., Fukumura, D., Ghesquière, B., Gong, Y., Griffin, R.J., Harris, A.L., Hughes, C.C.W., Hultgren, N.W., Iruela-Arispe, M.L., Irving, M., Jain, R.K., Kalluri, R., Kalucka, J., Kerbel, R.S., Kitajewski, J., Klaassen, I., Kleinmann, H.K., Koolwijk, P., Kuczynski, E., Kwak, B.R., Marien, K., Melero-Martin, J.M., Munn, L.L., Nicosia, R.F., Noel, A., Nurro, J., Olsson, A.-K., Petrova, T.V., Pietras, K., Pili, R., Pollard, J.W., Post, M.J., Quax, P.H.A., Rabinovich, G.A., Raica, M., Randi, A.M., Ribatti, D., Ruegg, C., Schlingemann, R.O., Schulte-Merker, S., Smith, L.E.H., Song, J.W., Stacker, S.A., Stalin, J., Stratman, A.N., Van de Velde, M., van Hinsbergh, V.W.M., Vermeulen, P.B., Waltenberger, J., Weinstein, B.M., Xin, H., Yetkin-Arik, B., Yla-Herttuala, S., Yoder, M.C., Griffioen, A.W., 2018. Consensus guidelines for the use and interpretation of angiogenesis assays. Angiogenesis 21, 425–532. https://doi.org/10.1007/s10456-018-9613-x

- Oranger, A., Brunetti, G., Colaianni, G., Tamma, R., Carbone, C., Lippo, L., Mori, G., Pignataro, P., Cirulli, N., Zerlotin, R., Moretti, B., Notarnicola, A., Ribatti, D., Grano, M., Colucci, S., 2017. Sclerostin stimulates angiogenesis in human endothelial cells. Bone 101, 26–36. https://doi.org/10.1016/j.bone.2017.03.001

- Ozbolat, I.T., 2016. 3D Bioprinting: fundamentals, principles and applications. Academic Press.

- Palumbo, C., Cavani, F., Sena, P., Benincasa, M., Ferretti, M., 2012. Osteocyte Apoptosis and Absence of Bone Remodeling in Human Auditory Ossicles and Scleral Ossicles of Lower Vertebrates: A Mere Coincidence or Linked Processes? Calcif. Tissue Int. 90, 211–218. https://doi.org/10.1007/s00223-012-9569-6

- Palumbo, C., Sisi, F., Checchi, M., 2023. CAM Model: Intriguing Natural Bioreactor for Sustainable Research and Reliable/Versatile Testing. Biology 12, 1219. https://doi.org/10.3390/biology12091219

- Pati, F., Jang, J., Lee, J.W., Cho, D.-W., 2015. Extrusion Bioprinting. Essent. 3D Biofabrication Transl. 123–152. https://doi.org/10.1016/B978-0-12-800972-7.00007-4

- Peng, X., Qu, W., Jia, Y., Wang, Y., Yu, B., Tian, J., 2020. Bioresorbable Scaffolds: Contemporary Status and Future Directions. Front. Cardiovasc. Med. 7. https://doi.org/10.3389/fcvm.2020.589571

- Potente, M., Gerhardt, H., Carmeliet, P., 2011. Basic and Therapeutic Aspects of Angiogenesis. Cell 146, 873–887. https://doi.org/10.1016/j.cell.2011.08.039

- Puppi, D., Pecorini, G., Chiellini, F., 2019. Biomedical Processing of Polyhydroxyalkanoates. Bioengineering 6, 108. https://doi.org/10.3390/bioengineering6040108

- Puppi, D., Pirosa, A., Lupi, G., Erba, P.A., Giachi, G., Chiellini, F., 2017. Design and fabrication of novel polymeric biodegradable stents for small caliber blood vessels by computer-aided wet-spinning. Biomed. Mater. 12, 35011. https://doi.org/10.1088/1748-605X/aa6a28

- Ribatti, D., Annese, T., Tamma, R., 2020. The use of the chick embryo CAM assay in the study of angiogenic activiy of biomaterials. Microvasc. Res. 131, 104026. https://doi.org/10.1016/j.mvr.2020.104026

- Roseti, L., Parisi, V., Petretta, M., Cavallo, C., Desando, G., Bartolotti, I., Grigolo, B., 2017. Scaffolds for Bone Tissue Engineering: State of the art and new perspectives. Mater. Sci. Eng. C 78, 1246–1262. https://doi.org/10.1016/j.msec.2017.05.017

- Rous, P., Murphy, J.B., 1912. The histological signs of resistance to a transmissible sarcoma of the fowl. J. Exp. Med. 15, 270. https://doi.org/10.1084/jem.15.3.270

- Rouwkema, J., Khademhosseini, A., 2016. Vascularization and Angiogenesis in Tissue Engineering: Beyond Creating Static Networks. Trends Biotechnol. 34, 733–745. https://doi.org/10.1016/j.tibtech.2016.03.002

- Russell, W.M.S., Burch, R.L., 1960. The Principles of Humane Experimental Technique. Med. J. Aust. 1, 500–500. https://doi.org/10.5694/j.1326-5377.1960.tb73127.x

- Schneider-Stock, R., Ribatti, D., 2020. The CAM Assay as an Alternative In Vivo Model for Drug Testing, in: Schäfer-Korting, M., Stuchi Maria-Engler, S., Landsiedel, R. (Eds.), Organotypic Models in Drug Development. Springer International Publishing, Cham, pp. 303–323.

- Shamloo, A., Heilshorn, S.C., 2010. Matrix density mediates polarization and lumen formation of endothelial sprouts in VEGF gradients. Lab. Chip 10, 3061. https://doi.org/10.1039/c005069e

- Siemerink, M.J., Klaassen, I., Vogels, I.M.C., Griffioen, A.W., Van Noorden, C.J.F., Schlingemann, R.O., 2012. CD34 marks angiogenic tip cells in human vascular endothelial cell cultures. Angiogenesis 15, 151–163. https://doi.org/10.1007/s10456-011-9251-z

- Simunovic, F., Finkenzeller, G., 2021. Vascularization Strategies in Bone Tissue Engineering. Cells 10, 1749. https://doi.org/10.3390/cells10071749

- Spanel-Borowski, K., 1989. The chick chorioallantoic membrane as test system for biocompatible materials. Res. Exp. Med. (Berl.) 189, 69–75. https://doi.org/10.1007/BF01856032

- Stanzani, V., Giubilini, A., Checchi, M., Bondioli, F., Messori, M., Palumbo, C., 2023. Eco-Sustainable Approaches in Bone Tissue Engineering: Evaluating the Angiogenic Potential of Different Poly(3-Hydroxybutyrate-Co-3-Hydroxyhexanoate)–Nanocellulose Composites with the Chorioallantoic Membrane Assay. Adv. Eng. Mater. 25, 2200934. https://doi.org/10.1002/adem.202200934

- Stegen, S., van Gastel, N., Carmeliet, G., 2015. Bringing new life to damaged bone: The importance of angiogenesis in bone repair and regeneration. Bone 70, 19–27. https://doi.org/10.1016/j.bone.2014.09.017

- Sun, M., Sun, X., Wang, Z., Guo, S., Yu, G., Yang, H., 2018. Synthesis and Properties of Gelatin Methacryloyl (GelMA) Hydrogels and Their Recent Applications in Load-Bearing Tissue. Polymers 10, 1290. https://doi.org/10.3390/polym10111290

- Tingaut, P., Zimmermann, T., Lopez-Suevos, F., 2010. Synthesis and Characterization of Bionanocomposites with Tunable Properties from Poly(lactic acid) and Acetylated Microfibrillated Cellulose. Biomacromolecules 11, 454–464. https://doi.org/10.1021/bm901186u

- Unger, R.E., Sartoris, A., Peters, K., Motta, A., Migliaresi, C., Kunkel, M., Bulnheim, U., Rychly, J., James Kirkpatrick, C., 2007. Tissue-like self-assembly in cocultures of endothelial cells and osteoblasts and the formation of microcapillary-like structures on three-dimensional porous biomaterials. Biomaterials 28, 3965–3976. https://doi.org/10.1016/j.biomaterials.2007.05.032

- Valdes, T.I., Kreutzer, D., Moussy, F., 2002. The chick chorioallantoic membrane as a novel in vivo model for the testing of biomaterials. J. Biomed. Mater. Res. Off. J. Soc. Biomater. Jpn. Soc. Biomater. Aust. Soc. Biomater. Korean Soc. Biomater. 62, 273–282. https://doi.org/10.1002/jbm.10152

- Valentini, F., Dorigato, A., Rigotti, D., Pegoretti, A., 2019. Polyhydroxyalkanoates/Fibrillated Nanocellulose Composites for Additive Manufacturing. J. Polym. Environ. 27, 1333–1341. https://doi.org/10.1007/s10924-019-01429-8

- Vert, M., Doi, Y., Hellwich, K.-H., Hess, M., Hodge, P., Kubisa, P., Rinaudo, M., Schué, F., 2012. Terminology for biorelated polymers and applications (IUPAC Recommendations 2012). Pure Appl. Chem. 84, 377–410. https://doi.org/10.1351/PAC-REC-10-12-04

- Vitale-Brovarone, C., Baino, F., Verné, E., 2009. High strength bioactive glass-ceramic scaffolds for bone regeneration. J. Mater. Sci. Mater. Med. 20, 643–653. https://doi.org/10.1007/s10856-008-3605-0

- Von Euw, S., Wang, Y., Laurent, G., Drouet, C., Babonneau, F., Nassif, N., Azaïs, T., 2019. Bone mineral: new insights into its chemical composition. Sci. Rep. 9. https://doi.org/10.1038/s41598-019-44620-6

- Wang, Y.-W., Wu, Q., Chen, G.-Q., 2004. Attachment, proliferation and differentiation of osteoblasts on random biopolyester poly(3-hydroxybutyrate-co-3-hydroxyhexanoate) scaffolds. Biomaterials 25, 669–675. https://doi.org/10.1016/S0142-9612(03)00561-1

- Xie, H., Cui, Z., Wang, L., Xia, Z., Hu, Y., Xian, L., Li, C., Xie, L., Crane, J., Wan, M., Zhen, G., Bian, Q., Yu, B., Chang, W., Qiu, T., Pickarski, M., Duong, L.T., Windle, J.J., Luo, X., Liao, E., Cao, X., 2014. PDGF-BB secreted by preosteoclasts induces angiogenesis during coupling with osteogenesis. Nat. Med. 20, 1270–1278. https://doi.org/10.1038/nm.3668

- Yang, M., Zhu, S., Chen, Y., Chang, Z., Chen, G., Gong, Y., Zhao, N., Zhang, X., 2004. Studies on bone marrow stromal cells affinity of poly (3-hydroxybutyrate-co-3-hydroxyhexanoate). Biomaterials 25, 1365–1373. https://doi.org/10.1016/j.biomaterials.2003.08.018

- Yilmaz, B., Tahmasebifar, A., Baran, E.T., 2019. Bioprinting Technologies in Tissue Engineering.

- Zhang, J., Eyisoylu, H., Qin, X.-H., Rubert, M., Müller, R., 2021. 3D bioprinting of graphene oxide-incorporated cell-laden bone mimicking scaffolds for promoting scaffold fidelity, osteogenic differentiation and mineralization. Acta Biomater. 121, 637–652. https://doi.org/10.1016/j.actbio.2020.12.026

- Zhang, L., Zheng, Z., Xi, J., Gao, Y., Ao, Q., Gong, Y., Zhao, N., Zhang, X., 2007. Improved mechanical property and biocompatibility of poly(3-hydroxybutyrate-co-3-hydroxyhexanoate) for blood vessel tissue engineering by blending with poly(propylene carbonate). Eur. Polym. J. 43, 2975–2986. https://doi.org/10.1016/j.eurpolymj.2007.04.007

- Zhu, H., Zheng, K., Boccaccini, A.R., 2021. Multi-functional silica-based mesoporous materials for simultaneous delivery of biologically active ions and therapeutic biomolecules. Acta Biomater. 129, 1–17. https://doi.org/10.1016/j.actbio.2021.05.007

- Zwadlo-Klarwasser, G., Görlitz, K., Hafemann, B., Klee, D., Klosterhalfen, B., 2001. The chorioallantoic membrane of the chick embryo as a simple model for the study of the angiogenic and inflammatory response to biomaterials. J. Mater. Sci. Mater. Med. 12, 195–199. https://doi.org/10.1023/a:1008950713001